CHARGE TRANSFER IN CONJUGATED ORGANOMETALLIC MATERIALS

by

YONGBAO ZHU

B.Sc., Zhejiang University, 1987
M.Sc., Chinese Academy of Sciences at Fuzhou, 1990

A THESIS SUBMITTED IN PARTIAL FULFILLMENT OF
THE REQUIREMENTS FOR THE DEGREE OF

DOCTOR OF PHILOSOPHY

in

THE FACULTY OF GRADUATE STUDIES

(Department of Chemistry)

THE UNIVERSITY OF BRITISH COLUMBIA

May 2000

Abstract

This thesis examines factors which influence charge delocalization in conjugated organometallic materials. This delocalization is examined by electrochemical and spectroscopic characterization of model complexes, oligomers and polymers.

The complex [*cis*-Ru(dppm)$_2$(C≡CFc)$_2$]CuI (dppm = $Ph_2PCH_2PPh_2$, Fc = ferrocenyl) (**52**) is prepared by the coupling of FcC≡CSn(*n*-Bu)$_3$ (**60**) and $RuCl_2$(dppm)$_2$ in the presence of excess CuI, while *trans*-Ru(dmpe)$_2$(C≡CFc)$_2$ (dmpe = $Me_2PCH_2CH_2PMe_2$) (**54**) is obtained from $RuCl_2$(dmpe)$_2$ and **60** using catalytic CuI. Removal of the coordinated CuI from **52** with excess P(OMe)$_3$ yields *trans*-Ru(dppm)$_2$(C≡CFc)$_2$ (**53**). The mono- and dications of both **52** – **54** and *trans,trans,trans*-Ru(PBu$_3$)$_2$(CO)(L)(C≡CFc)$_2$ complexes (L = CO (**55**); py (**56**); P(OMe)$_3$ (**57**)) are prepared by oxidation with $FcPF_6$. All the neutral and oxidized species are characterized using UV–Vis–near-IR spectroscopy and cyclic voltammetry (CV). The data are interpreted according to the Hush model of electron transfer, and the results indicate that ruthenium bisacetylide bridges facilitate electronic interactions between the two terminal ferrocenyl groups. Charge delocalization between the Fe^{III} and Ru^{II} centers in the oxidized species is enhanced when the ancillary ligands on the Ru center are electron donors and is lessened when the ligands are acceptors.

Complexes *trans*-Ru(dppm)$_2$(Cl)(C≡CR) (**62a – c**), *trans*-Ru(dppm)$_2$(C≡CR)$_2$ (**63a – c**), and Fc–≡–R (**68a – e**), Fc–≡–R–≡–Fc (**69a – e**) and R–Fc–R (**40, 50** and **73**) (R = 1 – 3 linked thiophene rings with various substituents) are prepared to elucidate electronic interactions between the metals and oligothienyl groups. The complexes are all redox-active due to the $Ru^{II/III}$ and $Fe^{II/III}$ couples and oligothiophene-based oxidations. The CVs of **62a – c**

and **63a – c** show that the $Ru^{II/III}$ oxidation process becomes more reversible with an increase in the conjugation length of the oligothienyl group. Complexes **68a – e, 69a – e, 40, 50** and **73** all contain a reversible $Fe^{II/III}$ oxidation wave and an irreversible oligothiophene-based wave. When oxidized past the oligothiophene-based oxidation potential, and by careful exclusion of water, the complexes with terminal bi- and terthienyl groups (**50, 62b, 62c, 68c, 68e** and **73**) electropolymerize or dimerize, resulting in the deposition of an electrochemically active film on the electrode surface.

The monocations $\mathbf{62c}^+$ and $\mathbf{63c}^+$ prepared in solution at –20 °C exhibit intense LMCT absorption bands at 500 – 700 nm and 900 — 1700 nm, indicative of significant charge delocalization from the Ru^{III} to the conjugated oligothienyl group. Electrochemical oxidation of the Fe^{II} centers in the ferrocene-oligothiophene complexes yields the corresponding monocations and dications, which all have oligothiophene-to-Fe^{III} charge-transfer transitions in the near-IR region. For each series, the energy and intensity of these low-energy transitions correlate to the difference in the oxidation potentials of the ferrocenyl and oligothienyl groups, showing that charge delocalization in these compounds is enhanced when the conjugated organic group and the metal are close in oxidation potential.

The complex *trans*-$RuCl_2(dppm)_2$ (**19**) is converted to its cis isomer (**59**) at 20 °C in the presence of catalytic CuCl or CuI, and $[\{cis\text{-}RuCl_2(dppm)_2\}_2Cu][CuCl_2]$ (**74**) is isolated when **19** or **59** reacts with excess CuCl. Addition of a small amount of **74** to a solution of **19** results in isomerization of **19** to **59**. Complex **74** can be converted quantitatively to **59** by reaction with excess $[(n\text{-}Bu)_4N]Cl$ or HCl (aq). A mechanism for the catalytic isomerization of **19** to **59** and the formation of **74** is proposed on the base of *in situ* ^{31}P NMR results.

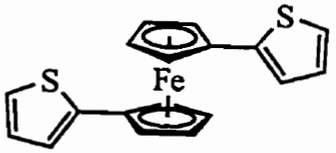

40

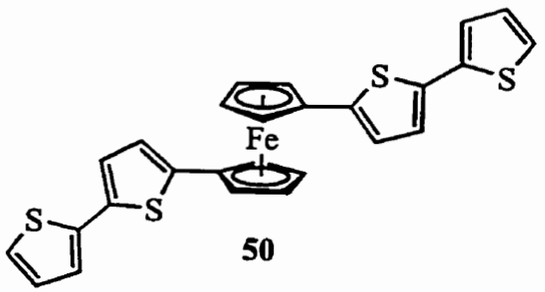

50

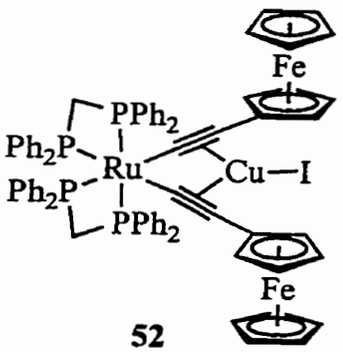

52

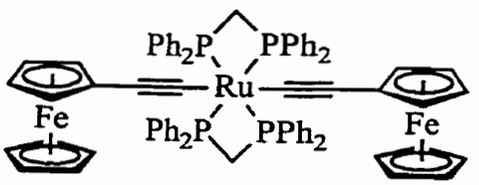

53

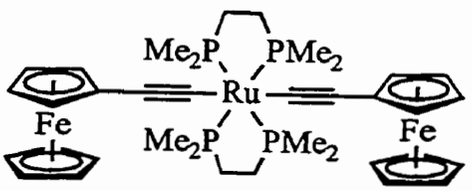

54

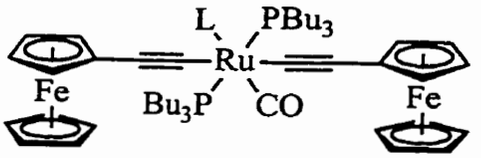

55 L = CO
56 L = py
57 L = $P(OMe)_3$

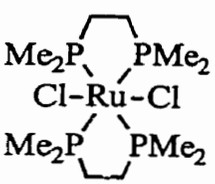

58

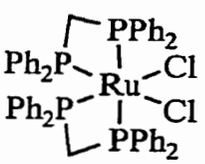

59

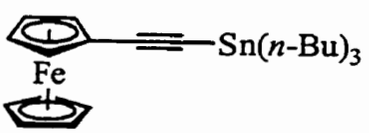

60

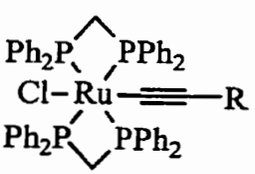

62a – c

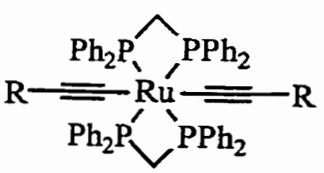

63a – c

R = 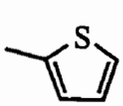

a

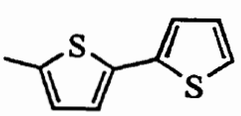

b

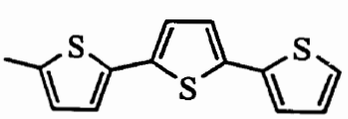

c

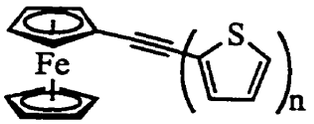

68a (n =1)
68b (n =2)
68c (n =3)

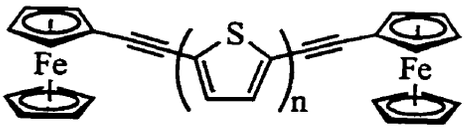

69a (n =1)
69b (n =2)
69c (n =3)

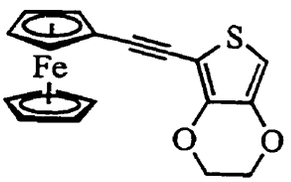

68d

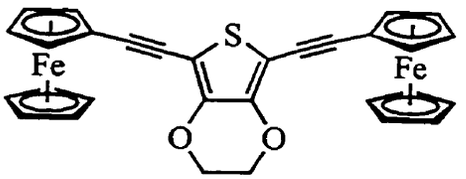

69d

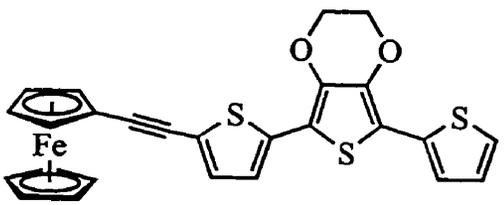

68e

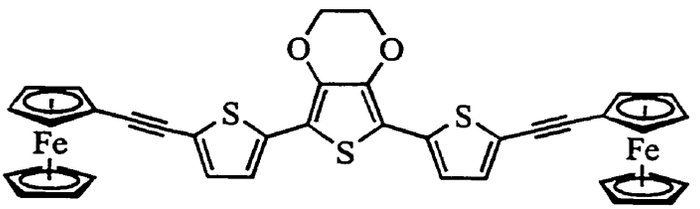

69e

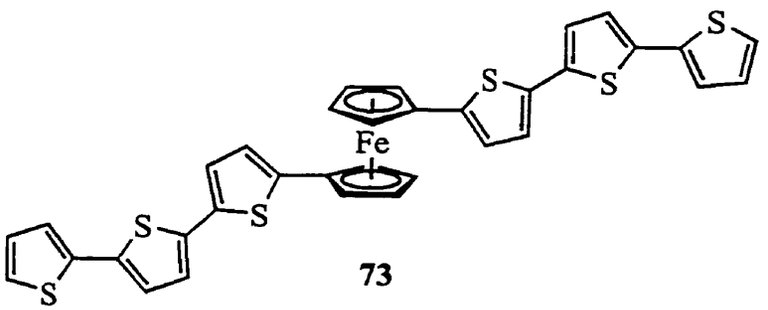

73

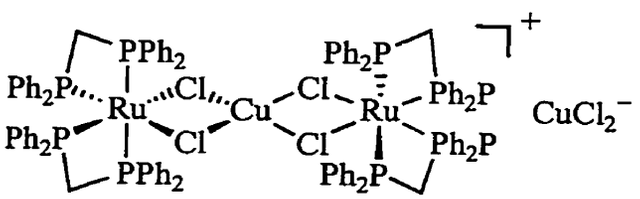

74

Table of Contents

List of Tables

List of Figures

List of Schemes

List of Equations

List of Symbols and Abbreviations

Symbol	Description	Units
c	speed of light	cm/s
d	intermetallic distance	m
	transition dipole length	m
D	correction factor in eqs 12 – 14	cm^{-1}
D_s	static dielectric constant of solvent	
ΔE	oxidation potential difference between two redox couples	V
ΔE^o	ground-state energy difference (Figures 7b, 12)	cm^{-1}
$\Delta E'$	additional energy due to spin-orbit or ligand-field splitting	cm^{-1}
$\Delta\nu_{1/2}$	bandwidth at the half-peak height in spectrum	cm^{-1}
e	electric charge	C
$E_{1/2}$	half-wave potential	V
E_g	band gap	eV
$E_{p,a}$	anodic peak potential	V
$E_{p,c}$	cathodic peak potential	V
E_{th}	thermal activation energy (Figures 7a, 17)	cm^{-1}
F	Faraday constant	C/mol
f	oscillator strength	cm^{-1}
G	degeneracy of states	
h	Plank constant	J s
H_{ad}	resonance exchange integral (Figure 7a)	cm^{-1}
$i_{p,a}$	anodic peak current	μA
$i_{p,c}$	cathodic peak current	μA
K_c	comproportionation constant	
J	coupling constant	Hz
M	transition dipole moment	C m
m	number of electron transferred in an IVCT process	
n	number of electron involved in a redox process	

	refractive index of solvent	
R	gas constant	J/(mol K)
	correction coefficient	
r	radius of a metal coordination sphere	m
T	temperature	K
α^2	delocalization coefficient or interaction parameter	
ε	extinction coefficient	$M^{-1}cm^{-1}$
λ_{max}	wavelength at band maximum	nm
ν_{max}	absorption energy at band maximum	cm^{-1}
ν_{op}	optical-transition energy (Figures 7, 12)	cm^{-1}
ν	frequency (wavenumber)	cm^{-1}
δ	chemical shift	ppm
χ_i	inner rearrangement parameter	cm^{-1}
χ_o	outer reorganization parameter	cm^{-1}

Abbreviation	**Description**
Å	angstrom
OAc	acetate
Anal.	analysis
aq	aqueous
bpy	bipyridine
Bu	butyl
C	coulomb
Calcd	calculated
°C	degrees Celsius
CB	conduction band
cm	centimeter
Cp	cyclopentadienyl
CV	cyclic voltammetry
Cy	cyclohexyl
Δ	heat at reflux

dd	doublet of doublets
deg	degree
dmpe	$Me_2PCH_2CH_2PMe_2$ or 1,2-bis(dimethylphosphino)ethane
dppm	$Ph_2PCH_2PPh_2$ or bis(diphenylphosphino)methane
dppp	$Ph_2PCH_2CH_2CH_2PPh_2$ or 1,3-bis(diphenylphosphino)propane
e	electron
eq	equation
Et	ethyl
eV	electronvolt
Fc	ferrocene; ferrocenyl
h	hour
HOCO	highest occupied crystal orbital
HOMO	highest occupied molecular orbital
IR	infrared
ITO	indium tin oxide
IVCT	intervalence charge transfer
K	Kelvin
L	liter
LMCT	ligand-to-metal charge transfer
LUCO	lowest unoccupied crystal orbital
LUMO	lowest unoccupied molecular orbital
M	metal; mol/L (molar)
m	multiplet
	meter
max	maximum
Me	methyl
mg	milligram
MHz	megahertz
min	minimum
mL	milliliter
MLCT	metal-to-ligand charge transfer

mmol	millimole
mol	mole
mV	millivolt
near-IR	near-infrared
NMR	nuclear magnetic resonance
nm	nanometer
μA	microampere
μm	micrometer
o	ortho
OTf	$^{-}OSO_2CF_3$ or triflate
p	para
ppm	parts per million
Ph	phenyl
py	pyridyl
ref	reference
S	siemens (conductance)
s	singlet; second
SCE	saturated calomel electrode
sh	shoulder
SSCE	saturated sodium chloride calomel electrode
t	triplet
TCNE	tetracyanoethylene
TCNQ	(2,2′-(2,5-cyclohexadiene-1,4-diylidene)bispropanedinitrile
THF	tetrahydrofuran
UV	ultraviolet
V	volt
VB	valence band
vis	visible
vs	versus
v/v	volume-to-volume ratio

Acknowledgements

First and foremost, I would like to thank my supervisor, Dr. Michael Wolf, for helping me to be a good chemist. Without his continuous support, guidance, patience and encouragement I would never be in a position to present this thesis. He taught me chemistry and cared about my career development. I would also like to thank Dr. Peter Legzdins who took his time to read the thesis and make corrections.

I must thank all present and past members in the Wolf group for their great friendship which made my life more cheerful. I specially appreciate Olivier Clot, Dylan Millet and Nathan Jones for their work which is related to my thesis.

I would like to thank the departmental support staff, especially Liane Diarge, Marietta Austria (NMR), Peter Borda (elemental analysis), and the late Dr. Steve Rettig (X-ray). I appreciate the Thompson and Orvig groups for allowing me to extensively use their spectrometers. I would also like to thank Dr. Glenn Yap in the Department of Chemistry at the University of Windsor for the determination of two solid-state molecular structures.

Finally I thank my wife Xuequn for her unlimited support and my little girl, DuoDuo, who used to wonder why Dad liked spending more time on work than with her.

Chapter 1 General Introduction

The miniaturization of microelectronic devices has been one of the most important scientific ventures in the latter part of the twentieth century. Enormous success has been achieved in the fabrication of integrated circuits for high-speed computers, encouraging continuing efforts towards further miniaturization. An important aspect of these efforts has been focused on the construction of devices on the nanometer scale. Forty years ago, when the construction of such devices was proposed in a speech entitled "Plenty of Room at the Bottom" by physicist Richard Feynman,[1] it seemed to be far from reality. This reality is gradually coming nearer as research both on materials and tools for such devices is progressing. The availability of STM (scanning tunneling microscopy) and AFM (atomic force microscopy) has allowed for the observation and manipulation of single atoms or molecules. Achievements in molecular self-assembly, metal nanoparticles and molecular wires means that the materials needed for such devices are no longer out of reach.[2]

Fabrication of devices from one molecule or a small assembly of molecules is a possible route to nanoscale devices.[3,4] This concept has been considered within an interdisciplinary field called molecular electronics.[2] Molecular electronics was originally defined as the application of a single molecule to process signals, and now is generally recognized as the use of molecule-based materials for electronic applications.[5] Many molecule-based devices, such as transistors, sensors and switches have been designed, and prototypes have been built.[2,3,6] The use of molecular materials provides a huge opportunity for device miniaturization because the functionality of the device arises from the intrinsic properties of individual molecules. It has even been reported that a single, specifically-

designed molecule is able to perform some simple mechanical functions,[7,8] but such molecules are complex to design and synthesize. The preparation of a device using an assembly of such molecules is more practical.

Carrying electricity through a single polymer chain or a small assembly is important for the fabrication of nanometer scale electronic devices. Organic conducting polymers are very useful for such applications due to their high electrical conductivity upon oxidation or reduction. Research into conducting polymers, triggered by the discovery of high conductivity in oxidized polyacetylene in 1977,[9] involves many fields including chemistry, physics, and materials science. A comprehensive summary of research results in this area can be found in two editions of the Handbook of Conducting Polymers, published in 1986[10] and 1998,[11] respectively. Chemists have discovered many new conducting polymers and tailored existing ones for specific purposes, such as the enhancement of conductivity, stability, solubility or processibility. The following introduction covers the fundamentals of organic conducting polymers, as well as recent advances in research on conjugated polymers in which transition-metals are integrated into the polymer backbone. Background on mixed-valence complexes and intervalence charge-transfer is also included, due to its relevance to the work reported in this thesis.

1.1 Organic Conjugated Polymers

Organic conjugated polymers possess a one-dimensional backbone which consists of alternating single and double bonds (or triple bonds). This structural characteristic allows overlap between orbitals with p (or π) symmetry on adjacent atoms, and results in their unique

electronic properties. The structures of several of the more well-studied organic conjugated polymers are shown in Figure 1.

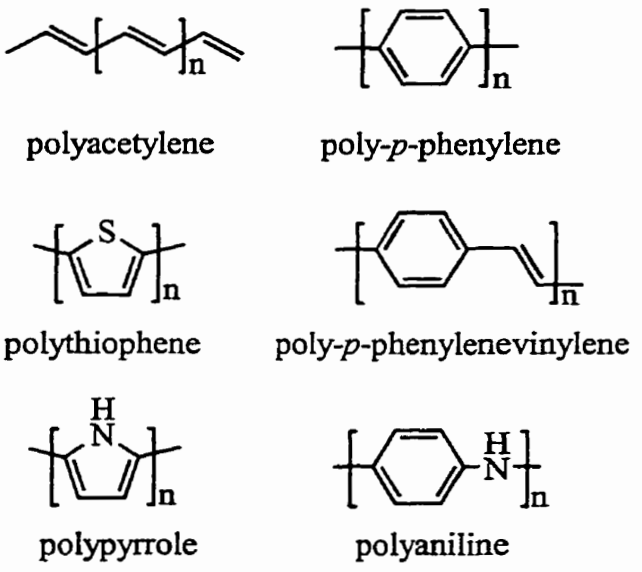

Figure 1. Examples of some common organic conjugated polymers.

Polyacetylene, which took central stage in the early phase of the evolution of this field, shows an increase in electrical conductivity of 12 orders of magnitude when it is oxidized (also called doping).[10] Neutral polyacetylene is semiconducting or insulating with electrical conductivity between ~10^{-5} – 10^{-13} S/cm depending on the ratio of cis to trans double bonds and the number of defects in the backbone. Doping polyacetylene causes a dramatic increase in conductivity up to ~1 – 10^{5} S/cm.[10] The highest conductivity ever measured in the defect-free polyacetylene doped with iodine, is 10^{5} S/cm,[12,13] comparable to that of copper (10^{6} S/cm). The conductivity of polyacetylene varies with doping agents used. Other organic conjugated polymers show similar electrical behavior to polyacetylene. For example, polythiophene is semiconductive (10^{-8} S/cm) in the neutral state, while its conductivity is as great as 10^{3} S/cm upon doping.[10]

Hückel theory predicts that extended conjugation along the polymer backbone causes a decrease in the energy gap between the lowest unoccupied molecular orbital (LUMO) and the highest occupied molecular orbital (HOMO). The absorption maxima in electronic spectra may be used as an estimate of the HOMO – LUMO gap. Polythiophene has λ_{max} at ~ 450 nm, while thiophene has λ_{max} at 243 nm, 2,2′-bithiophene at 302 nm and 2,2′:5′,2″-terthiophene at 355 nm.[14] Neutral polythiophene has a band gap of ~2.2 eV, and a conductivity of 10^{-8} S/cm.[15]

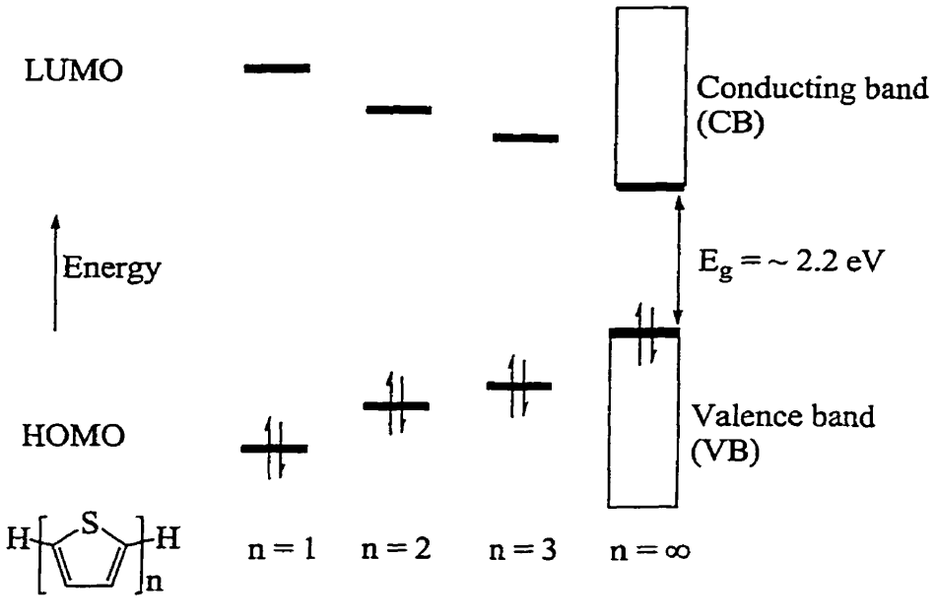

Figure 2. Evolution of the LUMO and HOMO gap energy of oligo- and polythiophenes.

Theories have been developed to understand the behavior of doped organic conjugated polymers.[10,11] One explanation involves the formation of solitons, polarons or bipolarons, as shown in Figure 3, in doped polymers.[10,11] Neutral polyacetylene has two degenerate ground states, thus oxidation of polyacetylene results in the formation of solitons which are associated with an electronic state in the mid-gap. Other conjugated polymers, such as polythiophene,

have a non-degenerate ground state. Lifting the ground-state degeneracy leads to the formation of polarons which are singly-charged paramagnetic states, and bipolarons, spinless bound states of double charges.[10]

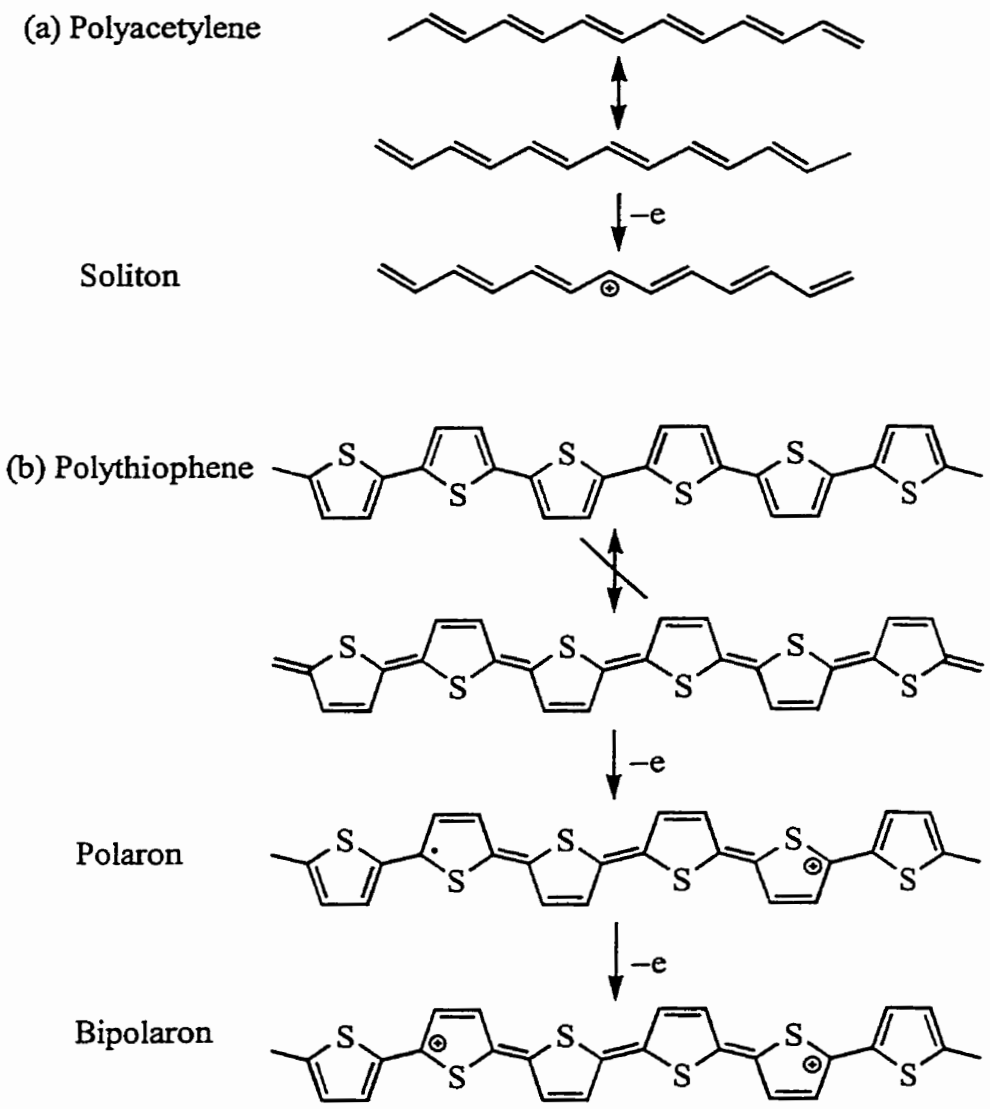

Figure 3. Solitons, polarons and bipolarons in polyacetylene and polythiophene.

Both polarons and bipolarons in polythiophene are associated with two new electronic states between the HOMO and the LUMO (Figure 4). Upon oxidation of polythiophene both

polarons and bipolarons form, and they are associated with two new states, one 0.60 – 0.65 eV above the HOMO, and the other 0.65 – 0.70 eV below the LUMO. As the level of doping is increased these intergap states overlap to form subbands. The subbands have been observed by electronic spectroscopy. Oxidation of polythiophene results in the appearance of a new, very broad band extending from 650 to 2000 nm, indicative of the formation of subbands in doped polythiophene.[10]

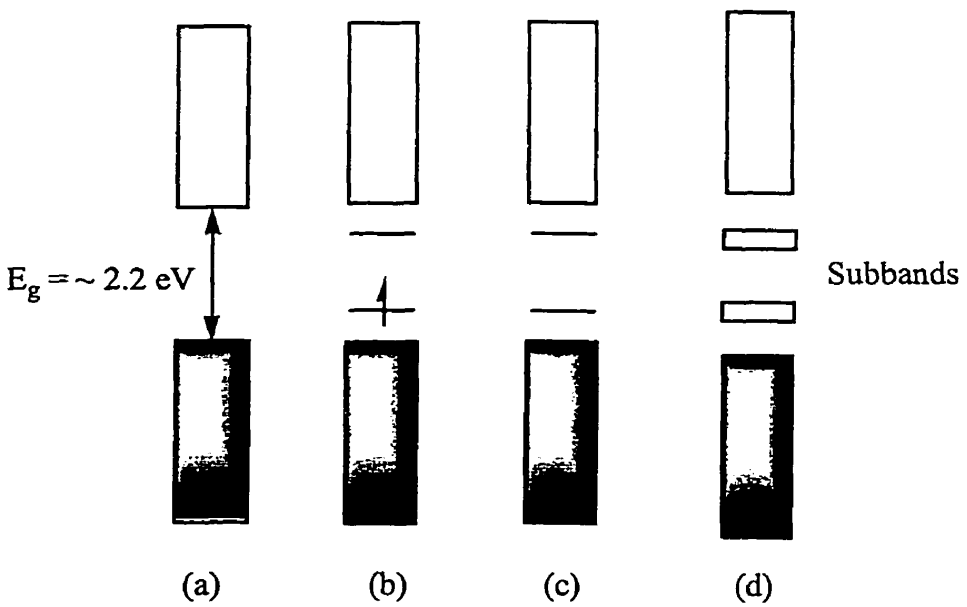

Figure 4. Evolution of the band structure of polythiophene upon oxidation: (a) the neutral form, (b) a polaron, (c) a bipolaron and (d) subbands.

Organic conjugated polymers have been proposed for many applications due to their unique optical and electrical properties. Applications have been discovered in many fields, such as in batteries, microelectronics, display devices, optical devices and coatings;[10,11] however, most commercial applications require the polymers to be chemically and thermally stable both in the neutral and doped states, as well as to be easily processed. Although doped

polyacetylene is highly conductive, its applications are limited by its instability in air and water, and poor processibility. Recently, more attention has been paid to polythiophene and its derivatives, since they are more stable in different oxidation levels, and can be easily modified chemically. Oligothiophenes often have similar properties to polythiophene, and are readily available.

1.2 Poly- and Oligothiophenes and Their Derivatives

Polythiophene has been prepared both by chemical and electrochemical methods.[10,11] Both methods give primarily $\alpha - \alpha$ coupling with some $\alpha - \beta$ coupling, depending on the routes used (Figure 5). Many polythiophene derivatives have been obtained using readily available β-substituted thiophenes, and their solubility and conductivity are significantly affected by the substituents.[10,11]

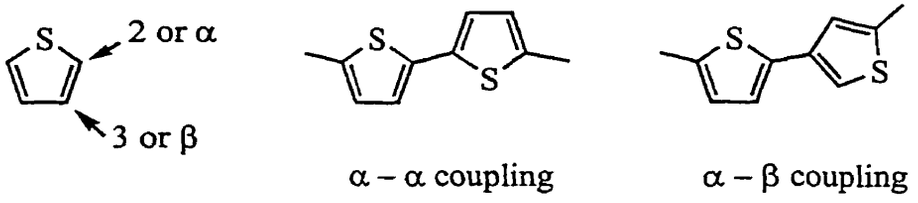

Figure 5. $\alpha - \alpha$ and $\alpha - \beta$ couplings in polythiophene.

There are two common chemical methods for the preparation of polythiophene and its derivatives (Scheme 1): (a) oxidative coupling of thiophene or its dianion using oxidizing reagents such as $FeCl_3$,[16] AsF_5[17] and $CuCl_2$.[18] This approach yields doped polythiophene directly, and (b) transition-metal catalyzed Grignard coupling of 2,5-dihalothiophene.[11] The latter method avoids $\alpha - \beta$ coupling, which occurs frequently with oxidative coupling.

Scheme 1

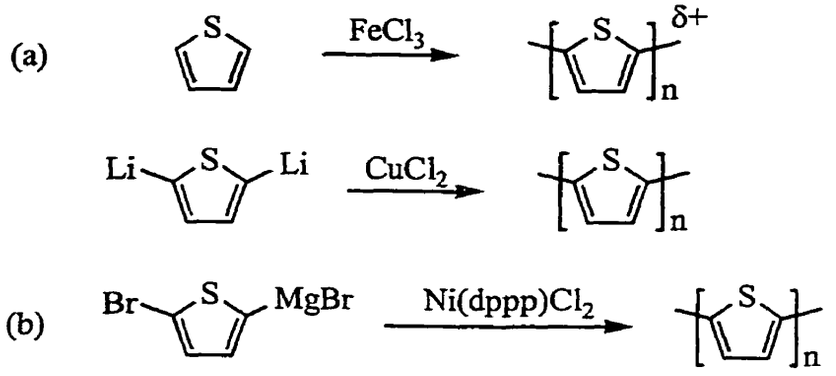

Electropolymerization has also been extensively used to prepare polythiophene and its derivatives. In this method catalysts are not required, avoiding the impurities arising from transition-metal catalysts. Electropolymerization can produce high quality films deposited directly on electrode surfaces. Film thickness can be easily controlled through control of current, voltage and deposition time, and the deposited films can be characterized directly by cyclic voltammetry. The major drawback is that $\alpha - \beta$ coupling may occur due to over-oxidation of thiophene or the resulting intermediates during the polymerization process.

Electropolymerization is typically carried out in a single-compartment cell with a three-electrode configuration. Platinum, gold and indium tin oxide (ITO) surfaces are typically used as working electrodes. Acetonitrile and dichloromethane are commonly used as solvents and tetraalkylammonium salts as supporting electrolytes. Insoluble polythiophene deposits as a film on the working electrode when a sufficiently high potential is applied to the working electrode, or the potential is repeatedly scanned beyond the thiophene-oxidation potential. The latter deposition method involves cyclic voltammetry (CV). CV is a versatile electroanalytical technique, consisting of cycling the potential at the working electrode in an analyte solution, and simultaneously measuring the resulting current. The current-potential plot yields thermodynamic and kinetic information about the redox processes of the analyte,

including redox potentials and reversibility. When CV is used for electropolymerization, the polythiophene film can be obtained either in the neutral or oxidized form.

The mechanism which has been proposed for electropolymerization of thiophene is detailed in Figure 6. Oxidation of the thiophene monomer produces a radical cation, which dimerizes and deprotonates to yield a neutral dimer. Oxidation of the dimer to its radical cation, followed by coupling of the dimer radical cation with another radical cation, allows for propagation of the polymer chain. Since electropolymerization proceeds via radical cation intermediates, it cannot occur in electrochemical media containing nucleophilic species.

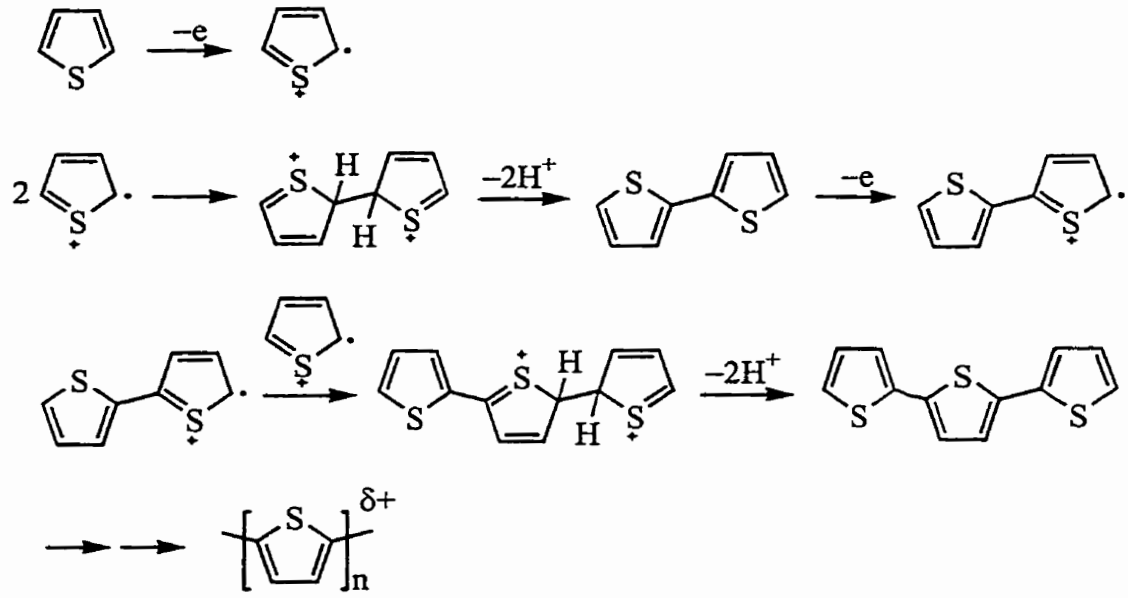

Figure 6. Proposed mechanism of thiophene electropolymerization.[10]

Oligothiophenes can also be electropolymerized to yield polythiophene, but this occurs at a lower oxidation potential than for thiophene. Interestingly, polythiophene prepared from an oligomer has a lower oxidation potential than polymer prepared from thiophene, possibly due to a lower number of $\alpha - \beta$ linkages. Table 1 gives the oxidation potentials of

thiophene, some thiophene derivatives, oligothiophenes and the corresponding polymers. Electron-donating substituents result in a decrease in the oxidation potentials of both monomers and the resulting polymers.

Table 1. Oxidation Potentials of Thiophene Derivatives and Corresponding Polymers [a]

Monomer	$E_{p,a}$ (monomer) (V vs SCE)	$E_{p,a}$ (polymer) (V vs SCE)
Thiophene	1.65	1.1
2,2′-Bithiophene	1.20	0.70
3-Methylthiophene	1.35	0.77
3,4-Dimethylthiophene	1.25	0.98
3-Bromothiophene	1.85	1.35
3,4-Dibromothiophene	2.0	1.45

[a] Refs.[19,20]

In addition to their use as monomers for polythiophene, oligothiophenes are of interest since they are suitable model compounds to elucidate structure-property relationships for organic conjugated polymers, and they are electronic materials in their own right. Oligothiophenes up to 10 thiophene units long have been prepared using either chemical or electrochemical synthetic methods (Scheme 2).[14,21-26] Longer oligomers can be prepared by transition-metal catalyzed Grignard coupling,[14] or by electrochemical dimerization.[25] Tetrathiophene, sexithiophene, and octathiophene have all been chemically synthesized by lithiation of a shorter oligomer followed by dimerization with copper chloride.[24,26] These

oligomers have been used in device applications such as thin film transistors, light-emitting diodes, photovoltaic cells and light modulators.[27-29]

Scheme 2

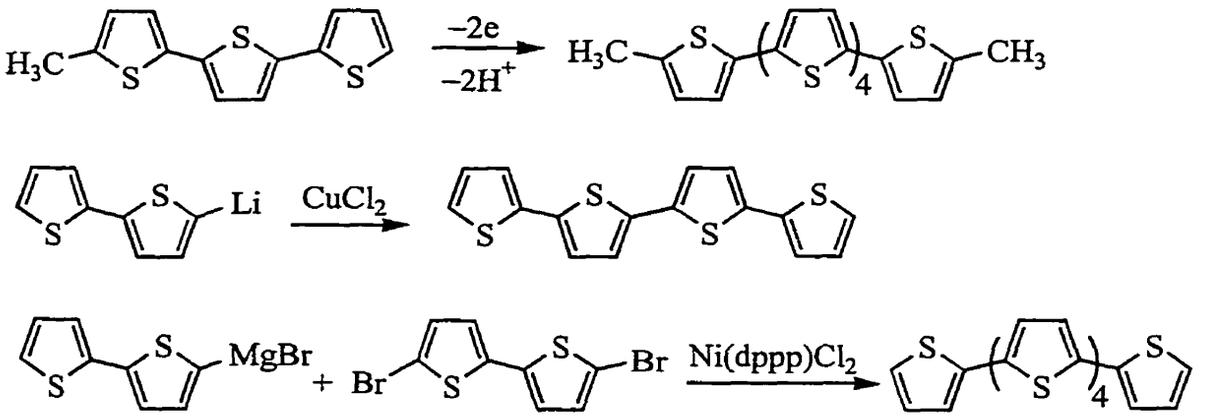

In solution, the absorption maximum (λ_{max}) of the $\pi - \pi^*$ transition in oligothiophenes increases linearly as chain length increases from 1 to 5 units. For longer oligothiophenes, λ_{max} varies only very slightly with length, and is close to that of polythiophene.[14,21] Similarly, a linear relationship between oxidation potential and chain length has been observed in this series.[21] Since long oligothiophenes can be oxidized at lower potentials, and the resulting charge can be delocalized over a more extended conjugation system, longer oxidized oligothiophenes are more stable. The oxidized species of quinquethiophene and sexithiophene can be spectroscopically characterized in highly dilute solution before any coupling reaction occurs.[23,30] CV has been used to characterize both poly- and oligothiophenes.[10] The CV of polythiophene displays a broad redox wave due to the range of conjugation lengths present in the material, while oligothiophenes typically exhibit discrete oxidation processes. For instance, the CV of didodecylsexithiophene demonstrates two reversible redox waves with

$E_{1/2}$ = 0.34 V and 0.54 V referenced to Fc^+/Fc, assigned to an one-electron transfer in each step leading to the radical cation and the dication.[23]

1.3 Charge Transfer and Hush Theory

Originally developed for interpretation of charge-transfer spectra of mixed-valence complexes, Hush theory has also been demonstrated to be useful for the evaluation of other charge-transfer processes.[31] These include charge transfer between organic donors and acceptors,[32,33] as well as ligand-to-metal (LMCT) and metal-to-ligand charge-transfer (MLCT) processes.[34-36] In Hush theory, charge transfer is considered as a process in which an electron is coupled between a donor and an acceptor via a single oscillator which has the same frequency in both initial and final states.[31,37,38] The electronic and optical behavior of polymers consisting of metal centers linked via conjugated organic groups depends on the extent of charge delocalization between the metal centers, as well as between the metal and organic groups. It may therefore be beneficial to use Hush theory to understand charge delocalization in such polymers.

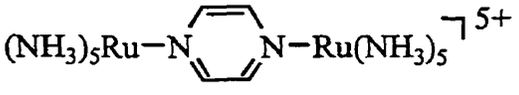

1a

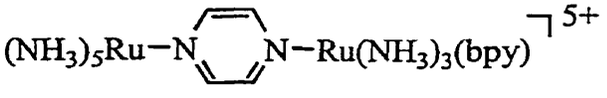

1b

Mixed-valence complexes like the Creutz-Taube ion (**1a**)[39] have been the subject of numerous theoretical and experimental investigations.[37,38,40] This class of complexes contains metal centers in different oxidation states. Mixed-valence complexes have been classified as symmetric, in which the metal centers are identical (e.g. **1a**), and asymmetric, in which the metal centers are different (e.g. **1b**).[41] Charge transfer is often observed between metal centers in mixed-valence complexes. On the basis of the degree of charge

delocalization Robin and Day divided mixed-valence complexes into three classes:[42] Class I, completely valence-trapped (no charge delocalization between metal centers); Class II, partically delocalized (weak coupling); and Class III, completely delocalized (strong coupling).

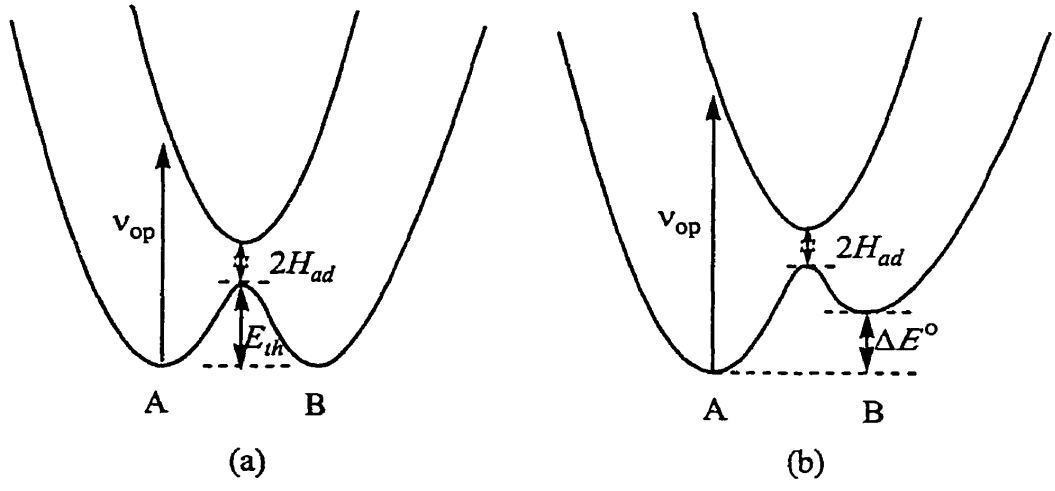

Figure 7. Potential-energy diagrams of initial and final states for (a) a symmetric mixed-valence complex and (b) an asymmetric mixed-valence complex.

In Hush model, potential-energy diagrams are used to explain thermal and optical charge-transfer processes in binuclear mixed-valence complexes (Class II) as shown in Figure 7.[31,37,38] The curve on the left represents the initial state (A) and the curve on the right the final state (B) of the charge-transfer process. A symmetric complex has the same energy for both the initial and final ground states ($\Delta E^{o} = 0$), while an asymmetric complex has $\Delta E^{o} > 0$. The vertical transition between the two states with transition energy ν_{op} represents an optical intervalence charge-transfer (IVCT) process. Broad IVCT bands typically appear in the visible or the near-IR region (400 – 3000 nm). Thermal electron transfer can occur by

vibronic coupling of the initial and final states with activation energy E_{th}. In this model, the resonance-exchange integral (H_{ad}) gives the degree of coupling between the two ground states.

For Class II complexes, the following relationships have been derived to evaluate the degree of charge delocalization based on the features of their IVCT bands.[31,37,38] For symmetric mixed-valence complexes:

$$\nu_{op} = 4 E_{th} \tag{1}$$

$$\Delta\nu_{1/2} = (2310\ \nu_{max})^{1/2} \tag{2}$$

For asymmetric mixed-valence complexes:

$$\Delta\nu_{1/2} = [2300\ (\nu_{max} - \Delta E^{o})]^{1/2} \tag{3}$$

Where $\Delta\nu_{1/2}$ is the bandwidth at the half-peak height in cm^{-1}, and ν_{max} is the energy of an IVCT band maximum in cm^{-1}.

The oscillator strength f of an IVCT band in a Class II mixed-valence complex can be theoretically derived as given in eq 4. Here, G refers to the degeneracy of the states concerned, e is the electric charge in C, and M is the charge-transfer transition dipole moment in C m.

$$f = 1.085 \times 10^{15}\, G\, \nu_{max} M^2/e^2 \tag{4}$$

$$M^2 = \alpha^2 e^2 d^2 \tag{5}$$

The oscillator strength f of a Gaussian band can be determined experimentally using eq 6. The delocalization coefficient or interaction parameter α^2, which is proportional to the amount of time spent by an electron in a given state, can then be derived from eqs 4, 5 and 6 as given in eq 7. Here ε is the extinction coefficient in $M^{-1}cm^{-1}$, and d is the transition dipole length in m.

$$f = 4.6 \times 10^{-9}\, \varepsilon\, \Delta\nu_{1/2} \tag{6}$$

$$\alpha^2 = (H_{ad}/\nu_{max})^2 = (4.2 \times 10^{-24}\, \varepsilon\, \Delta\nu_{1/2})/\nu_{max}\, d^2 \quad (7)$$

The dependence of the absorption maximum of an IVCT band on solvent has been used as a diagnostic test for a class II species. The solvent effect on the IVCT energy is given by eq 8.

$$\nu_{max} = \chi_i + \chi_o + \Delta E' + \Delta E^o \quad (8)$$

$$\chi_o = (m^2\, e^2/h\, c)(1/r - 1/d)(1/n^2 - 1/D_s) \quad (9)$$

$\Delta E'$ is the additional energy due to either a spin-orbit or a ligand-field splitting, χ_i is the inner rearrangement parameter and χ_o is the outer reorganizational parameter. The dielectric continuum treatment defines the outer-sphere reorganization energy χ_o according to eq 9, where m is the number of electrons transferred, r is the radius of the metal coordination sphere in m, n is the refractive index and D_s is the static dielectric constant of the solvent. If χ_o is assumed to be the only solvent-dependent term in eq 9, then ν_{max} may be expected to vary linearly with $(1/n^2 - 1/D_s)$ for a Class II complex.

Mixed-valence complexes can often also be characterized by CV. The electrochemical potential difference between two sequential redox processes, $\Delta E_{1/2} = [E_{1/2}(2) - E_{1/2}(1)]$, in a symmetric mixed-valence complexes such as **1a** is related to the degree of charge delocalization in the complexes. The comproportionation constant K_c of a symmetric binuclear complex such as $L_mM^{II}M^{III}L_m$ (eq 11) can be calculated from $\Delta E_{1/2}$ (eq 10). Here, $E_{1/2}(1)$ and $E_{1/2}(2)$ are the first and second oxidation potentials of $L_mM^{II}M^{II}L_m$, n is the number of electrons in each redox process, and F is the Faraday constant. Charge delocalization makes contribution to the magnitude of $\Delta E_{1/2}$ (therefore Kc) along with several other factors, such as statistical distribution, electrostatic repulsion, inductive factor.[38] Comparsion of $\Delta E_{1/2}$

(K_c) between the complexes having similar structures is often instructive with respect to the extent of charge delocalization. The magnitude of K_c has been used as a criterion for the classification of mixed-valence complexes.[38] Complexes with $K_c > 10^6$ are considered to belong to Class III complexes. In Class III complexes, the even distribution of charge between metal centers results in the breakdown of Hush model and solvent-independent absorption features. Most asymmetric mixed-valence complexes belong to either Class I or Class II because of the energy difference ΔE^o between the initial and final ground states (see Figure 7b).

Scheme 3

$$L_mM^{II}M^{II}L_m \xrightarrow[E_{1/2}(1)]{-e} L_mM^{II}M^{III}L_m \xrightarrow[E_{1/2}(2)]{-e} L_mM^{III}M^{III}L_m$$

$$L_mM^{II}M^{II}L_m + L_mM^{III}M^{III}L_m \overset{K_c}{\rightleftharpoons} L_mM^{II}M^{III}L_m$$

$$\Delta E_{1/2} = [E_{1/2}(2) - E_{1/2}(1)] \quad (10)$$

$$\ln(K_c) = nF(\Delta E_{1/2})/RT \quad (11)$$

Charge delocalization between the metal centers in mixed-valence complexes is influenced by the nature of the bridge linking the two metal centers. Conjugated bridges enhance the electronic interactions between the two metal centers. For example, the CV of diferrocenylacetylene Fc–C≡C–Fc shows two redox waves with $\Delta E_{1/2}$ of 0.13 V. The monocation $[Fc–C≡C–Fc]^+$ has an IVCT band with λ_{max} at 1560 nm.[43] On the other hand, only one redox wave occurs in the CV of 1,2-diferrocenylethane $Fc–CH_2CH_2–Fc$, in which the bridge is saturated.[44] The length of a bridge also greatly affects delocalization of charge between the two metal centers. Ribou and coworkers synthesized and characterized a series of

diferrocenylpolyenes Fc–$(CH{=}CH)_n$–Fc (n = 1 – 6).[45] They showed that as n increases from 1 to 3, $\Delta E_{1/2}$ decreases from 0.17 to ~ 0.10 V, and that the compound with a longer bridge (n = 4, 5 and 6) has only one redox wave. Other symmetric, bimetallic complexes of the type $L_mM–(C{\equiv}C)_n–ML_m$ show similar effects of the bridge length on charge delocalization.[46-51] Gladysz and coworkers have synthesized and electrochemically characterized a series of linear symmetric birhenium complexes **2**.[48,51] They showed that lengthening the carbon chain results in a smaller difference in the oxidation potentials between the two Re centers: $\Delta E_{1/2}$ = 0.53 V for n = 2, 0.38 V for n = 3, 0.28 V for n = 4, 0.19 V for n = 6, 0.1 V for n = 8 and 0 V for n = 10.

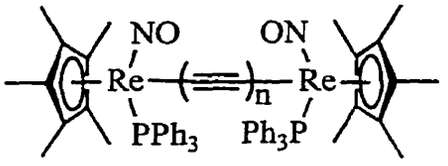

2 n = 2, 3, 4, 6, 8 and 10

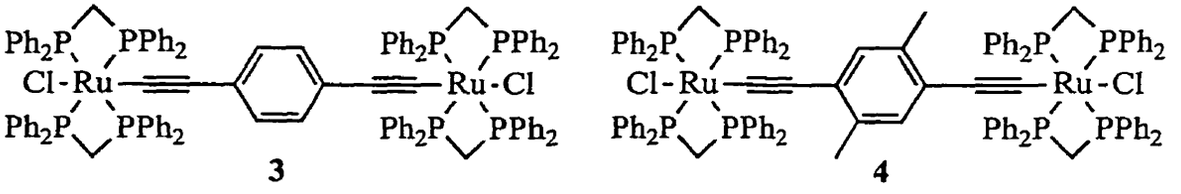

3 **4**

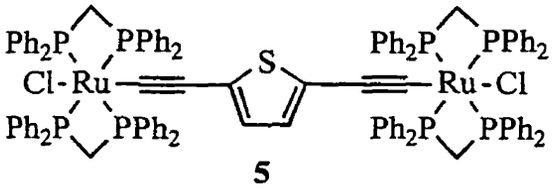

5

Colbert and coworkers have studied the effects of the electron density in the bridge on charge delocalization by the synthesis and characterization of a series of bimetallic ruthenium complexes **3** – **5** containing conjugated bridges of differing electron density.[52] The CVs of **3** – **5** all show two separated redox waves, assigned to sequential oxidations of the two ruthenium centers with a potential difference $\Delta E_{1/2}$ = 0.30 V for **3**, 0.33 V for **4** and 0.36 V for

5. The monocations of these complexes all have an IVCT band in the near-IR region. The calculated α^2 is 4.4×10^{-3} for $\mathbf{3}^+$, 6.5×10^{-3} for $\mathbf{4}^+$ and 8.9×10^{-3} for $\mathbf{5}^+$. Both results indicate that the more electron-rich thienyl bridge favors charge delocalization in this series.

There are some interesting trimetallic complexes **6** and **7** in which two ferrocenyl groups are linked via a metal bisacetylide bridge. The observation of two separated ferrocene redox waves with $\Delta E_{1/2} = 0.22$ V in **6** indicates a strong electronic interaction between the two ferrocenyl groups.[53,54] Complex **7**, on the other hand, has only one ferrocene redox wave, suggesting only a weak electronic interaction between the two terminal ferrocenyl groups.[55]

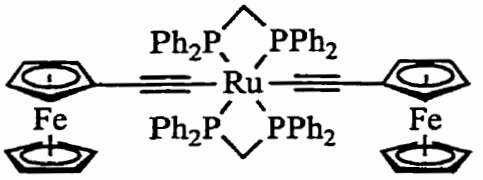

6

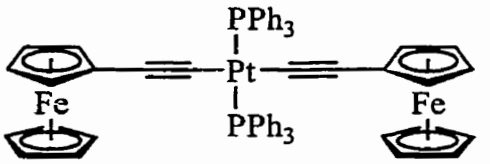

7

As shown in Figure 7b, charge transfer in an asymmetric mixed-valence complex should be affected by the energy difference ΔE^o between the initial and final ground states as well as by the nature of the bridge between two metal centers. It is impossible to measure ΔE^o experimentally, but the relative value of ΔE^o can be estimated from the electrochemical data.

As shown in Scheme 4, $M_1^{II}M_2^{III}$ corresponds to the higher energy state (B) in Figure 7b, and the oxidation potential of this species can be given as $\Delta E_{1/2}(1) + D$, in which D is a correction factor resulting from the presence of M_2^{III} instead of M_2^{II}. As given in eq 12 ΔE^o of an asymmetric complex should be linearly related to the potential difference $\Delta E_{1/2}$ between the two sequential oxidations of the metal centers.

The CVs of complexes **8a** and **8b** show two reversible redox waves with $\Delta E_{1/2} = [E_{1/2}(2) - E_{1/2}(1)] = 0.59$ V for **8a**, and 0.80 V for **8b**. The electronic spectra of $\mathbf{8a}^+$ and $\mathbf{8b}^+$ in

CH_2Cl_2 have IVCT bands with λ_{max} at 1590 nm ($\varepsilon = 3060\ M^{-1}cm^{-1}$, $\alpha^2 = 2.31 \times 10^{-3}$) for **8a**$^+$, and at 1295 nm ($\varepsilon = 1630\ M^{-1}cm^{-1}$, $\alpha^2 = 0.98 \times 10^{-3}$) for **8b**$^+$.[56] The complex with the smaller value of $\Delta E_{1/2}$ has the lower energy absorption and a higher value of α^2.

Scheme 4

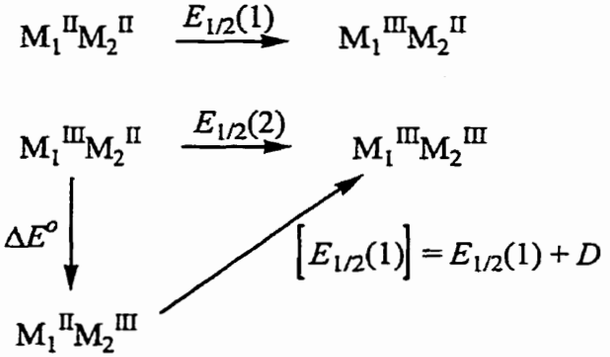

$$\Delta E^o = (E_{1/2}(2) - E_{1/2}(1)) + D = \Delta E_{1/2} + D \qquad (12)$$

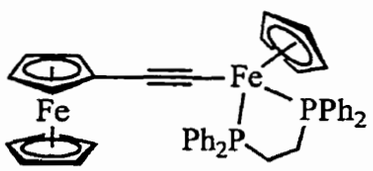

8a

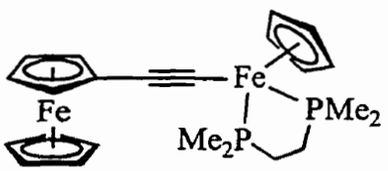

8b

The observation of low-energy absorptions due to LMCT transitions, as well as charge transfer from an organic donor to an organic acceptor, has been reported recently. Crutchley and coworkers synthesized a series of Ru^{III}-cyanamide complexes **9**, which have a LMCT band appearing in the near-IR region.[36] Lambert and Nöll prepared a set of six bistriarylamine derivatives with varying organic conjugated bridges **10** – **12**.[33] The CVs of these complexes contain two reversible redox waves due to the sequential oxidations of the amine groups. Oxidation of only one amine group results in the appearance of low-energy absorption bands in the near-IR region, indicative of effective charge delocalization between

the two organic redox centers. In complexes **9** and $\mathbf{10}^{+}$ – $\mathbf{12}^{+}$ Hush model has been used to evaluate the degree of charge delocalization.

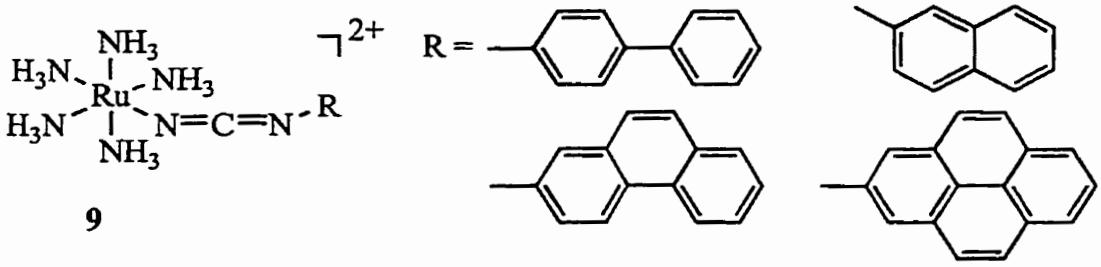

9

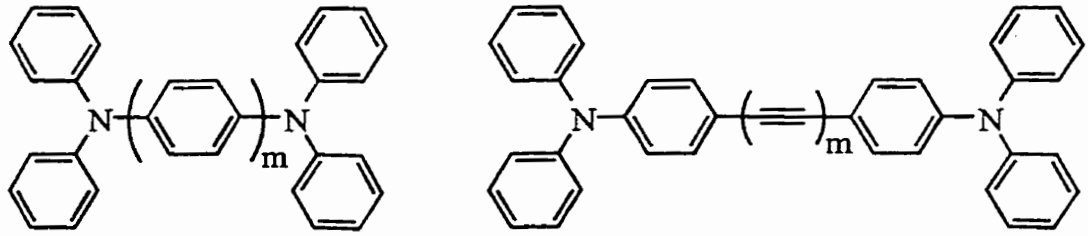

10 m = 1, 2 **11** m = 1, 2

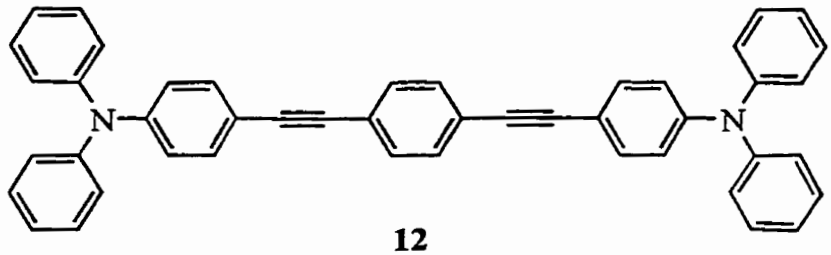

12

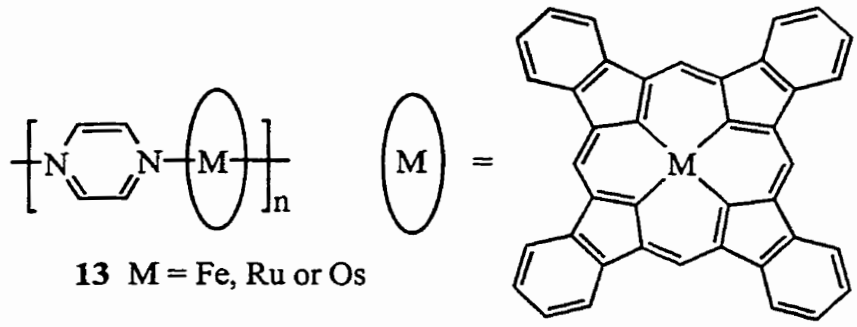

13 M = Fe, Ru or Os

Low-energy absorptions in the near-IR region have also been observed in conducting polymers. Oxidized organic conjugated polymers show very broad and strong near-IR absorption bands,[10,11] as do polymers such as **13**,[57] which contain Fe, Ru, or Os

phthalocyanines bridged by tetrazine or 2,5-dimethyltetrazine. These polymers exhibit high conductivities ($0.05 - 0.3$ S cm^{-1}) even without oxidative doping.

1.4 Transition-Metal σ-Acetylide Polymers

Transition-metal σ-acetylide polymers with the general structure $[-ML_m-C\equiv C-R-C\equiv C-]_n$ (M = Pd, Pt, Ru, Os etc., m = 2 or 4, R = conjugated organic groups), are of significant interest due to their rigid-rod backbone, high stability and possible extended π-conjugation.[58-76] It has been speculated that transition-metal σ-acetylide polymers may possess extended π-conjugation along the polymer backbone due to the overlap of metal dπ and alkyne pπ orbitals; thus, these polymers may have similar optical and electrical properties to organic conjugated polymers.[70] Experimental results have shown that some transition-metal σ-acetylide polymers have third order non-linearities and electrical conductivities.[77-79] More interestingly, transition-metal σ-acetylide polymers may combine the properties of the metal and the organic conjugated bridge, and could be superior to organic conjugated polymers in some applications. The nature of the ligands on the metal centers can alter the chemical and physical properties of the polymers, such as the solubility, stability, electrical conductivity and non-linearity. The rigid-rod structure also gives some of these polymers liquid-crystalline properties.

Many transition-metal σ-acetylide polymers have been synthesized by the Hagihara and Lewis groups.[58-67,71,72,75] Over 20 years ago, Hagihara and coworkers first synthesized soluble Pd and Pt polymers such as **14** via the copper halide-catalyzed coupling of *trans*-$M(PBu_3)_2Cl_2$ (**15**) and *trans*-$M(PBu_3)_2(C\equiv C-C\equiv CH)_2$ (**16**) in the presence of Et_2NH (Scheme 5).[58]

Scheme 5

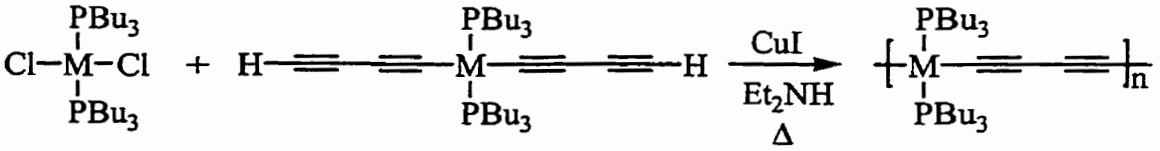

15 M = Pd, Pt **16** **14**

Lewis and coworkers have developed a new synthetic route using bis(alkynylstannyl) reagents, thus avoiding the need for amine solvents which may lead to the decomposition of the resulting polymers.[64,65,67,71,72,75,80-85] Reaction of $Me_3SnC{\equiv}C{-}p{-}C_6H_4{-}C{\equiv}CSnMe_3$ (**17**) with **15** affords polymers **18** as shown in Scheme 6.

Scheme 6

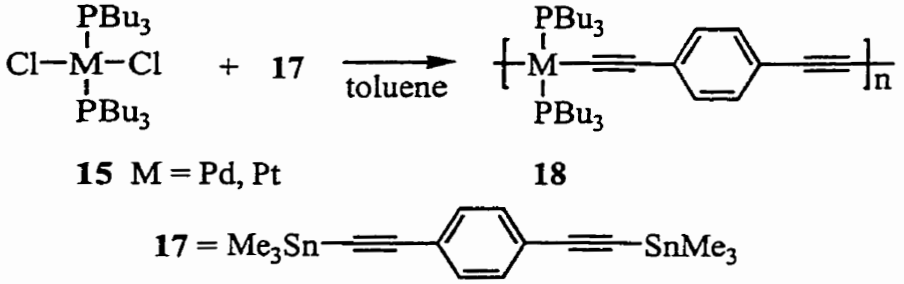

15 M = Pd, Pt **18**

17 = Me_3Sn—≡—C₆H₄—≡—$SnMe_3$

Scheme 7

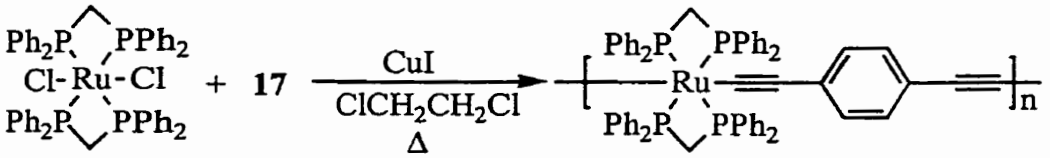

19 **20**

The Lewis approach has also been very successful for the preparation of polymers with the general structure $[{-}M(PR_3)_4{-}C{\equiv}C{-}R{-}C{\equiv}C{-}]_n$ (M = Fe, Ru and Os) [64,71,80,82] In the presence of catalytic copper halide, *trans*-$Ru(dppm)_2Cl_2$ (**19**) reacts with **17** yielding the soluble polymer **20** (Scheme 7).[71]

Many polymers analogous to **14** and **18** have been prepared using different acetylides. Lewis and coworkers have prepared polymers **21** – **26** with various conjugated bridges.[67,75,84] These polymers have been spectroscopically characterized, and their band gaps have been derived from their electronic spectra. They are wide band-gap semiconductors or insulators in their neutral states with band gaps around 3 eV (Table 2). The band gaps decrease with an increase in the conjugation length of the organic bridges. Polymer **24** has a terthienyl bridging group, and **26** has an anthracene bridge, and these polymers show lower band gaps than the others. Doping is expected to change the band gaps of metal acetylide polymers. There is only one example of this in the literature in which doping of **22** by exposure to iodine vapor or nitric acid results in the appearance of two new absorption bands with energy at 2.8 eV and ~2 eV respectively.[78]

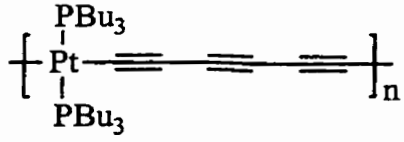

21

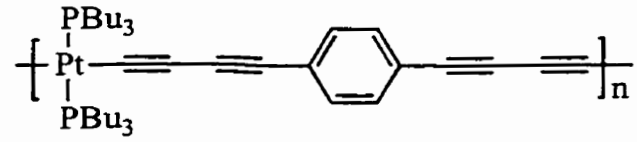

22

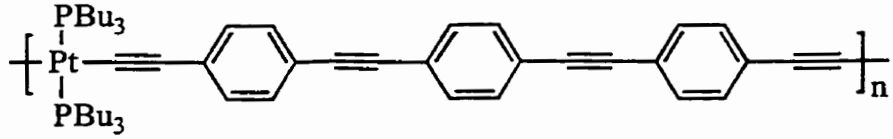

23

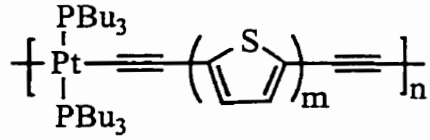

24 m =1, 2, 3

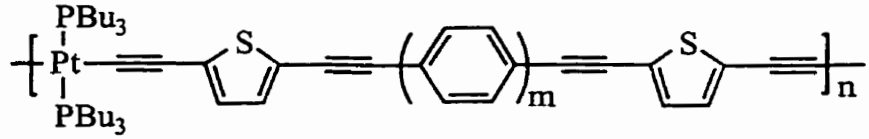

25 m = 1, 2

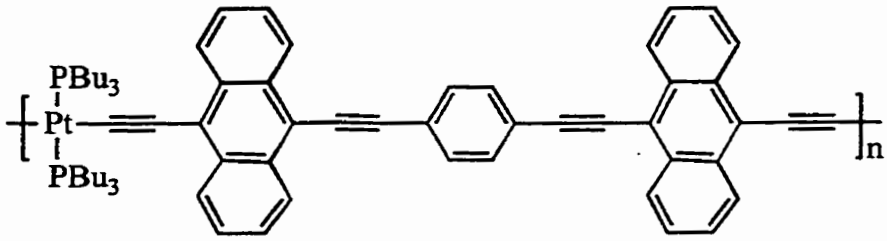

26

Efforts in this field have also been directed toward the preparation of σ-acetylide polymers containing different metal centers in their backbones. Takahashi and coworkers have prepared polymer **27**, which contains alternating Pd and Pt centers, by the CuI-catalyzed coupling of **15** (M = Pd) and **16** (M = Pt) in the presence of Et_2NH.[59] Using a similar approach Dixneuf *et al.* have synthesized the mixed Ru – Pd σ-acetylide polymer **28**.[86]

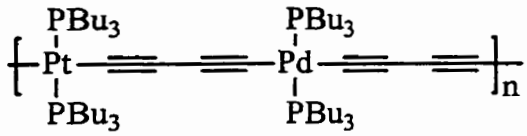

27

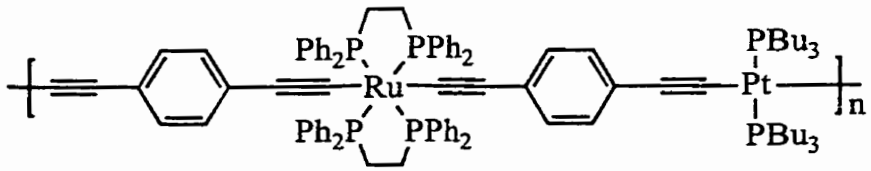

28

Elucidation of the extent of π-conjugation along the σ-acetylide polymer backbone is of central interest in these materials. Since extension of π-conjugation in these polymers depends on the overlap of metal dπ orbitals with alkyne pπ orbitals, both the metal and organic bridge can affect the extent of conjugation. Frapper and Kertesz have carried out a theoretical study on $[-ML_m-C{\equiv}C-R-C{\equiv}C-]_n$ (L = PR_3, CO or H; M = Ni, Pd, Pt, Rh, Co, Fe or Ru; m = 2 or 4; R = C≡C or *p*-C_6H_4) using extended Hückel theory.[70] They concluded that delocalization of the highest occupied crystal orbital (HOCO) extends over the metal centers

for both m = 2, 4, and that polymers containing 4-coordinate metal centers are better candidates for conduction by intrinsic doping than polymers with 6-coordinate metal centers.

Table 2. Band Gaps of Pt-Containing σ-Acetylide Polymers

Polymer	Band gap (eV)
$[-Pt(PH_3)_2-(C\equiv C)_2-]_n$	2.92[a]
$[-Pt(PH_3)_2-(C\equiv C)_4-]_n$	2.42[a]
$[-Pt(PH_3)_2-C\equiv C-p-C_6H_4-C\equiv C-]_n$	2.56[a]
$[-Pt(PH_3)_2-C\equiv C-p-(C_6H_4)_2-C\equiv C-]_n$	2.38[a]
$[-Pt(PBu_3)_2-(C\equiv C)_2-]_n$ **14**	3.23[b]
18	3.26[b]
23	3.11[b]
24 (m = 1)	2.80[b]
24 (m = 2)	2.55[b]
24 (m = 3)	2.40[b]
25 (m = 1)	2.70[b]
26	2.48[b]

[a] Calculated.[70] [b] Experimentally determined.[67,75,86]

The band gaps of the polymers, which they defined as the energy difference between the lowest unoccupied orbital (LUCO) and the highest occupied orbital (HOCO), vary between 2.16 eV and 3.18 eV, depending on the nature of the metal, ligands and organic

linkers. Without doping, these polymers are semiconducting or insulating. The calculated band gaps of some Pt-containing σ-acetylide polymers are summarized in Table 2, as well as the experimentally determined band gaps of closely related polymers.

1.5 Conjugated Polymers with Ferrocene in the Backbone

Ferrocene-containing polymers are attractive electrical and magnetic materials due to the well-known thermal and redox stability of ferrocene. Ferrocene-containing polymers have been prepared either by attaching ferrocene as a pendant group on the polymer backbone or incorporating it into the backbone. The latter approach has yielded polymers containing directly linked ferrocene centers,[87-91] as well as those containing saturated hydrocarbon,[92-95] alkene,[96] aromatic,[69,97-102] ER_2 (E = Si, Ge, and Sn), P and S bridges.[103-107] Poly(1,1′-ferrocenylene) **29**, in which ferrocene centers are directly linked, can be prepared using several different synthetic routes. Polycondensation of ferrocene radicals in the presence of peroxides yields a polymer with a molecular weight greater than 5000 g/mol, but the polymer also contains other residues such as $-CH_2-$ and –O– in the main chain.[87,89] Upon oxidation, this polymer becomes semiconducting with a conductivity of 10^{-6} – 10^{-8} S/cm. More structurally well-defined poly(1,1′-ferrocenylene) has been prepared either via the condensation of 1,1′-dilithioferrocene with 1,1′-diiodoferrocene,[90] or the reaction of dihaloferrocene with magnesium.[91] The latter yields crystalline poly(1,1′-ferrocenylene), which, upon oxidation with TCNQ, exhibits a conductivity of 10^{-2} S/cm.[91]

Soluble poly- and oligo(1,1′-ferrocenylenes) have been characterized by CV. The cyclic voltammogram of poly(1,1′-ferrocenylene) with a molecular weight less than 900 g/mol contains a broad redox feature between 0.2 and 0.8 V vs SSCE,[108] while short

oligo(1,1′-ferrocenylene) with less than 7 ferrocene units has a discrete redox wave for each ferrocene unit. Nishihara and coworkers have prepared a series of oligo(1,1′-dihexylferrocenylene) complexes **30** with up to 7 ferrocene units by reaction of disodium dihexylfulvalene with $FeCl_2(THF)_2$.[108] The CV of these oligomers reveals closely spaced $Fe^{II/III}$ waves, indicative of strong electronic interactions between adjacent iron centers.

29

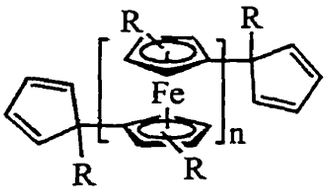

30 n = 1 – 7; R = *n*-hexyl

Ring-opening polymerization has been used with great success for the preparation of polymers with the main chain consisting of ferrocene and various ER_2 (E = Si, Ge and Sn), P and S_n bridges.[103-107] Ring-opening polymerization generally proceeds via a chain-growth mechanism, and yields polymers of high molecular weights. Manners and coworkers discovered that thermally induced ring-opening polymerization of the strained silaferrocenophanes (**31**), shown in Scheme 8, yields poly(ferrocenylsilanes) (**32**) with a molecular weight of 520,000 g/mol for R = Me.[104] Using this method they were able to prepare analogous polymers with other linking groups.[107] The CV of **32** exhibits two reversible oxidation waves of equal intensity, corresponding to initial oxidation at alternating iron sites followed by oxidation at the remaining sites.[103] Similar features occur in the cyclic voltammograms of analogous polymers with other linkers.[105] The appearance of two redox waves indicates that electronic interactions between adjacent iron centers exist in these materials.

Scheme 8

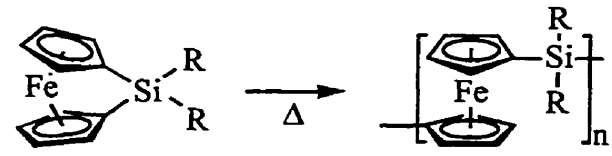

31 **32**

R = Me, Et, *n*-Bu and *n*-hexyl

Although the CV of such polymers shows that some electronic interactions exist among adjacent iron centers, the possibility of appreciable electron delocalization along the polymer chain is excluded by both electronic and Mössbauer spectroscopies.[106,107,109] The electronic spectra of polymers **32** with different R groups show similar absorption features in the visible region to those of ferrocene and monomers such as **31**, and The Mössbauer spectra of the partially oxidized **32** reveal discrete Fe^{II} and Fe^{III} environments. Conductivity measurements further support essentially localized electronic structures in these polymers. Polymers **32** are insulators with conductivities of $10^{-13} - 10^{-14}$ S/cm in the neutral state.[106,107] When doped with I_2 they become semiconductors with conductivities of $10^{-7} - 10^{-8}$ S/cm, consistent with a mechanism in which conductivity is due to electron hopping between localized redox sites.

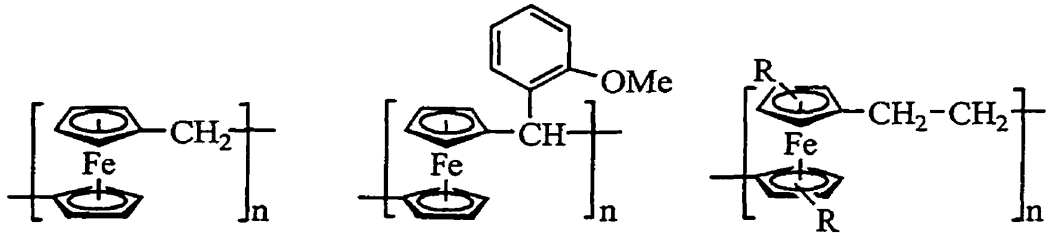

33 **34** **35** R = H, Me

Analogous polymers with saturated hydrocarbon bridges can be prepared either by step-growth or ring-opening polymerization. Polymer **33** with a methylene bridge and a

closely related polymer **34** were prepared via step-growth polymerization,[88,92,93] and **35** (R = H, Me) with an ethylene bridge was prepared from the corresponding ferrocenophanes via the ring-opening route.[94] The conductivity of the neutral **34** is 5×10^{-12} S/cm, and the partially oxidized polymer has a conductivity of $5 \times 10^{-8} - 2 \times 10^{-6}$ S/cm depending on the percentage of iron centers oxidized.[88] The CV of polymer **35** (R = Me) shows the presence of a single reversible oxidation wave, indicative of virtually no interaction between iron centers.[103]

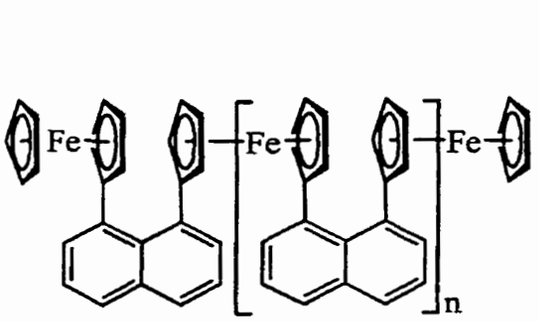

36

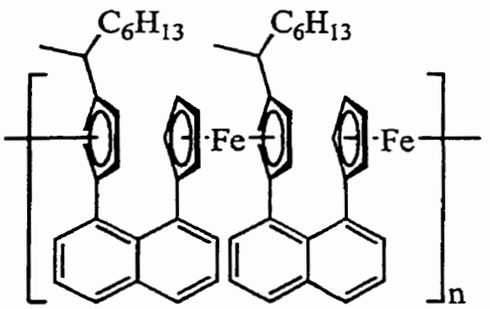

37

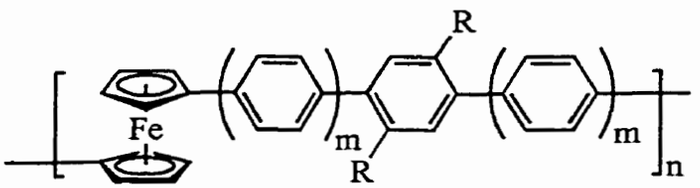

38 R = *n*-hexyl, *n*-dodecyl; m = 0, 1, 2 and 3

There has been significant interest in polymers with the main chain consisting of ferrocene groups linked via organic conjugated bridges such as aromatic, alkene or alkyne groups.[69,96-102] Such hybrid polymers may possess extended π-conjugation along the polymer chain, thus combining the properties of π-conjugated polymers and ferrocene. Rosenblum and coworkers first prepared oligomeric or low molecular weight polymer **36** by coupling zincated ferrocene with 1,8-diiodonaphthalene in the presence of a Pd(0) catalyst.[97] Later they developed a new route leading to the preparation of a closely related polymer **37**, which is soluble, and has high molecular weight (14,363 g/mol).[98] Both polymers consist of

stacked ferrocene moieties held together by a π-conjugated naphthalene bridge. Using Pd(0)-catalyzed polycondensation Rehahn and coworkers prepared a series of poly(1,1′-ferrocenylene-alt-*p*-oligophenylenes) **38**, in which the ferrocene moieties are linked via *p*-oligophenylenes with the number of the phenyl rings ranging from 1 to 7.[101]

Scheme 9

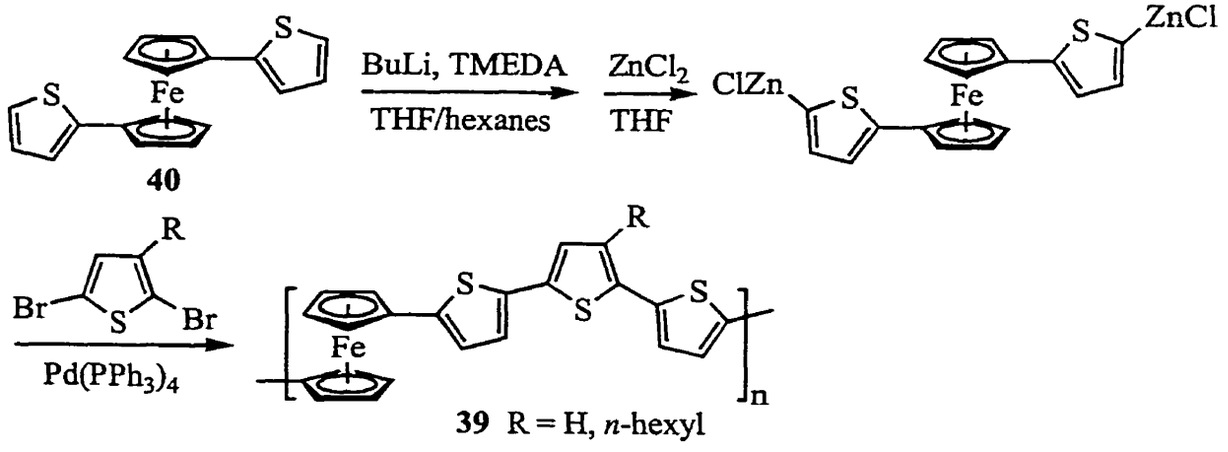

The Garnier group has prepared hybrid polymers **39** (R = H, *n*-hexyl) by the Pd(0)-catalyzed coupling of zincated 1,1′-dithienylferrocene **40** and the corresponding dibromothiophene (Scheme 9).[69,110] The main driving force behind this work has been the application of such hybrid polymers as magnetic materials. In the neutral state polymers **39** are diamagnetic, but oxidation of Fe^{II} to Fe^{III} results in the appearance of antiferromagnetic properties. For instance, when oxidized by NO_2BF_4, polymer **39** (R = H) can be attracted to a magnetic stirring bar. The bulk conductivities of the oxidized polymers have been measured, but the results are inconsistent. When doped with TCNE the measured conductivity of **39** (R = *n*-hexyl) is approximately 10^{-8} S/cm,[110] while a four-point probe conductivity measurement on **39** (R = H) when doped with $FeCl_3$, gives a value of 1×10^{-3} S/cm.[69]

Scheme 10

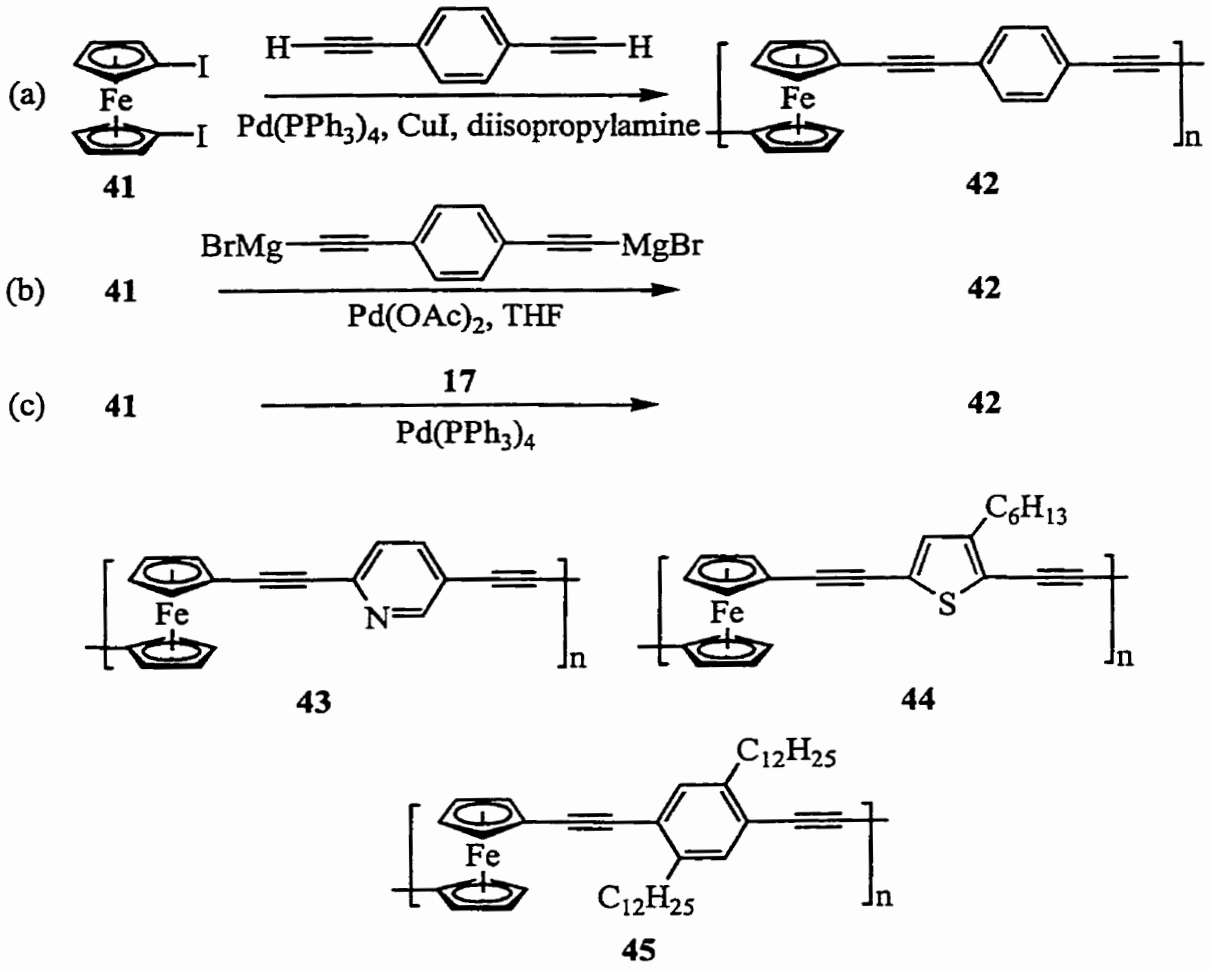

Yamamoto and coworkers have synthesized a poly(arylenethynylene)-type polymer **42** via the palladium-catalyzed coupling of 1,1′-diiodoferrocene (**41**) with HC≡C–*p*-C_6H_4–C≡CH or BrMgC≡C–*p*-C_6H_4–C≡CMgBr (Scheme 10a, b).[100] Lewis and coworkers have obtained the same polymer using alkynyltrimethylstannane **17** (Scheme 10c).[111] By varying aromatic groups Yamamoto was able to obtain a series of closely related polymers **43** – **45**.[100] The cyclic voltammograms of these polymers all contain a single broadened Fe^{II}/Fe^{III} redox wave, indicating that there is insignificant interaction between iron centers. Mössbauer characterization on the iodine adducts of polymer **42** yields the same conclusion. These

polymers all show an increase in conductivity when oxidized. Polymers **42** – **45** in the neutral state have conductivities of approximately 1.0×10^{-12} S/cm, while their iodine adducts have a conductivity of 1.3×10^{-4} S/cm for **42**, 1.3×10^{-6} S/cm for **43** and 6.0×10^{-7} S/cm for **44**.

1.6 Electropolymerization to Prepare Metal-Thiophene Hybrid Polymers

Electropolymerization has been extensively used in the synthesis of organic conjugated polymers such as polythiophene and polypyrrole.[10] Recently this approach has also been used to prepare hybrid polymers containing transition metal and thiophene units. This approach allows the direct preparation of polymer-modified electrodes for applications in electrocatalysis, chemical sensors and electrochromic displays.[112] Electropolymerization typically produces polymers which are insoluble and deposit as a film on the electrode surface. Thus electropolymerization and film growth require that the resulting polymer has moderate to high conductivities.

Hybrid metal-thiophene polymers can be obtained by anodic oxidation of transition-metal complexes bearing oligothiophenes with unsubstituted α positions. In order to obtain hybrid polymers with well-defined structures it is very important that the monomers be electropolymerized at potentials at which the metal centers are stable. Thus an important prerequisite for electropolymerization of such monomers is a relatively low oxidation potential. This may be achieved by the use of monomers which have either longer oligothienyl groups or electron-donating substituents. Shimidzu and coworkers have prepared porphyrin-containing polymers by electropolymerization of monomers **46** and **47**,[113] and Swager has prepared polythiophene–$Ru(bpy)_3^{n+}$ hybrids of monomer **48**,[114] in all cases, the monomers bear bi- or terthienyl groups.

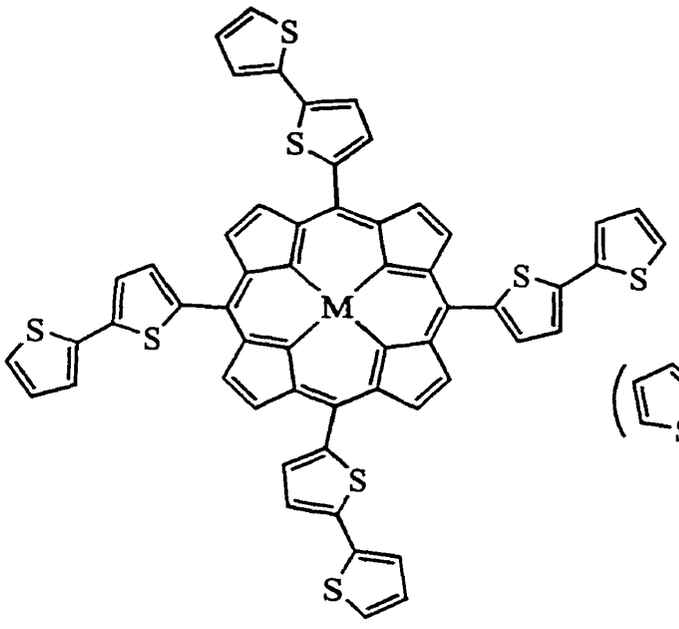

46 M =Zn, Pd

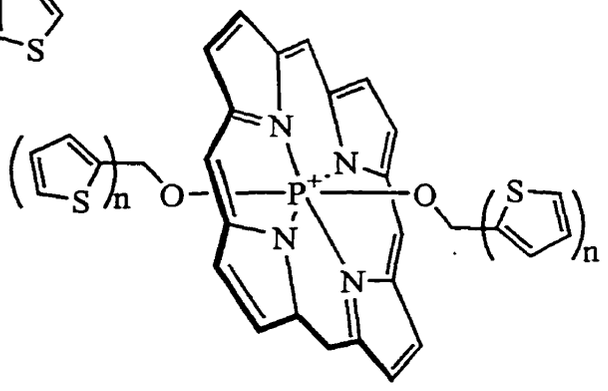

47 n = 2, 3

Swager and coworkers have also focused on the synthesis and subsequent polymerization of Schiff-base complexes such as **49a** and **49b**.[115,116] Electropolymerization of **49a** (M = Co) results in the deposition of a yellow film on the electrode surface. The CV of the thin polymer film contains quasireversible $Co^{II/III}$ wave at –0.1 V vs Fc^{+}/Fc and two larger polymer-based waves at 0.3 and 0.6 V, but only a fraction of the Co centers are electroactive in a thick film. *In situ* conductivity measurements indicates that there is no contribution from $Co^{II/III}$ to the conductivity, and that the polymer has a maximum conductivity of 34 S/cm at the second polymer oxidation potential.

By matching the oxidation potentials of the metal and organic groups in these polymers the electroactivity of the metal centers is enhanced. Electropolymerization of **49b** (M = Co) which has ethylenedioxy substituents results in a polymer which has broad redox waves due to both the $Co^{II/III}$ (–0.05 V vs Fc^{+}/Fc) and polymer-based oxidation processes (0.1 V). The conductivity profile of this polymer shows a broad trace increasing from

approximately –0.4 V through a maximum at –0.05 V and a subsequent decrease to a plateau at higher potentials. The maximum conductivity of this polymer is 44 S/cm.

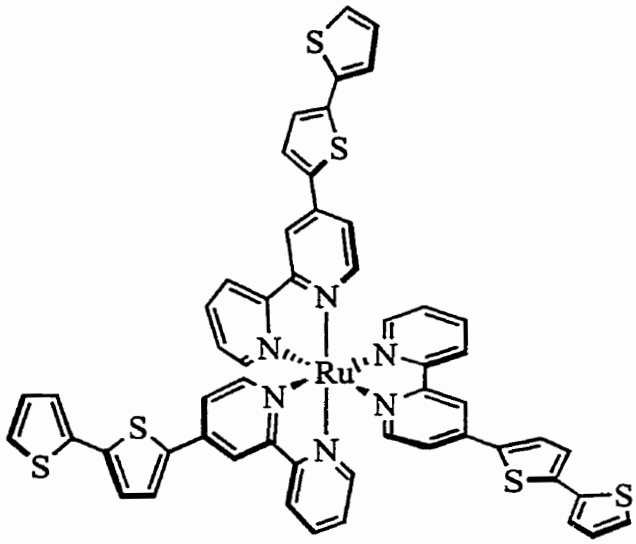

48

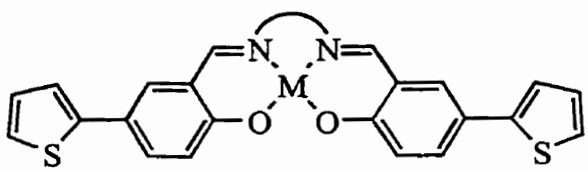

49a M = Co, Cu, Ni, UO_2

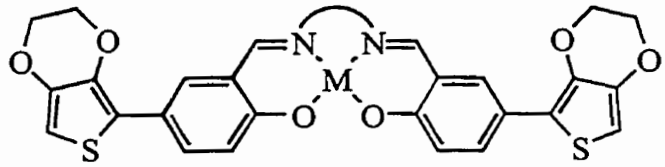

49b

Concurrent with the work reported in this thesis, Higgins and coworkers also reported electropolymerization of **50** and **51**.[117] In both cases they obtained dark films in which the ferrocenyl groups are not electrochemically accessible.

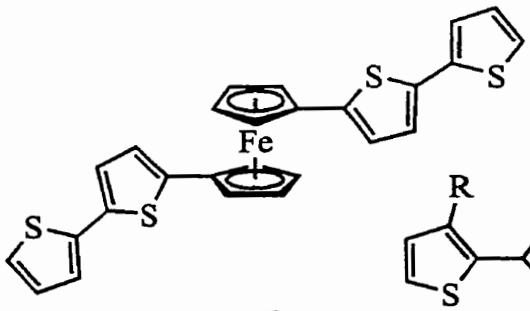

50

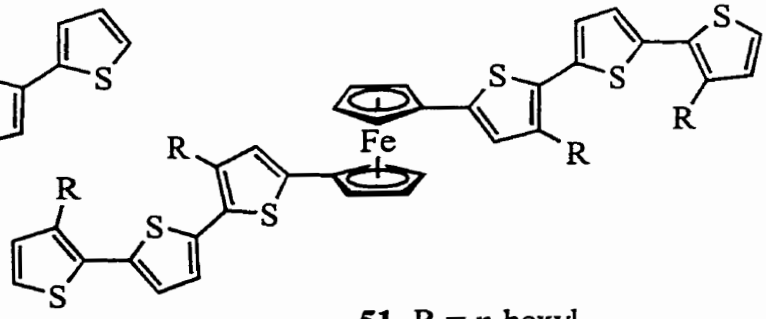

51 R = *n*-hexyl

1.7 Goals and Strategies

As discussed in this Chapter many hybrid polymers with a backbone consisting of transition-metal centers and organic conjugated fragments have been prepared. Such polymers possess extended π-conjugation along the polymer backbone due to the dπ – pπ orbital overlap between the metal and organic fragments, and in some cases demonstrate similar electrical properties to organic conjugated polymers. Many show a significant increase in their electrical conductivity when oxidized; however, the conductivity is often in the range of 10^{-2} – 10^{-7} S/cm, far lower than that of doped organic conjugated polymers.[69,84,88,91,100,110]

Conductivity in such hybrid polymers can result from two possible mechanisms: electron hopping between adjacent metal centers, or charge delocalization over both metal and organic fragments. The contribution from electron hopping is expected to be least dependent on the dπ – pπ overlap between the metal and organic fragments, and to decrease dramatically with increasing distance between adjacent metal centers. On the other hand, charge delocalization is expected to have a greater impact if the energy levels and symmetries of the frontier orbitals of the metal and organic fragments favor the dπ – pπ overlap. The work presented in this thesis focuses on understanding the factors which influence the extent of charge delocalization and conductivity in such hybrid polymers.

The strategies exploited in this thesis include the synthesis of polymerizable monomers containing both transition metal and conjugated organic fragments which show significant charge delocalization between the metal and organic components. Complexes, containing oligothienyl groups and metal centers, such as ferrocene, bisethynylferrocene or ruthenium bisacetylide (Figure 8), are targeted as monomers since they can be

electropolymerized via the oxidative coupling at the unsubstituted α positions of thiophenes. Such monomers may be synthesized by coupling a metal halide complex with an oligothiophene bearing suitable functional groups in the presence of Pd(0), Pd(II) or/and CuI catalyst, as shown in Schemes 5, 6, 7, 9 and 10.

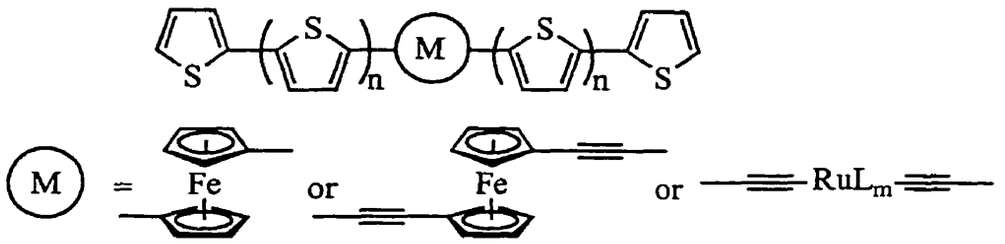

Figure 8. General structures of monomers targeted in this thesis.

Polymers prepared from these monomers may exhibit several relevant charge-transfer processes such as IVCT, LMCT and MLCT. Analysis of these charge-transfer processes can also be carried out on the monomers as well as on model complexes such as Fc^+/Fc–≡–RuL_n–≡–Fc/Fc^+ and Fc^+/Fc–≡–R–≡–Fc/Fc^+ (R = oligothiophene). The electronic interactions between the two ferrocenyl groups over a ruthenium bisacetylide bridge and an oligothiophene can be probed by electrochemical and spectroscopic methods. Analysis of electrochemical and spectroscopic data using Hush theory is expected to give insight into the extent of charge delocalization in these complexes.

The targeted monomers are expected to be electroactive due to redox processes involving both the metal and oligothienyl groups. The charge delocalization due to LMCT and MLCT processes in these monomers at different oxidation levels can then be assessed using electronic spectroscopy and CV. These results can be used to guide the optimization of

charge delocalization in these monomers. Varying the ligands on the metal centers, and altering the conjugation length of the oligothienyl groups allows for the optimization of charge delocalization.

1.8 Scope

The syntheses and characterization of a series of ruthenium bis(ferrocenylacetylide) complexes $RuL_4(C{\equiv}CFc)_2$, and their mono- and dications are described in Chapter 2. The results show that the ruthenium bisacetylide bridge allows electronic interaction between two terminal ferrocenyl groups, and that the interaction can be enhanced by an increase in the electron density on the ruthenium center. Chapter 3 covers the syntheses and characterization of ruthenium monoacetylide (*trans*-$Ru(dppm)_2(Cl)(C{\equiv}C{-}R)$ (R = 2-oligothienyl) and bisacetylide (*trans*-$Ru(dppm)_2(C{\equiv}C{-}R)_2$) complexes. Complexes which contain sufficiently long conjugated oligothienyl groups electropolymerize and form electroactive and electrochromic films. An intense low-energy absorption due to an oligothienyl-to-Ru(III) charge-transfer transition in the monooxidized complexes occurs, indicating electronic delocalization between the metal and organic fragments in these monocations.

The preparation, electrochemical and spectroscopic characterization of a series of mono- and bis(ferrocenylethynyl)oligothiophene complexes are described in Chapter 4. Changing the conjugation length and substituents of the oligothienyl group affects the degree of charge delocalization between the ferrocenyl and oligothienyl groups. Matching the oxidation potential of the metal center to that of the oligothienyl group enhances charge delocalization. Chapter 5 describes the preparation and electropolymerization of a series of

bis(oligothienyl)ferrocene complexes, and the spectroscopic and electrochemical characterization of these compounds and their electropolymerized films.

In Chapter 6, the copper(I) halide-catalyzed trans – cis isomerization of $RuCl_2(dppm)_2$ is described. A mechanism for the catalytic isomerization is proposed on the basis of the solid-state molecular structure of a reaction intermediate $[\{cis\text{-}RuCl_2(dppm)_2\}_2Cu][CuCl_2]$, and the identification of several other intermediates by NMR spectroscopy. Finally, Chapter 7 summarizes some suggestions for future work.

Chapter 2 Charge Delocalization in Ruthenium(II) Bis(ferrocenylacetylide) Complexes

2.1 Introduction

Conjugated transition-metal σ-acetylide polymers will only be highlyconductive if charge carriers can be delocalized over both the metal and organic fragments. Since many organic conjugated oligomers and polymers delocalize charge very well, it is important to find suitable metal bridging groups. Metal bisacetylide bridges are good candidates because they can be stable under the oxidizing conditions which are typically used to dope conducting polymers. They are also synthetically accessible for a large number of different metal-ligand combinations.[118] Charge delocalization over a metal bisacetylide bridge can be probed by examining the electrochemical and spectroscopic behavior of molecules in which the bridge spans two redox-groups. The Wolf group and others have recently demonstrated that ruthenium bisacetylide complexes show electronic interaction between terminal redox groups, suggesting that such bridges are capable of delocalizing charge.[53,54]

This Chapter examines the effect of the ancillary ligands on the ruthenium on the electronic interactions between the terminal ferrocenyl groups in a series of ruthenium bis(ferrocenylacetylide) complexes **52** – **57**. The effect of isomerization at the ruthenium is also evaluated by comparing the electronic properties of the cis complex **52** with those of the closed related complex **53**.

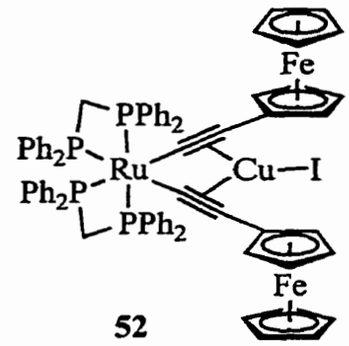

52

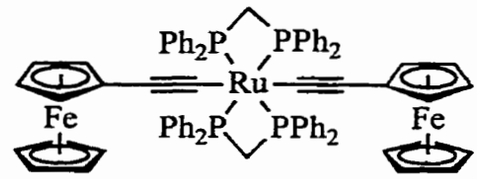

53

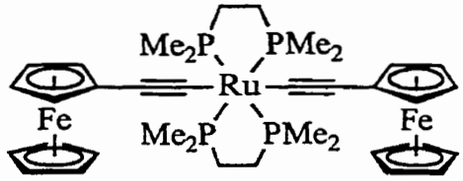

54

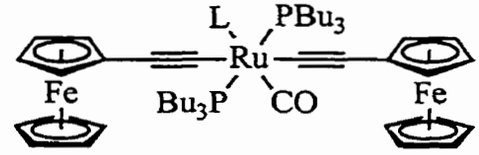

55 L = CO
56 L = py
57 L = $P(OMe)_3$

2.2 Experimental

General. *trans*-$RuCl_2(dppm)_2$ (**19**),[119] *trans*-$RuCl_2(dmpe)_2$ (**58**),[119] *cis*-$RuCl_2(dppm)_2$ (**59**),[120] $FcPF_6$,[121], ethynylferrocene[122] and $FcC{\equiv}CSn(n\text{-}Bu)_3$ (**60**)[53] were all prepared using literature procedures. Complex **53** and its dication were previously prepared by the Wolf group, but were not characterized by near-IR spectroscopy.[53] Complexes **55** – **57** were prepared by Olivier Clot in the Wolf group. All other reagents were purchased from either Strem Chemicals or Aldrich and used as received. Electronic absorption spectra were recorded on a UNICAM UV2 UV-vis spectrometer. Near-IR spectroscopic data were obtained on a Varian Cary 5 spectrometer. Extinction coefficients and absorption maxima for overlapping near-IR bands were determined by fitting the data using multiple Gaussian curves. IR data were collected on a UNICAM Galaxy Series FTIR 5000 spectrometer. ^1H, ^{13}C and $^{31}P\{^1H\}$ NMR experiments were performed either on a Bruker CPX-200, Varian XL-300 or Bruker WH-400 spectrometer. Spectra were referenced to residual solvent (^1H, ^{13}C) or

external 85% H_3PO_4 (^{31}P). Elemental analyses were performed by Peter Borda in this department. Electrochemical measurements were conducted on a Pine AFCBP1 bipotentiostat using a Pt disc working electrode, Pt wire-coil counter electrode and saturated calomel reference electrode (SCE). The supporting electrolyte was 0.1 M $[(n\text{-Bu})_4N]PF_6$, which was purified by triple recrystallization from ethanol and dried at 90 °C under vacuum for three days. Decamethylferrocene (–0.12 V vs SCE) was used as an internal reference. CH_2Cl_2 used in CV was dried by refluxing over CaH_2.

[*cis*-Ru(dppm)$_2$(C≡CFc)$_2$]CuI (52). To a solution of **60** (1.10 g, 2.20 mmol) in CH_2Cl_2 (70 mL) under a nitrogen atmosphere was added **59** (0.82 g, 0.87 mmol) and CuI (0.26 g, 1.4 mmol). The red-brown suspension was stirred at 25 °C for 72 h. The cloudy solution was filtered through Celite 545, the volume of the solution was reduced to approximately 4 mL, and hexanes (100 mL) were added to precipitate a yellow-brown solid. The solid was dissolved in CH_2Cl_2 (50 mL), and a solution of sodium iodide (2.1 g, 14 mmol) in acetone (30 mL) was added. The solution turned cloudy after the solution was stirred at room temperature for 2 h. After the solvent was removed chloroform (20 mL) was added. The undissolved solids were removed by filtration, the filtrate was concentrated, and hexanes were added until the solution was almost saturated. A yellow-orange crystalline solid precipitated after the solution was cooled to –10 °C. The solid was dissolved in a small amount of choroform and reprecipitated by adding hexanes. The resulting powder was dried *in vacuo* at room temperature for 3 days. Yield: 0.94 g (72%). ^1H NMR (400 MHz, CD_2Cl_2): δ 8.23 (m, 4H, Ph), 8.03 (m, 4H, Ph), 7.50 – 7.15 (m, 24H, Ph), 6.86 (t, J_{HH} = 7.1 Hz, 4H, Ph), 6.39 (t, J_{HH} = 8.2 Hz, 4H, Ph), 4.67 (m, 2H, C_5H_4), 4.72 – 4.62 (m, 2H, CH_2), 4.40 – 4.30 (m, 2H, CH_2), 4.05 (s, 10H, Cp), 3.95 (m, 4H, C_5H_4), 3.88 (m, 2H, C_5H_4). $^{31}P\{^1H\}$ (81.015 MHz,

$CDCl_3$): δ –16.9, –17.5 (AA'BB', J_{PP} = 28 Hz). Anal. Calcd for $C_{74}H_{62}IP_4CuFe_2Ru$: C 60.12; H 4.23. Found: C 60.38; H 4.25.

[*trans*-Ru(dmpe)$_2$(C≡CFc)$_2$] (54). To a solution of **60** (1.00 g, 2.00 mmol) in chlorobenzene (70 mL) under a nitrogen atmosphere was added **19** (0.31 g, 0.66 mmol) and CuI (8 mg, 0.04 mmol). The red-brown suspension was heated at reflux overnight. The cloudy solution was filtered through Celite 545, the volume of the solution was reduced to approximately 4 mL, and diethyl ether (100 mL) was added to precipitate a yellow-brown solid, which was washed thoroughly with diethyl ether. The product was recrystallized from CH_2Cl_2/haxanes, and the crystalline solid contained 0.5 equivalent CH_2Cl_2. Yield: 0.38 g (69%). ^{1}H NMR (400 MHz, $CDCl_3$): δ 5.29 (s, 1H, CH_2Cl_2), 4.03 (s, 10H, Cp), 3.97 (s, 4H, C_5H_4), 3.89 (s, 4H, C_5H_4), 1.68 (s, 8H, CH_2), 1.55 (s, 24H, CH_3). Anal. Calcd for $C_{36.5}H_{51}ClP_4Fe_2Ru$: C 50.86; H 5.96. Found: C 50.79; H 6.12.

{[*cis*-Ru(dppm)$_2$(C≡CFc)$_2$]CuI}[PF$_6$]$_2$ (52^{2+}[PF$_6$]$_2$) A solution of **52** (67 mg, 0.046 mmol) in CH_2Cl_2 (4 mL) was cooled to –78 °C. To this solution was added a solution of $FcPF_6$ (30 mg, 0.091 mmol) in CH_2Cl_2 (3 mL). The solution turned brick-red immediately. After the solution was stirred for 2 min at –78 °C, hexanes (40 mL) were added to precipitate a brick-red solid. The solid was collected by filtration, washed with hexanes, and dried *in vacuo* at 80 °C for 3 days. Yield: 71 mg (88%). Anal. Calcd for $C_{74}H_{62}CuF_{12}Fe_2IP_6Ru$: C 50.26; H 3.53. Found: C 50.30; H 3.53.

[*trans*-Ru(dmpe)$_2$(C≡CFc)$_2$][PF$_6$]$_2$ (54^{2+}[PF$_6$]$_2$). **54** (42 mg, 0.051 mmol) was dissolved in hot CH_2Cl_2 (15 mL) under N_2. To this solution was added $FcPF_6$ (34 mg, 0.103 mmol). The solution turned blue-purple immediately. After the solution was stirred for 20 min at room temperature, hexanes (50 mL) were added to precipitate a dark-blue solid. The

solid was collected by filtration, washed with hexanes, and dried *in vacuo* at 80 °C for 3 days. Yield: 54 mg (95%). Anal. Calcd for $C_{36}H_{50}F_{12}Fe_2P_6Ru$: C 38.98; H 4.54. Found: C 38.74; H 4.50.

[*trans,trans,trans*-Ru(PBu$_3$)$_2$(CO)$_2$(C≡CFc)$_2$][PF$_6$]$_2$ (55^{2+}[PF$_6$]$_2$). To a solution of **55** (56 mg, 0.057 mmol) in CH_2Cl_2 (2 mL) was added a solution of $FcPF_6$ (38 mg, 0.12 mmol) in CH_2Cl_2 (2 mL). The solution turned red immediately. After the solution was stirred for 30 min at room temperature, hexanes (40 mL) were added to precipitate a brick-red solid. The solid was collected by filtration, washed with hexanes, and dried *in vacuo* at 85 °C for 4 days. Yield: 64 mg (88%). Anal. Calcd for $C_{50}H_{72}F_{12}Fe_2O_2P_4Ru$: C 47.29; H 5.71. Found: C 47.15; H 5.55.

[*trans,trans,trans*-Ru(PBu$_3$)$_2$(CO)(py)(C≡CFc)$_2$][PF$_6$]$_2$ (56^{2+}[PF$_6$]$_2$). To a solution of **56** (47 mg, 0.046 mmol) in CH_2Cl_2 (2 mL) was added a solution $FcPF_6$ (30 mg, 0.091 mmol) in CH_2Cl_2 (2 mL). The solution turned purple-red immediately. After the solution was stirred for 10 min at room temperature, hexanes (30 mL) were added to precipitate a dark purple solid, which was isolated by filtration and washed with hexanes. The solid was collected by dissolving it in a small amount of CH_2Cl_2, removing the solvent and drying *in vacuo* at 90 °C for 7 days. Yield: 48 mg (80%). Anal. Calcd for $C_{54}H_{77}F_{12}Fe_2OP_4Ru$: C 49.10; H 5.88, N 1.06. Found: C 49.19; H 6.03; N 1.04.

***trans,trans,trans*-Ru(PBu$_3$)$_2$(CO)(P(OMe)$_3$)(C≡CFc)$_2$][PF$_6$]$_2$ (57^{2+}[PF$_6$]$_2$).** This complex was prepared as described for **56**$^{2+}$[PF$_6$]$_2$. Yield: 77%. Anal. Calcd for $C_{52}H_{81}F_{12}Fe_2O_4P_5Ru$: C 45.73; H 5.98. Found: C 45.27; H 5.85.

Reaction of 53 with CuI. To a solution of **53** (130 mg, 0.10 mmol) in CH_2Cl_2 (30 mL) was added CuI (38 mg, 0.20 mmol). After the suspension was stirred at 25 °C under

nitrogen for 24 h, the solution was filtered through Celite 545. The volume of the filtrate was reduced to approximately 1 mL, and hexanes (30 mL) were added to the solution to precipitate a yellow solid. The solid was collected by filtration, washed with hexanes, and dried *in vacuo* at room temperature overnight to obtain pure **52**. Yield: 130 mg (88%).

Reaction of 52 with $P(OMe)_3$. To a solution of **52** (150 mg, 0.10 mmol) in CH_2Cl_2 (25 mL) was added $P(OMe)_3$ (50 mg, 0.40 mmol). The solution was stirred at 25 °C under nitrogen for 2 days. During this time the solution became deeper red and cloudy. After this period, the volume of the solution was reduced to approximately 2 mL, and diethyl ether (20 mL) was added to the solution to precipitate an orange solid. The solid was collected by filtration, washed with diethyl ether, and dried *in vacuo* at 85 °C for 2 days. NMR indicated that the product was **53**. Yield: 82 mg (64%).

Crystallographic Study. Data collection and structure determination were carried out by Dr. Glenn Yap (Department of Chemistry and Biochemistry, University of Windsor, Ontario). Single crystals of **52**·2($CHCl_3$) were obtained by slow crystallization from layered $CHCl_3$ and hexanes. Crystal data and refinement parameters were summarized in Table 3. Suitable crystals were mounted on thin, glass fibres with epoxy cement. The systematic absences in the diffraction data and the unit-cell parameters were uniquely consistent with the reported space group. The structure was solved by direct methods, completed by Fourier syntheses, and refined by full-matrix least squares procedures based on F^2. The data were corrected for absorption by using redundant data at different effective azimuthal angles. Two symmetry-unique molecules of cocrystallized chloroform solvent were located in the asymmetric unit of **52**·2($CHCl_3$). All non-hydrogen atoms were refined with anisotropic displacement coefficients. All hydrogen atoms were treated as idealised contributions. All

software and sources of atomic scattering factors are contained in the SHELXTL (5.03) program library.[123]

Table 3. Summary of Crystallographic Data for **52**·2($CHCl_3$)[a]

Empirical formula	$C_{76}H_{64}Cl_6CuFe_2IP_4Ru$	T_{max}/T_{min}	1.695
Formula weight	1717.06	T, K	296
Crystal system	Monoclinic	Radiation	MoKα (0.71073 Å)
Space group	$P2_{1/c}$	Diffractometer	Siemens CCD
Crystal color	Yellow–orange	Z	4
a, Å	17.7522(6)	μ(Mo Kα), cm^{-1}	16.4
b, Å	17.3529(5)	θ	1.45 – 22.50
c, Å	23.8798(7)	$R(F)$, %	5.24
β, deg	90.221(1)	$R(wF^2)$, %	12.5
V, $Å^3$	7350.7(4)	N_v/N_o	10.5
D (calcd), g cm^{-3}	1.552	GOF on F^2	1.08

[a] Quantity minimized = $R(wF^2) = \Sigma[w(F_o^2 - F_c^2)^2]/\Sigma[w(F_o^2)^2]^{1/2}$; $R = \Sigma|(F_o - F_c)|/\Sigma(F_o)$, $w = [\sigma^2(F_o^2) + (0.0563P)^2 + 23.7444P]^{-1}$; GOF = Goodness-of-fit.

2.3 Results and Interpretation

2.3.1 Syntheses and Structure

The ruthenium bisacetylide complex **53** has previously been synthesized by the Wolf group by the CuI-catalyzed coupling of **59** and **60**.[53] The synthesis of **53** is sensitive to both the amount of CuI used and to the reaction temperature. When catalytic CuI (5 mol%) is used

and the reaction is carried out in 1,2-dichloroethane at reflux, **53** is obtained in good yield. When a stoichiometric amount of CuI is used a mixture of two new complexes with very similar NMR spectra is obtained. Elemental analysis of the mixture suggests that the two products are $[Ru(dppm)_2(C{\equiv}CFc)_2]CuCl$ and $[Ru(dppm)_2(C{\equiv}CFc)_2]CuI$ (Scheme 11). By metathesis of the product mixture with NaI pure **52** is isolated. Complex **52** is obtained in 72% yield when the reaction is carried out at room temperature in CH_2Cl_2 for 3 days. Complex **52** may also be prepared in 70% yield from $FcC{\equiv}CSn(n\text{-}Bu)_3$ (**60**) and *trans*-$RuCl_2(dppm)_2$ (**19**) in the presence of excess CuI at room temperature.

Scheme 11

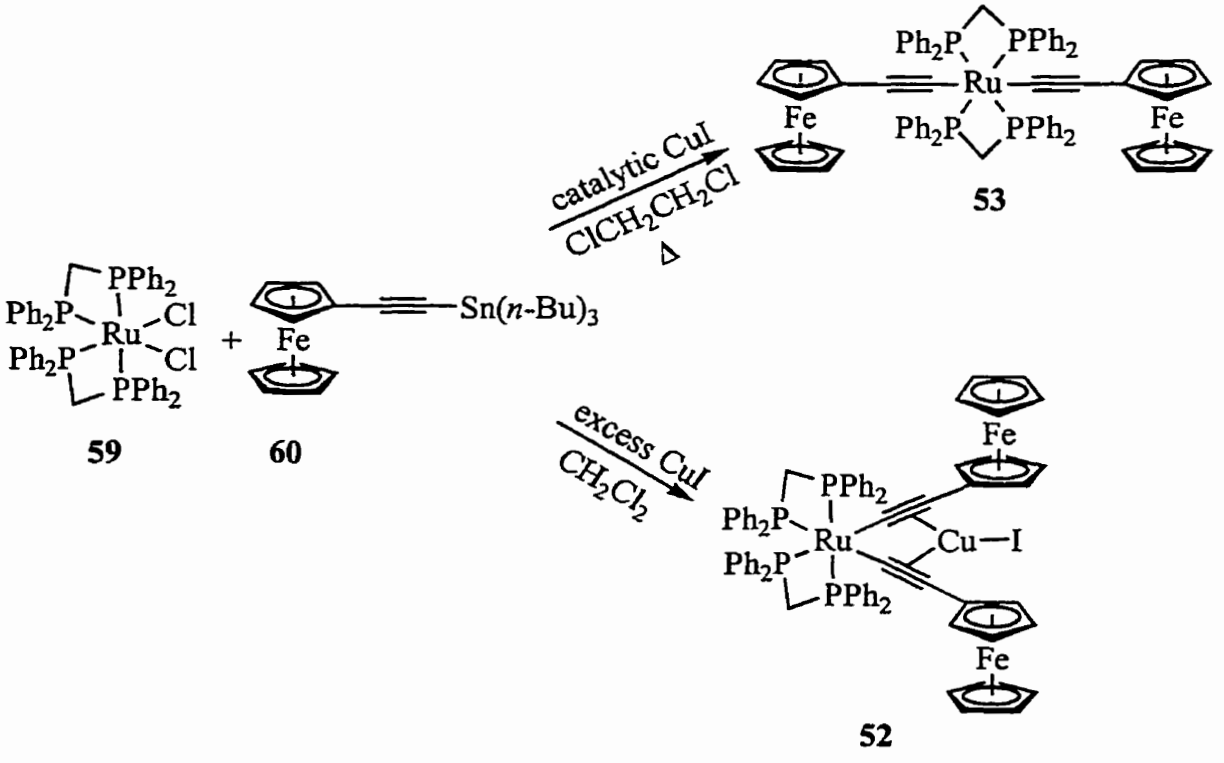

Less CuI and higher temperatures favor the formation of the trans complex, while excess CuI and lower temperatures produce the cis complex. The cis complex is found to decompose in $ClCH_2CH_2Cl$ at reflux. Complex **54** is prepared in 71% yield from the reaction of **60** and *trans*-$RuCl_2(dmpe)_2$ (**58**) at 132 °C using CuI (6 mol%) as catalyst.

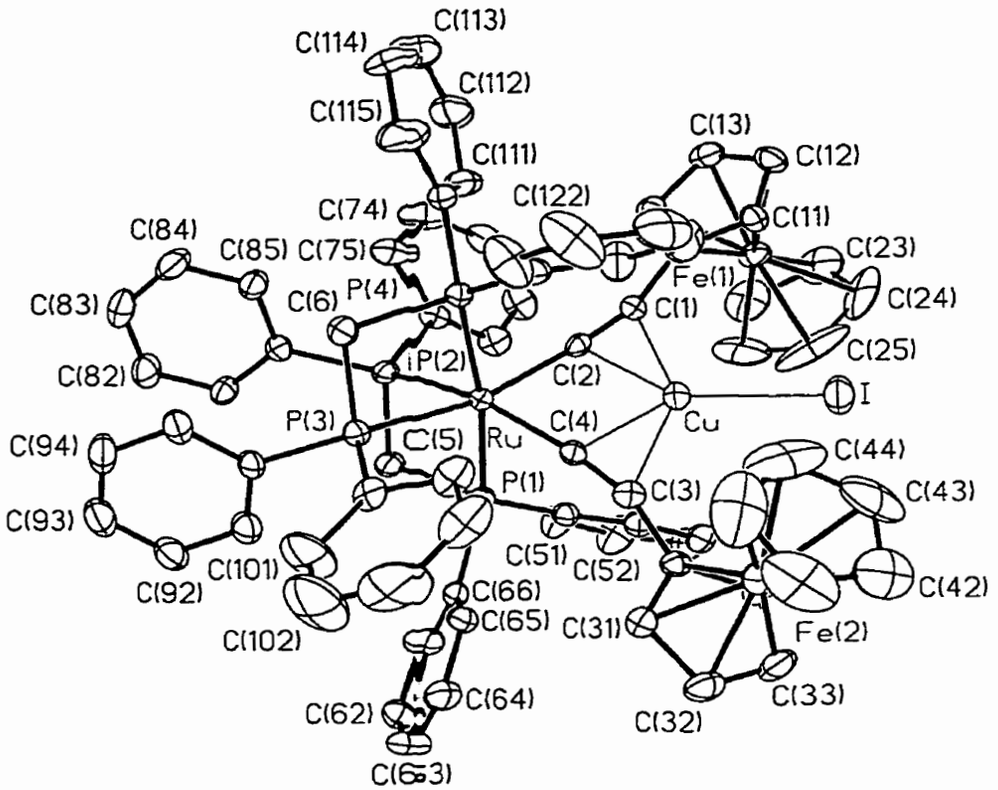

Figure 9. ORTEP diagram of the solid-state molecular structure of **52** (30% probability ellipsoids shown). Hydrogen atoms are omitted for clarity.

The solid-state molecular structure of **52**·2($CHCl_3$) shows that the ruthenium center is in a distorted octahedral environment, and that the ferrocenylacetylide ligands are in a cis orientation around the ruthenium (Figure 9). The CuI unit is bonded in an η^2 fashion to both acetylide bonds. Many complexes in which Cu is bonded in this manner to an acetylide bond are known;[124-128] however, there are only a few examples of organometallic bidentate bis(alkyne) ligands which chelate Cu^I, such as in [(η^5-$C_5H_4SiMe_3)_2Ti(C{\equiv}CSiMe_3)_2$]CuOTf.[129-132]

Table 4. Selected Bond Lengths in **52**·2($CHCl_3$) (Å)

Ru – P(1)	2.340(2)	Ru – C(4)	2.055(7)	Cu – I	2.529(1)
Ru – P(2)	2.368(2)	Cu – C(1)	2.229(7)	C(1) – C(2)	1.20(1)
Ru – P(3)	2.370(2)	Cu – C(2)	2.143(6)	C(1) – C(15)	1.467(8)
Ru – P(4)	2.330(2)	Cu – C(3)	2.264(8)	C(3) – C(4)	1.218(9)
Ru – C(2)	2.062(8)	Cu – C(4)	2.140(8)	C(3) – C(35)	1.452(7)

Table 5. Selected Bond Angles in **52**·2($CHCl_3$)·(deg)

P(1) – Ru – P(2)	71.62(6)	C(1) – Cu – C(4)	110.1(3)
P(1) – Ru – P(3)	102.81(7)	C(2) – Cu – C(3)	110.0(3)
P(1) – Ru – P(4)	172.04(7)	C(2) – Cu – C(4)	78.8(3)
P(2) – Ru – P(3)	95.08(8)	C(3) – Cu – C(4)	31.9(2)
P(2) – Ru – P(4)	102.78(7)	C(2) – C(1) – C(15)	160.9(7)
P(3) – Ru – P(4)	71.64(7)	C(2) – C(1) – Cu	70.1(5)
P(1) – Ru – C(2)	95.6(2)	C(15) – C(1) – Cu	128.7(4)
P(1) – Ru – C(4)	89.0(2)	C(1) – C(2) – Ru	168.9(7)
P(2) – Ru – C(2)	93.1(2)	C(1) – C(2) – Cu	78.0(4)
P(2) – Ru – C(4)	159.7(2)	Ru – C(2) – Cu	99.2(3)
P(3) – Ru – C(2)	161.4(2)	C(4) – C(3) – C(35)	161.1(7)
P(3) – Ru – C(4)	95.1(2)	C(4) – C(3) – Cu	68.4(5)
P(4) – Ru – C(2)	90.2(2)	C(35) – C(3) – Cu	128.9(5)

P(4) – Ru – C(4)	97.1(2)	C(3) – C(4) – Ru	168.7(6)
C(2) – Ru – C(4)	82.6(3)	C(3) – C(4) – Cu	79.6(5)
C(1) – Cu – C(2)	31.8(3)	Ru – C(4) – Cu	99.5(3)
C(1) – Cu – C(3)	141.8(3)		

Isomerization of 52 and 53. In order to examine the behavior of **52** in the absence of the chelated CuI, $P(OMe)_3$ is used to remove the CuI. This method has been used successfully to remove a CuOTf unit from the chelating bis(η^2-alkyne) unit of $[(\eta^5\text{-}C_5H_4SiMe_3)_2Ti(C{\equiv}CSiMe_3)_2]CuOTf$.[130] The major product of the reaction of **52** with excess $P(OMe)_3$ is **53** (Scheme 9) (64% isolated yield). When **53** is allowed to react with stoichiometric CuI for 24 h at room temperature, **52** is obtained in 88% isolated yield (Scheme 12).

Scheme 12

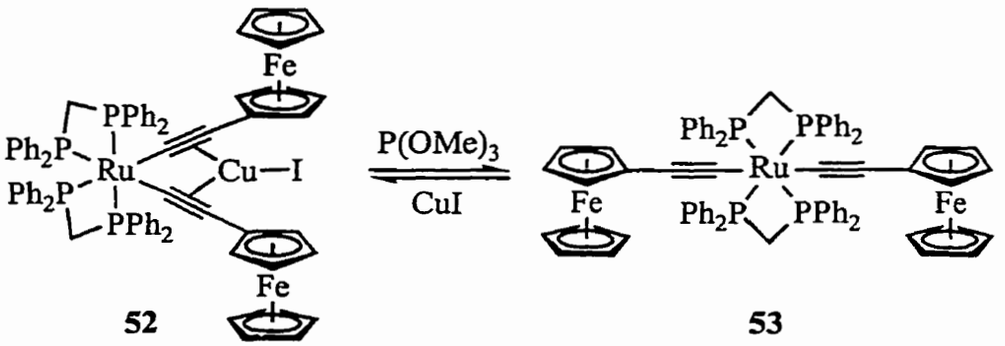

52 **53**

The CuI acts to "lock" the complex in the cis form with the bis(η^2-alkyne) units chelating the CuI. When the CuI is removed from **52** by complexation with $P(OMe)_3$, isomerization to the trans isomer occurs. It is possible that **53** and its cis isomer are in

equilibrium, with **53** being the favored form for steric reasons. The chelated CuI must stabilize the cis isomer and trap the cis form as **52**.

2.3.2. Electrochemistry

Table 6 summarizes the electrochemical data of the series **52** – **57**, as well as the literature data for **61**.[43] The electrochemical data of **55** – **57** are obtained by Olivier Clot.

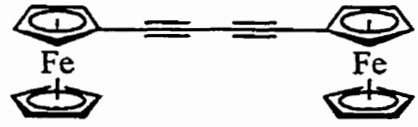

61

Table 6. Electrochemical Data for **52** – **57** and **61**

Complex	$E_{1/2}(1)^a$ (±0.01 V)	$E_{1/2}(2)^a$ (±0.01 V)	$E_{1/2}(3)$ or $E_{p,a}(3)^a$ (±0.01 V)	$\Delta E_{1/2}{}^b$ (±0.02 V)	$K_c{}^c$
52	0.20	0.34	0.97	0.14	260
53[d]	0.04	0.26	0.92	0.22	6100
54	–0.04	0.27	0.80	0.31	210000
55[g]	0.29	0.38	1.52[e]	0.09	35
56[g]	0.22	0.35	1.24[e]	0.13	170
57[g]	0.20	0.35	1.30[e]	0.15	370
61[f]	0.58	0.68		0.10	52

[a] Volts vs SCE, Pt working electrode, CH_2Cl_2 containing 0.1 M $[(n\text{-Bu})_4N]PF_6$, 20 °C. [b] $\Delta E_{1/2} = [E_{1/2}(2) - E_{1/2}(1)]$. [c] $\ln(K_c) = nF(\Delta E_{1/2})/RT$. [d] Ref.[53] [e] $E_{p,a}$ (irreversible wave). [f] Ref.[43]. [g] Measured by Olivier Clot.

The cyclic voltammogram of complex **52** in CH_2Cl_2 containing 0.1 M $[(n\text{-}Bu)_4N]PF_6$ at 20 °C, as shown in Figure 10a and b, contains three reversible waves of equal area between 0 and +1.1 V vs SCE. The waves at +0.20 V and +0.34 V are assigned to oxidation of the two ferrocenyl centers in **52**. The potentials for the two waves are close to those observed for the two ferrocenyl centers in **53**[53] and consistent with results observed for related complexes.[133] The potential difference between the first and second ferrocenyl oxidation waves in **52**, $\Delta E_{1/2}$, is 0.14 V ($\Delta E_{1/2} = E_{1/2}(2) - E_{1/2}(1)$). The redox wave at +0.97 V vs SCE in the CV of **52** is assigned to oxidation of the ruthenium center. This oxidation occurs at a slightly higher potential than the corresponding wave in the CV of complex **53**. When the scan range is extended to +1.4 V vs SCE, a smaller quasireversible wave (wave 4) is observed at +1.18 V, along with a reduction wave (wave 5) at +0.81 V. The relative intensity of wave 4 compared to waves 1 – 3 in the CV increases as the scan rate is decreased, suggesting that wave 4 may be due to oxidation of a product resulting from decomposition of oxidized **52**. Wave 5 may also be due to the decomposition of **52** upon oxidation. This feature is found to increase in intensity upon repeated scanning, possibly due to the deposition of the decomposition product on the working electrode.

The CV of **54** is very similar to that of **52** or **53**, containing three reversible redox waves with $E_{1/2}$ at –0.04, 0.27 and 0.80 V vs SCE in the range –0.4 – 1.10 V vs SCE (Figure 10c and d). All three redox potentials in **54** shift to lower potentials compared with those for **53** due to electron-donation from the dmpe ligands. The difference in the first and second redox potentials $\Delta E_{1/2}$ is 0.31 V for **54**. When the scan range is extended to 1.50 V, an irreversible oxidation wave (wave 4) at 1.44 V vs SCE is observed, along with reduction waves (waves 5 and 6) at 0.66 and 0.88 V vs SCE. This oxidation wave is possibly due to a

$Ru^{III/IV}$ oxidation process, and the waves 5 and 6 may result from reduction of the products formed in this process.

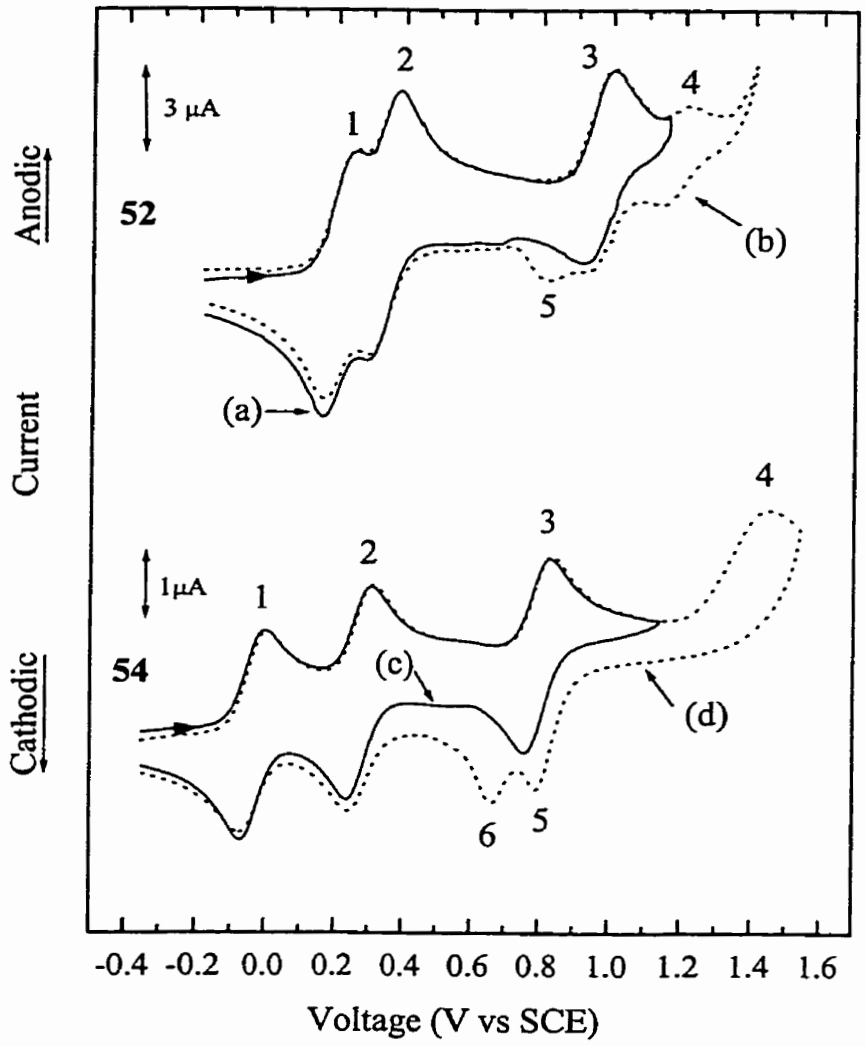

Figure 10. Cyclic voltammograms of **52** (a) –0.2 – 1.2 V and (b) –0.2 – 1.4 V vs SCE, and **54** (c) –0.3 – 1.1 V and (d) –0.3 – 1.5 V vs SCE in CH_2Cl_2 containing 0.1 M $[(n\text{-}Bu)_4N]PF_6$. Scan rate = 100 mV/s.

The cyclic voltammograms of complexes **55** – **57** contain two closely spaced waves which are assigned to oxidation of the two ferrocenyl centers, and the third irreversible wave which is assigned to the $Ru^{II/III}$ oxidation. The $Ru^{II/III}$ oxidation potential is higher than that observed for **52** – **54** due to increased backbonding with the carbonyl ligands in these complexes.

2.3.3 Spectroscopic Characterization

Chemical oxidation of one or both ferrocenyl groups in complexes **52** – **57** allows for the spectroscopic properties of the oxidized species to be determined and compared with those of the neutral analogs. Shifts in diagnostic absorptions in the IR region as well as the appearance of intervalence charge-transfer bands in the near-IR region are useful in evaluating the extent of electronic delocalization in these complexes.

The dications $\mathbf{52}^{2+}$ – $\mathbf{57}^{2+}$ are prepared by oxidation with two equivalents of $FcPF_6$ and are isolated as stable solids which are characterized by elemental analysis. The dications are shown to be paramagnetic at room temperature using the Evans method.[134] The monocations $\mathbf{52}^{+}$ – $\mathbf{57}^{+}$, prepared by dissolving equimolar masses of the neutral complex and the corresponding dication in an appropriate solvent, are in equilibrium with the corresponding neutral and dicationic species (Scheme 3). The equilibrium constants (K_c) for $\mathbf{52}^{+}$ – $\mathbf{57}^{+}$ at 20 °C are calculated from $\Delta E_{1/2}$ using the Nernst equation (eq 11) and are shown in Table 6.

2.3.3.1 Visible and IR Spectroscopies

The visible and IR spectroscopic data for the neutral and oxidized species are shown in Table 7. The visible spectra of the neutral complexes **52** – **57** all contain ligand-based

absorptions (data not shown) in addition to weaker bands (430 – 460 nm) which are assigned to metal d – d transitions. The monocations **52**$^+$ – **57**$^+$ all exhibit medium-intensity transitions in the visible region between 500 – 625 nm which are assigned to a ferrocenium-based ligand-to-metal charge-transfer (LMCT) excitation. This assignment is based on the similarity of the energy and intensity of the band to that observed for ferrocenium (620 nm).[135] The energy of the LMCT absorption of ferrocenium blue-shifts with the introduction of electron-withdrawing substituents,[135] and the absorption is observed at 510 nm in [Fc–C≡C–C≡C–Fc]$^+$ (**61**$^+$).[43] The LMCT absorptions for the monocations **52**$^+$– **57**$^+$ appear at higher wavelengths than the absorption for **61**$^+$, consistent with electron donation from the ruthenium moiety to the ferrocenium. In the visible spectra of the dications **52**$^{2+}$ – **57**$^{2+}$ the LMCT absorption blue-shifts with respect to the corresponding monocation, consistent with competition between the two ferrocenium groups for the electron density of the ruthenium center. Significantly, the absorption maximum for the LMCT transition is sensitive to the electronic nature of the ancillary ligands around the ruthenium center. Within the series of monocations of the trans substituted complexes, λ_{max} for the LMCT absorption decreases in the order: **53**$^+$ (616 nm) ≈ **54**$^+$ (625 nm) > **56**$^+$ (570 nm) ≈ **57**$^+$ (562 nm) > **55**$^+$ (514 nm). The same trend is observed within the series of dications.

The strong IR absorptions due to the C≡C and C≡O groups are sensitive to the electron density at the ruthenium center. The energy of the acetylide absorption ($\nu_{C\equiv C}$) increases in the series of trans bisacetylide complexes as the number of electron-withdrawing carbonyl ligands on the metal increases ($\nu_{C\equiv C}$: **53** ≈ **54** < **56** ≈ **57** < **55**). The energy of the absorption due to the carbonyl group ($\nu_{C\equiv O}$) is sensitive to the degree of backbonding with the ligand trans to the carbonyl. Thus $\nu_{C\equiv O}$ in **56**, which has a σ-donor (py) trans to the carbonyl,

is lower than $\nu_{C\equiv O}$ in **57** in which the trans $P(OMe)_3$ is a weak π-acceptor. The carbonyl absorption in **55** has the highest wavenumber in the series as the two trans carbonyls compete for backbonding with the same Ru d-orbital. The acetylide absorption in the spectra of the dications $\mathbf{52}^{2+}$ – $\mathbf{57}^{2+}$ shifts to lower energy than the absorption for the analogous neutral complexes as more electron density from the ruthenium is transferred to the acetylide bond via increased backbonding. This is also observed in the carbonyl stretching frequency in $\mathbf{55}^{2+}$ – $\mathbf{57}^{2+}$ which increases slightly relative to the neutral analogs as less electron density is available for backbonding with the carbonyl groups upon oxidation of the ferrocenyl groups.

Table 7. Visible and IR Spectroscopic Data for **52** – **57**

Complex	Visible λ_{max} (nm) (±5 nm); ε (M^{-1} cm^{-1}) (±5%)[a]	IR (KBr) ν (cm^{-1}) (±2 cm^{-1})
52	460 (850)	1994 (C≡C)
$\mathbf{52}^{+}$	500 (4700) (±10%)	
$\mathbf{52}^{2+}$	378 (7700), 476 (sh) (8500)	1948 (C≡C)
53	434 (2000)	2067 (C≡C)
$\mathbf{53}^{+}$	448 (sh) (2100), 616 (4100), 820 (sh), (1800)	
$\mathbf{53}^{2+}$	420 (sh) (5500), 560 (13 000)	1997 (C≡C)
54	350 (12000), 455 (1150)	2057 (C≡C)
$\mathbf{54}^{+}$	470 (sh) (3100), 625 (4100), 780 (4800)	
$\mathbf{54}^{2+}$	430 (sh) (5800), 585 (13000)	1964 (C≡C)
55[b]	450 (760)	2103 (C≡C), 1986 (C≡O)

55^{+}	390 (sh) (5100), 514 (6900) (±25%)	
55^{2+}	378 (10 000), 488 (12 000)	2067 (C≡C), 1994 (C≡O)
56^{b}	450 (920)	2079 (C≡C), 1940 (C≡O)
56^{+}	420 (sh) (3400), 570 (5300) (±15%)	
56^{2+}	394 (sh) (8500), 524 (12 000)	2030 (C≡C), 1954 (C≡O)
57^{b}	454 (810)	2084 (C≡C), 1974 (C≡O)
57^{+}	414 (sh) (3700), 562 (5300) (±10%)	
57^{2+}	394 (sh) (7500), 524 (9100)	2032 (C≡C), 1979 (C≡O)

[a] Solvent: CH_2Cl_2, ±5% except indicated. [b] Measured by Olivier Clot.

2.3.3.2 Near-IR Spectroscopy and IVCT

The near-IR spectroscopic data for the monocations and dications are shown in Table 8 and 9 respectively. None of the neutral complexes absorb in the near-IR region. The spectra of the monocations and dications all contain multiple absorption bands in the near-IR region. For these absorptions, the band widths at half maximum ($\Delta\nu_{1/2}$) are measured directly when possible, and using Gaussian peak fitting when the band is overlapped. The spectra are obtained in several solvents in order to study the solvent dependence of the observed transitions. The lower-energy band is obscured by solvent overtones in many solvents; therefore, the data for this band are shown only for spectra taken in CH_2Cl_2. The spectra of **52**$^{+}$ and **52**$^{2+}$ are only obtained in CH_2Cl_2 and 1,2-dichloroethane because the complexes decompose or react with other solvents used. For **54**$^{+}$ and **54**$^{2+}$ the measurements are only carried out in CH_2CH_2.

Table 8. Near-IR Spectroscopic Data for Monocations $\mathbf{52}^+ - \mathbf{57}^+$

Complex	ν_{max} (cm^{-1}) (±50 cm^{-1}); (λ_{max}, nm)[a]	ε (M^{-1} cm^{-1})	$\Delta\nu_{1/2}$ (cm^{-1}) (±50 cm^{-1})	α^2 ($\times 10^{-3}$)
$\mathbf{52}^+$	8420 (1190)	440 ± 40	2400	1.4 ± 0.2
	5630 (1775)	290 ± 30	2100	1.2 ± 0.2
	4320 (2315)	310 ± 30	810	
$\mathbf{53}^+$	4770 (2095)	6700 ± 300	3300	47 ± 5
	4380 (2285)	2700 ± 100	700	
$\mathbf{54}^+$	4914 (2035)	11000 ± 600	2625	60 ± 6
$\mathbf{55}^+$	8030 (1245)	2400 ± 600	3500	12 ± 4
	4380 (2285)	410 ± 100	540	
$\mathbf{56}^+$	6430 (1555)	3200 ± 500	2900	16 ± 3
	4410 (2265)	1100 ± 200	510	
$\mathbf{57}^+$	6520 (1535)	2900 ± 300	3100	15 ± 2
	4440 (2250)	1100 ± 100	530	

[a] CH_2Cl_2, 20 °C.

Table 9. Near-IR Spectroscopic Data for Dications $\mathbf{52}^{2+} - \mathbf{57}^{2+}$

Complex	Solvent[a]	ν_{max} ($\pm$50 cm^{-1}) (λ_{max}, nm)	ε ($M^{-1}cm^{-1}$) ($\pm$5%)	$\Delta\nu_{1/2}$ ($\pm$50 cm^{-1})	α^2 ($\times 10^3$) ($\pm$10%)
$\mathbf{52}^{2+}$	CH_2Cl_2	9620 (1040)	1600	3200	5.8
		4260 (2350)	150	950	
	$ClCH_2CH_2Cl$	9260 (1080)	1800	3600	7.5
$\mathbf{53}^{2+}$	CH_2Cl_2	6650 (1505)	7400	2800	33
		4470 (2240)	2400	480	
	CH_3COCH_3	6850 (1460)	7500	2800	32
	$ClCH_2CH_2Cl$	6540 (1530)	6400	2800	29
	o-Dichlorobenzene	6210 (1610)	5500	3800	36
	Chlorobenzene	6120 (1635)	5600	4400	42
	CH_3CN	6950 (1440)	7800	2600	31
	Nitrobenzene	6780 (1475)	10000	2100	34
	Trichloroethylene	6170 (1621)	6300	3500	37
	CH_3NO_2	6900 (1450)	8400	2600	33
$\mathbf{54}^{2+}$	CH_2Cl_2	6270 (1595)	9600	2560	40
		4400 (2270)	4700	430	
$\mathbf{55}^{2+}$	CH_2Cl_2	9220 (1085)	3700	2800	12
		4290 (2330)	340	840	
	o-Dichlorobenzene	9130 (1095)	3405	2900	12

	CH_3COCH_3	9620 (1040)	3230	2830	11
	CH_3CN	9620 (1040)	4200	2870	14
	Nitrobenzene	9440 (1060)	3980	2760	13
	CH_3NO_2	9520 (1050)	4075	2810	13
56^{2+}	CH_2Cl_2	7940 (1260)	5200	2900	21
		4360 (2295)	860	570	
	o-Dichlorobenzene	7880 (1270)	5340	2880	22
	CH_3COCH_3	8400 (1190)	3875	3160	16
	CH_3CN	8370 (1195)	4950	2980	20
	Nitrobenzene	8130 (1230)	4635	3151	20
	CH_3NO_2	8300 (1205)	4340	3060	18
57^{2+}	CH_2Cl_2	7880 (1270)	3500	3200	16
		4370 (2290)	620	640	
	o-Dichlorobenzene	7810 (1280)	2825	3420	14
	CH_3COCH_3	8200 (1220)	2900	3130	12
	CH_3CN	8230 (1215)	2375	3190	10
	Nitrobenzene	8030 (1245)	3505	3150	13
	CH_3NO_2	8130 (1230)	3190	3160	14

[a] 20 °C.

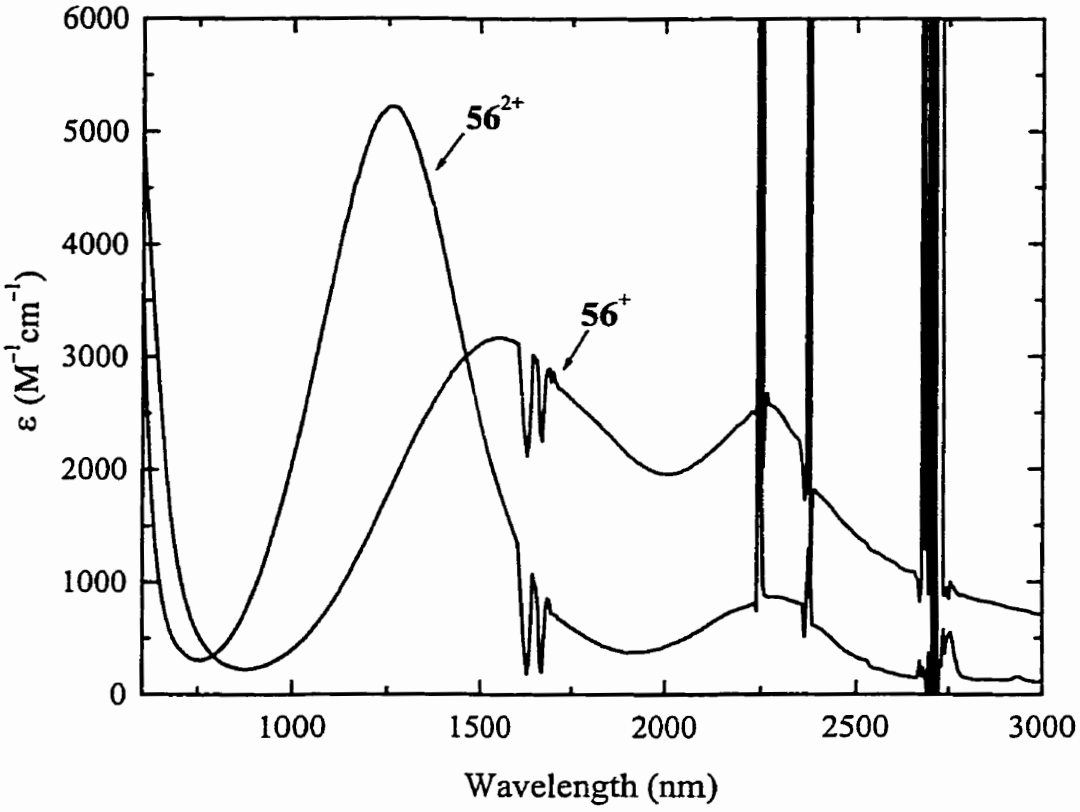

Figure 11. Near-IR spectra of $\mathbf{56}^{+}$ and $\mathbf{56}^{2+}$ in CH_2Cl_2. Sharp absorptions are due to vibrational overtones from the solvent.

The near-IR spectra of all the mono- and dications contain a higher energy band (1040 – 2240 nm) and a lower energy band (2240 – 2350 nm). The spectrum of $\mathbf{52}^{+}$ has the third broad absorption. Representative spectra for complexes $\mathbf{56}^{+}$ and $\mathbf{56}^{2+}$ are shown in Figure 11. The higher energy band is assigned to a Class II IVCT transition. The half-widths (2100 – 4400 cm^{-1}) and intensities of the higher energy band are consistent with this assignment.[31,38,136] In addition, the absorption maximum of the band depends both on solvent and on the ancillary ligands around the ruthenium (*vide infra*), also consistent with the

band being an IVCT transition. The lower energy band is narrower (430 – 950 cm^{-1}) and is of lower intensity than the higher energy band while the absorption maximum for the lower energy band is relatively insensitive to the changes in the ancillary ligands on the ruthenium center. The features of the lower energy band obtained in a limited number of solvents indicate that the absorption band is largely solvent-independent.

Although it is difficult to unequivocally assign the lower energy band, it is clear that the properties of the lower energy absorption differ dramatically from those of the higher energy band. It is most likely that the lower-energy band is due to a d – d transition in Fe^{III} which becomes accessible in the mono- and dicationic species. The energy of such a band would be expected to be solvent-independent and to appear at approximately the same energy for all the mono- and dications.[137] In addition, since the electronic transition is localized on the Fe^{III}, it would be relatively independent of the changes in the ancillary ligands on the Ru center. Multiple bands in other mixed-valence complexes have been assigned to either ligand-field splitting[138] or spin-orbit coupling in the metal centers.[139] The markedly different behavior of the two absorption bands in the series of complexes described here makes these explanations less likely. The lower energy absorption is not due to intermolecular charge transfer as the relative band intensities do not exhibit to be concentration-dependent, and the spectra are all taken at low concentrations (10^{-4} – 10^{-3} M).

Scheme 13

$$\underset{\mathbf{A}}{Fe^{III}\text{–}Ru^{II}\text{–}Fe^{III}} \xrightarrow{\nu_{op}} \underset{\mathbf{B^*}}{[Fe^{III}\text{–}Ru^{III}\text{–}Fe^{II}]^*}$$

The higher energy near-IR absorption bands for the dications $\mathbf{53}^{2+}$ – $\mathbf{57}^{2+}$ (1040 – 1595 nm) are assigned to the IVCT transition shown in Scheme 13. In these complexes both iron

centers are oxidized, and thus IVCT between the iron centers is not possible. The absorption maximum (ν_{max}) for the IVCT band shifts to higher energy as the number of carbonyl ligands on the ruthenium increases (ν_{max}: $\mathbf{53}^{2+} < \mathbf{56}^{2+} \approx \mathbf{57}^{2+} < \mathbf{55}^{2+}$). The origin of this shift in ν_{max} may be rationalized using two overlapping potential energy curves (Figure 12a). In this diagram, ν_{op} is the energy required to excite an electron from state A to state B. For complexes $\mathbf{53}^{2+}$ – $\mathbf{57}^{2+}$ ν_{op} should vary proportionally with the difference in ground-state energies (ΔE^o). Importantly, ΔE^o is expected to be larger as the electron density at the ruthenium is decreased via electron-accepting ligands.

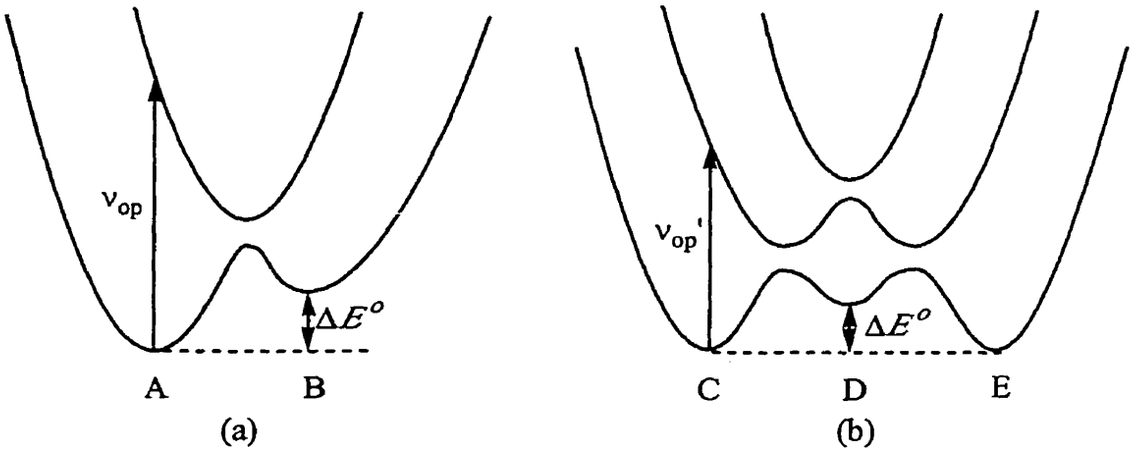

Figure 12. Potential energy diagrams for initial and final states for (a) states A and B (Scheme 13), and (b) states C, D and E (Scheme 14).

It is not possible to calculate ΔE^o exactly from the measured oxidation potentials since state B cannot be isolated; however, ΔE^o can be estimated from the electrochemical data. The transition from state A to B involves oxidation of the Ru^{II} and concomitant reduction of the Fe^{III} center; therefore, eq 13 can be derived from eqs 8 and 12. A plot of ν_{max} for the dications

vs $E_{p,a}(3) - E_{1/2}(2)$ should be linear on the base of eq 13. This data is plotted in Figure 13a, and demonstrates an approximately linear correlation between ν_{max} and $E_{p,a}(3) - E_{1/2}(2)$.

$$\nu_{max} = \chi_i + \chi_o + \Delta E' + D + (e/h\,c)[E_{p,a}(3) - E_{1/2}(2)] \qquad (13)$$

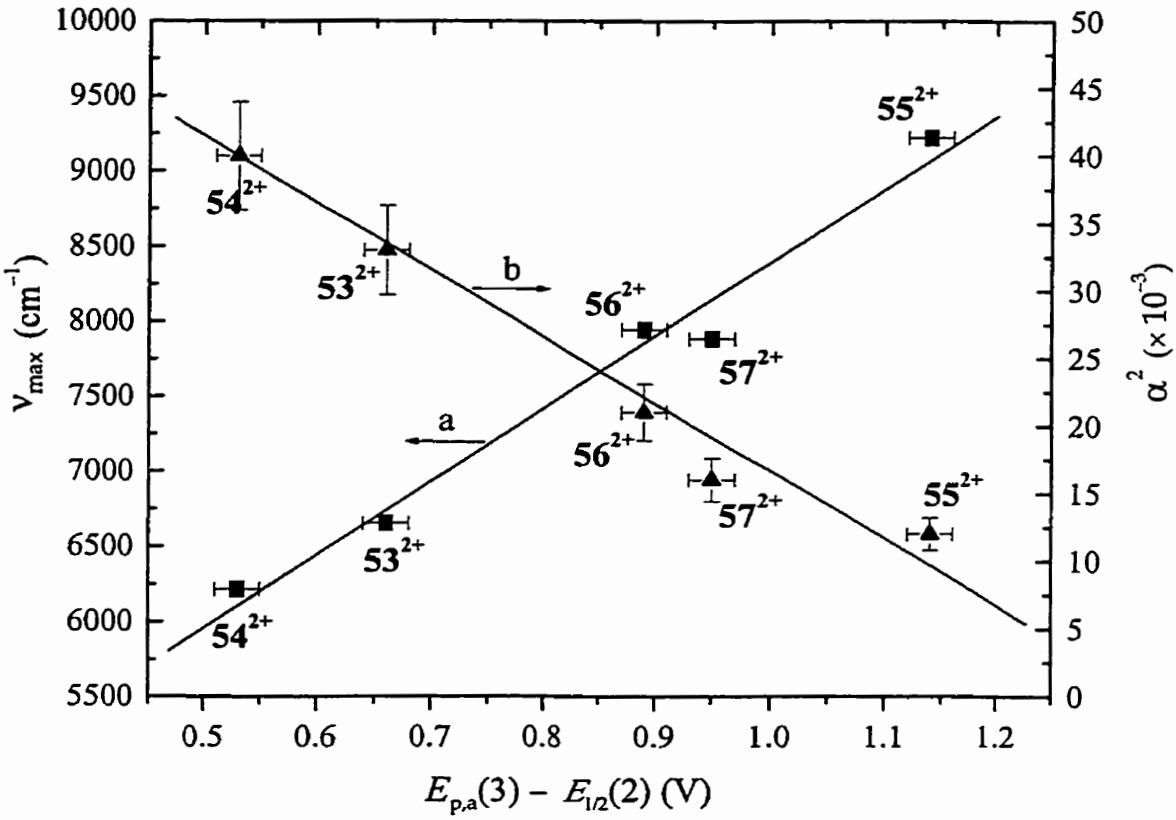

Figure 13. Plots of (a) ν_{max} vs $E_{p,a}(3) - E_{1/2}(2)$ (R = 0.989) and (b) α^2 vs $E_{p,a}(3) - E_{1/2}(2)$ (R = 0.983) for the dications $\mathbf{53}^{2+} - \mathbf{57}^{2+}$.

The model shown in Figure 12a may be extended to charge transfer in the monocations (Scheme 14). Here one must consider a three-state potential energy diagram (Figure 12b) in which ν_{op}' corresponds to the energy required to optically excite an electron

from state C to D. States C and E are isoenergetic, while state D has a higher ground-state energy.

Scheme 14

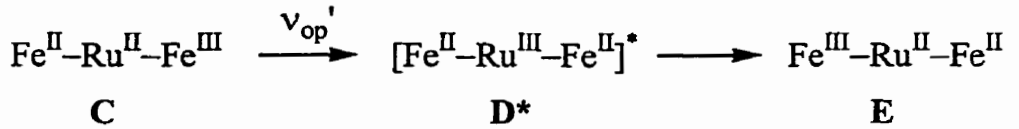

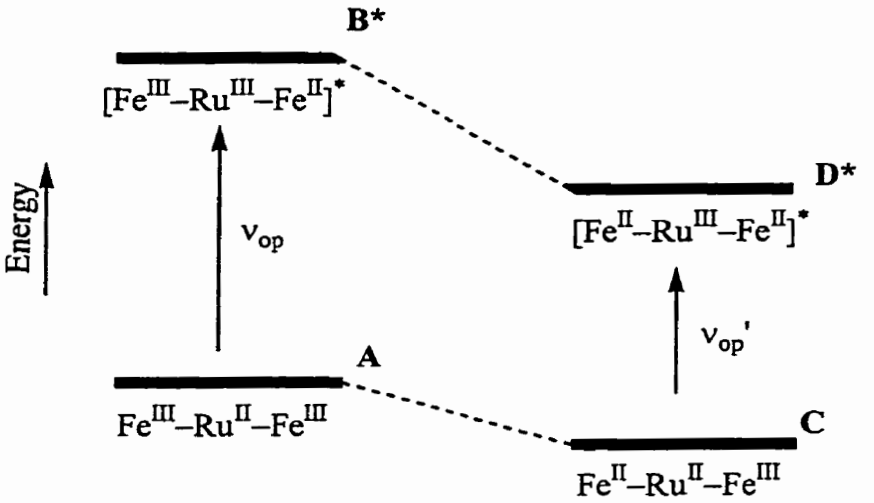

Figure 14. Relative energy diagrams for states A – D.

The absorption maximum for the IVCT band in the monocations is lower by 1000 – 2000 cm^{-1} than the corresponding transition in the spectra of the corresponding dications. The relative magnitude of the absorption maxima in the spectra of the mono- and dications may be predicted by considering the relative energies of the states involved (Figure 14). Both states C and D are lower in energy than states A and B respectively, because C and D carry less total charge than A and B. Furthermore, oxidation of a Fe^{II} center adjacent to a Ru^{III} (D to B) requires more energy than oxidation of a Fe^{II} adjacent to a Ru^{II} (C to A). Thus ν_{op}' is expected

to be lower in energy than ν_{op}. A transition involving long-range electron transfer between the two iron centers is also possible, but is expected to be of higher energy. A larger intermetallic distance often results in higher IVCT energy. The IVCT bands have been observed at 1800 nm for the monocation $[Fc–Fc]^+$, 1560 nm for $[Fc–C{\equiv}C–Fc]^+$ and 1180 nm for $\mathbf{61}^+$ in which the Fe – Fe distance is still significantly shorter than in $\mathbf{53}^+ - \mathbf{57}^+$.[43] A near-IR absorption is also observed in mixed-valence diferrocenylpolyenes;[45] however, the intermetallic distance in these complexes in solution is not exactly known due to the nonrigidity of the polyene linker. An unusual band at 820 nm is present in the visible spectrum of $\mathbf{53}^+$, and at 780 nm in $\mathbf{54}^+$. It is possible that these bands arise from the direct Fe^{II}-to-Fe^{III} charge transfer. Since states C and E are isoenergetic, state D can relax thermally to either C or E. Optical excitation to form state D followed by electron transfer to form E thus provides a pathway for charge transfer across the ruthenium bisacetylide bridge.

The dependence of the ν_{max} of an IVCT band on solvent has been used as a diagnostic test of a Class II species. According to Hush model (eqs 8 and 9), the energy (ν_{max}) of an IVCT transition may be expected to vary linearly with $(1/n^2 - 1/D_s)$ for a Class II system. The spectra of the dications are all found to be solvent-dependent. A plot of ν_{max} as a function of $(1/n^2 - 1/D_s)$ for $\mathbf{53}^{2+}$ is shown in Figure 15, along with the best-fit line obtained from linear regression (R = 0.925). This behavior is consistent with complex $\mathbf{53}^{2+}$ behaving as a Class II partially delocalized system.

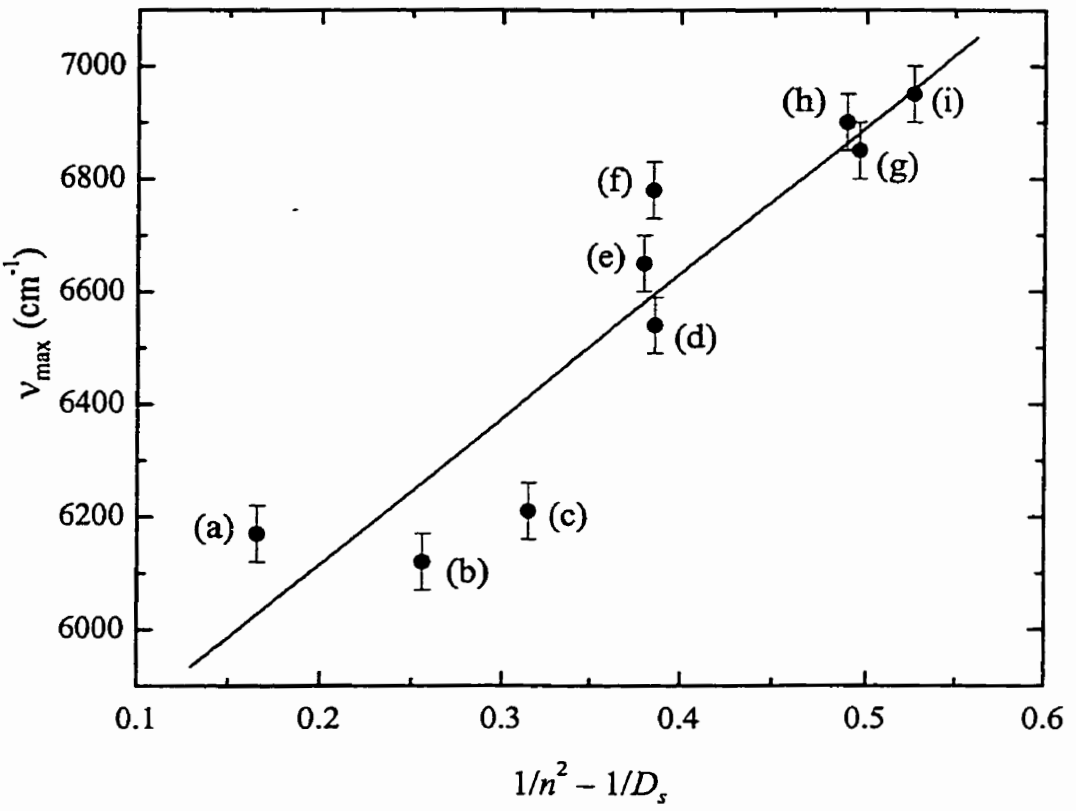

Figure 15. Plot of ν_{max} (near-IR) vs $1/n^2 - 1/D_s$ for $\mathbf{53}^{2+}$ with the best-fit line (R = 0.925). (a) trichloroethylene; (b) chlorobenzene; (c) *o*-dichlorobenzene; (d) $ClCH_2CH_2Cl$; (e) CH_2Cl_2; (f) nitrobenzene; (g) CH_3COCH_3; (h) CH_3NO_2; (i) CH_3CN.

The energy and intensities of the near-IR absorptions of mixed-valence complexes may be used to calculate a delocalization coefficient α^2 (eq 7). The values calculated for α^2 are shown in Tables 8 and 9. The value used for the Ru – Fe intermetallic distance *d* is obtained from the structural data for **52** (d = 6.20 Å) **53** (d = 6.30 Å)[53] and **55** (d = 6.15 Å). Complex **54** is assumed to have the same intermetallic distance as **53**; **56** and **57** are assumed

to have the same *d* as **55**. As shown in Figure 13b the calculated values of α^2 for the dications $\mathbf{53}^{2+} - \mathbf{57}^{2+}$ in CH_2Cl_2 are linearly correlated with $E_{p,a}(3) - E_{1/2}(2)$ (R = 0.983), indicating that the complexes with smaller difference in the ground-state energies (ΔE^o) have more charge delocalization between the iron and ruthenium centers. The monocations $\mathbf{55}^{+} - \mathbf{57}^{+}$ in CH_2Cl_2 have similar calculated values of α^2, while the values obtained for $\mathbf{53}^{+}$ and $\mathbf{54}^{+}$ are larger. The monocation $\mathbf{52}^{+}$ has two broad IVCT absorptions which have similar α^2 values, both being lower than those calculated for $\mathbf{53}^{+} - \mathbf{57}^{+}$. Comparison of the α^2 values with literature results for other molecules containing the same metal centers is instructive. The α^2 value for $[(\eta^5\text{-}C_5H_5)(PPh_3)_2RuC{\equiv}CFc]^+$ is comparable (2.8×10^{-2}),[136] while α^2 for $[(NH_3)_5RuN{\equiv}CFc]^+$ is less (2.3×10^{-3}).[140] The smaller values of α^2 for $\mathbf{52}^{+}$ and $\mathbf{52}^{2+}$ are obtained even though the extent of delocalization observed from the CV of **52** is comparable to those for **56** and **57**. Complex **52** contains a coordinated Cu^I which can interact with the delocalized system, and this may decrease the effective distance between the donor and acceptor wavefunctions.

2.4 Discussion

The cyclic voltammetric and spectroscopic data for **52** – **57** and their oxidized derivatives may be used to compare the electronic delocalization within this series of complexes. Complex **52** demonstrates the effect of varying the geometry at the ruthenium on the electronic delocalization. For **52**, $\Delta E_{1/2}$ is 0.14 V, smaller than that observed for **53** (0.22 V). There are two factors which may influence $\Delta E_{1/2}$ here; the geometry around the ruthenium center and the presence of the coordinated CuI. In complex **53** the electronic interaction between the terminal redox groups occurs via the π bonds of the cyclopentadienyl and alkynyl moieties and the d-orbitals of the ruthenium. When the acetylide ligands are trans, as in **53**,

the same d-orbitals on the metal are involved in backbonding with both acetylide ligands ($d_{xz} \rightarrow \pi^*$ and $d_{xy} \rightarrow \pi^*$). This should enhance the interaction between the ferrocenyl groups in **53** relative to **52**, where the acetylide ligands are cis, and backbonding involves three different d-orbitals, only one of which is common to both acetylide ligands ($d_{xy} \rightarrow \pi^*$, $d_{xz} \rightarrow \pi^*$ for one acetylide, $d_{xy} \rightarrow \pi^*$, $d_{yz} \rightarrow \pi^*$ for the other).

The coordinated CuI in **52** could act either to enhance the electronic interaction between the ferrocenyl groups by acting as another bridge between the two C≡C bonds, or to reduce the interaction through the ruthenium center by reducing conjugation between the ferrocenyl group and the ruthenium. It is difficult to predict which effect is more significant without comparing the electrochemical behavior of the analog of **52** in which the CuI is absent; however, this is impossible due to the instability of that analog. In the related complex $[(\eta^5\text{-}C_5H_4SiMe_3)_2Ti(C{\equiv}CSiMe_3)_2]CuOTf$[129-132] the coordinated CuOTf group lowers the energy of the C≡C absorption in the IR relative to the free ligand. This has been interpreted as the result of both backbonding from the Cu^I to a π^* orbital on the ligand and electron-donation from the π bond to the Cu^I. These results suggest that electronic interaction via the coordinated Cu^I in **52** is possible, but the magnitude of this effect relative to interaction through the Ru center is difficult to predict.

The behavior of the series of trans bisacetylide complexes **53** – **57** may be directly compared as the basic structures of these complexes are identical. Cyclic voltammetry shows that $\Delta E_{1/2}$ decreases as **54** > **53** > **56** ≈ **57** > **55**. Considering the properties of the ancillary ligands on the ruthenium found in this series of complexes, pyridine is a σ-donor, the phosphines are strong σ-donors and weak π-acceptors while carbonyl is a strong π-acceptor and a weak σ-donor. The results obtained from the CVs of this series demonstrate that the

electronic interaction between the ferrocenyl groups depends primarily on the number of carbonyl ligands. Hence, the more carbonyl ligands present around the ruthenium, the smaller $\Delta E_{1/2}$. This can be interpreted as resulting primarily from the strongly π-acidic nature of the carbonyl groups, which serve to withdraw the electron density from the ruthenium and thus decrease the electron density available for conjugation with the acetylide bonds. Two electron-donating dmpe ligands on the ruthenium in **54** result in a 0.09 V increase in $\Delta E_{1/2}$ compared with **53**, while one carbonyl group decreases $\Delta E_{1/2}$ by almost the same amount. Varying the number and nature of the non-carbonyl ligands has a somewhat smaller effect on $\Delta E_{1/2}$ compared to that exerted by the carbonyl group. In addition to the trend in $\Delta E_{1/2}$, the potential measured for the $Ru^{II/III}$ oxidation wave in the CV increases as the number of carbonyl ligands on the ruthenium is increased. As electron density is lost from the metal to the carbonyl ligands, the ruthenium becomes increasingly difficult to oxidize.

The trends in electron delocalization observed by CV are consistent with those observed by spectroscopic methods. In the visible region, the magnitude of the redshift observed in the LMCT band for $\mathbf{53}^+ - \mathbf{57}^+$ relative to $\mathbf{61}^+$ increases as the number of donor ligands on the ruthenium is increased. Similarly, in the IR region both the C≡C and C≡O absorptions correlate to the electrochemical results. Based on the CV data, **53** or **54** has a higher electron density at the ruthenium relative to the monocarbonyl complexes **56** and **57** and dicarbonyl **55**. This results in a lower $\nu_{C\equiv C}$ for **53** or **54** than for **56** or **57** since more backbonding is possible in **53** or **54**. Complex **56** also has a donor ligand trans to the carbonyl group which allows for more backbonding with the lone carbonyl than in **55**.

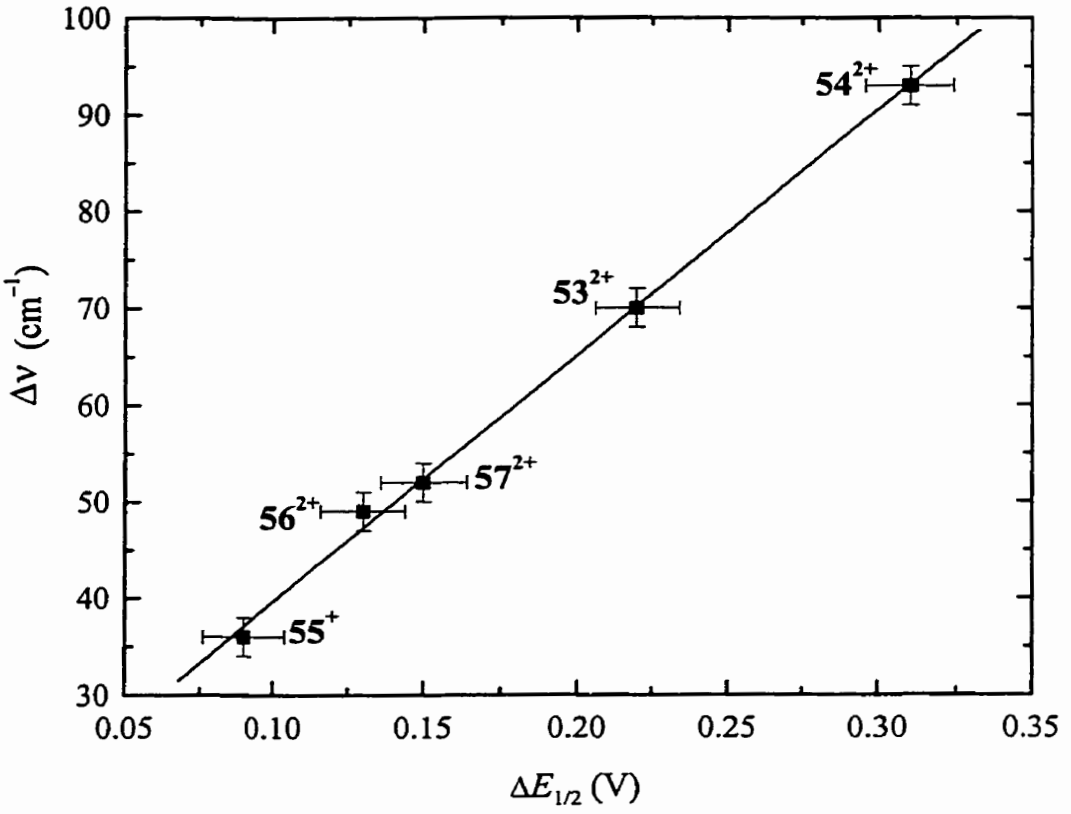

Figure 16. Plot of $\Delta E_{1/2} = E_{1/2}(2) - E_{1/2}(1)$ vs the difference in $\nu_{C\equiv C}$ between the neutral and dicationic complexes ($\Delta\nu_{C\equiv C}$) with a best-fit line to the data (R = 0.999).

Interestingly, the wavenumber difference between the acetylide absorptions of the neutral and dicationic species correlates with the degree of electronic delocalization observed in the CV. The difference in the sequential ferrocenyl-oxidation potentials $\Delta E_{1/2}$ is correlated to the difference in the C≡C absorptions between the neutral and dicationic complexes ($\Delta\nu_{C\equiv C}$) (Figure 16). Complex **54** has the largest $\Delta E_{1/2}$, and the difference in the absorption is the largest (93 cm^{-1}) between **54** and $\mathbf{54}^{2+}$; while **55** has the smallest $\Delta E_{1/2}$, and the difference is

smallest (36 cm^{-1}). This is a result of how much of the electron density at the ruthenium is available for backbonding with the acetylide ligands. Ancillary ligands such as carbonyls, which withdraw electron density, allow less participation of the ruthenium d-electrons in electron transfer along the acetylide backbone.

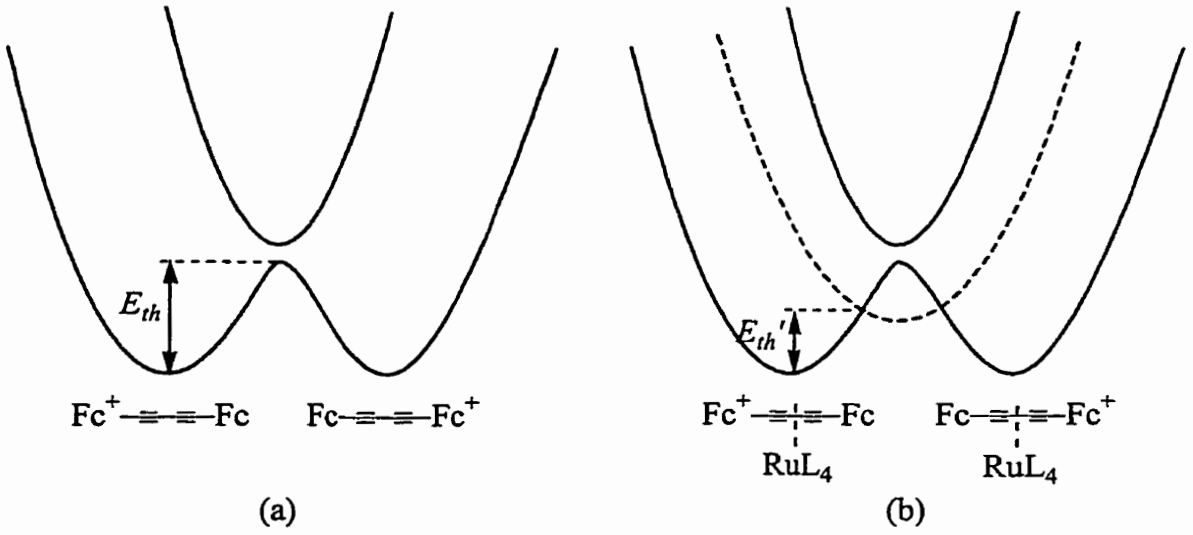

Figure 17. Potential diagrams for electron delocalization in (a) **61**$^+$ and in a hypothetical molecule in which a RuL_4 is inserted into the central C–C bond in **61**$^+$.

The charge delocalization in these complexes is best explained by the potential-energy diagram shown in Figure 12b. The nature of the ancillary ligands on the ruthenium center affects the difference in ground-state energy (ΔE^o). Donor ligands decrease ΔE^o, thus facilitating charge transfer across the ruthenium bisacetylide bridge, while acceptor ligands increase ΔE^o. Complexes **53** – **57** have similar structures, and comparison of the $\Delta E_{1/2}$ within the series indicates a significant contribution from charge delocalization to the magnitude of $\Delta E_{1/2}$. Changes in the ligands on the Ru (II) result in increases in $\Delta E_{1/2}$ (0.13 V) from 0.09 V for **55** to 0.22 V for **53**, and (0.22 V) to 0.31 V for **54**. It is reasonable to conclude that this

increase in $\Delta E_{1/2}$ is mainly due to the contribution from charge delocalization. For **53** and **54** this contribution exceeds the total stabilization energy in complex **61**, which has $\Delta E_{1/2} = 0.10$ V, thus there is less charge delocalization between the two ferrocenyl groups in complex $\mathbf{61}^+$ than in $\mathbf{53}^+$ and $\mathbf{54}^+$. This result may be understood by considering the potential-energy diagram for $\mathbf{61}^+$ (Figure 17a). Charge transfer between the two states occurs either in the ground states by overcoming the activation barrier (E_{th}), or in the excited state via IVCT. Figure 17b shows the potential-energy diagram for a hypothetical molecule consisting of $\mathbf{61}^+$ with a ruthenium center between the two ferrocenyl groups. Here the ruthenium facilitates electron delocalization by reducing the energy barrier in the ground state (E_{th}'). The potential-energy diagrams for the mono- and dications of complexes **52** – **57** (Figure 12a and b) are slightly different since the distance between the two iron centers is greater than that shown in Figure 17b; however, the same principle is expected to hold. It is clearly demonstrated that the extent to which the energy barrier is lowered is influenced by the ancillary ligands on the ruthenium; therefore, the extent of delocalization is affected by these ligands.

2.5 Conclusions

A series of ruthenium(II) bisferrocenylacetylide complexes are synthesized by coupling ruthenium halide complexes with FcC≡CSn(*n*-Bu)$_3$ in the presence of copper (I) halide. The amount of copper (I) halide used significantly affects the product formed. When a stoichiometric amount of CuI is used [*cis*-Ru(dppm)$_2$(C≡CFc)$_2$]CuI is obtained, while *trans*-Ru(dppm)$_2$(C≡CFc)$_2$ is obtained with catalytic CuI. Removal of coordinated CuI from [*cis*-Ru(dppm)$_2$(C≡CFc)$_2$]CuI yields *trans*-Ru(dppm)$_2$(C≡CFc)$_2$, while reaction of *trans*-

$Ru(dppm)_2(C{\equiv}CFc)_2$ with a stoichiometric amount of CuI yields [*cis*-$Ru(dppm)_2(C{\equiv}CFc)_2$]CuI.

The stability of the complexes in different oxidation states allows for studies of charge transfer between different metal centers in these complexes by electrochemical and spectroscopic characterization. Charge delocalization between the iron and ruthenium centers in the oxidized species is observed, and the extent of delocalization is evaluated. The ruthenium bisacetylide bridges facilitate electronic interactions between the terminal ferrocenyl groups. The interaction is enhanced when the ancillary ligands on the ruthenium center are electron donors and lessened when the ligands are acceptors.

Chapter 3 Models for Conjugated Metal Acetylide Polymers: Ruthenium Oligothienylacetylide Complexes

3.1 Introduction

The work described in Chapter 2 shows that the bridge in ruthenium bis(ferrocenylacetylide) complexes allows for delocalization of charge between the two ferrocenyl groups, and that the delocalization varies with the nature of the ancillary ligands surrounding the ruthenium. These results suggest that linking conjugated organic groups with ruthenium bisacetylide bridges could result in extended conjugation involving both the metal center and the organic bridges. Lewis and coworkers have synthesized ruthenium bisacetylide polymers where the metal centers are linked by phenyl bridges;[71,80] however, no electronic properties have been reported to date for these materials. Although these phenyl group-bridged polymers are readily accessible synthetically it may be necessary to link the metal centers in these polymers with organic fragments which are more electron-rich and have longer conjugation lengths in order to enhance delocalization of charge.

It has been demonstrated that block copolymers containing short oligothiophenes (> 4 thiophene units) are conductive.[10,141] This suggests that ruthenium acetylide polymers containing oligothienyl bridges may be good candidates for conducting materials. Toward this end, one approach is the preparation of electropolymerizable monomers consisting of oligothiophenes bridged by ruthenium bisacetylide groups (Figure 8). In this Chapter the preparation and characterization of the series of ruthenium mono(oligothienylacetylide) complexes **62a – c** and bis(oligothienylacetylide) complexes **63a – c** are described. The

interaction between the metal and organic fragments is probed. Electropolymerization of several of these complexes are also carried out.

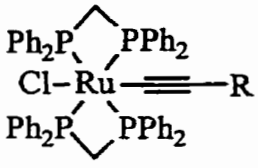

62a – c

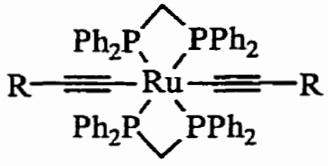

63a – c

R =

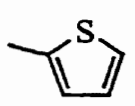

a

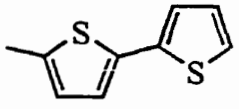

b

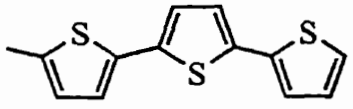

c

3.2 Experimental

General. Procedures were as described in Chapter 2 except as noted here. Diethyl ether and THF were dried by refluxing over sodium/benzophenone. Diisopropylamine was purified by distillation from KOH and was stored over molecular sieves (4 Å). Trans-$Pd(PPh_3)_2Cl_2$,[142], $Ni(dppp)Cl_2$,[143] 1-(trimethylsilyl)-2-(2-thienyl)acetylene (**64a**),[144] (2-thienyl)acetylene (**65a**),[144] 2,2'-bithiophene,[144] 5-bromo-2,2'-bithiophene,[145] 2,2':5',2"-terthiophene[146] and 5-iodo-2,2':5',2"-terthiophene[146] were all prepared using literature procedures. 1-(Trimethylsilyl)-2-(5-(2,2'-bithienyl))acetylene (**64b**) and (5-(2,2'-bithienyl))acetylene (**65b**) were prepared by modification of the procedures for the preparation of **64a** and **65a** respectively.[144] 1-(Tributylstannyl)-2-(2-thienyl)acetylene (**67a**) and 1-(tributylstannyl)-2-(5-(2,2'-bithienyl))acetylene (**67b**) were prepared using the procedure for 1-(tributylstannyl)-2-(5-(2,2':5',2"-terthienyl))acetylene (**67c**), and used without further purification. The concentration of the complexes for electrochemical measurements was in the range $1.6 \times 10^{-3} - 2.2 \times 10^{-3}$ M unless otherwise noted. The visible and near-IR spectra of

62a$^+$ – c$^+$ and **63a$^+$ – c$^+$** in dry CH_2Cl_2 solutions were collected on a Varian Cary 5 spectrometer, in which the sample cell was held at –17 °C under a nitrogen atmosphere.

1-(Trimethylsilyl)-2-(5-(2,2':5',2"-terthienyl))acetylene (64c). A suspension of 5-iodo-2,2':5',2"-terthiophene (0.64 g, 1.7 mmol), diisopropylamine (0.33 g, 3.3 mmol), trans-$Pd(PPh_3)_2Cl_2$ (0.14 g, 0.20 mmol) and CuI (0.022 g, 0.12 mmol) in dry THF (60 mL) was degassed for 2 min with N_2. Trimethylsilylacetylene (0.33 g, 3.4 mmol) was added to the suspension via syringe. After the solution was stirred overnight at room temperature the solution turned dark green. The reaction was quenched by adding distilled water (20 mL) to the solution. The organic layer was collected, and the aqueous layer was extracted with CH_2Cl_2 (2 × 20 mL). The organic extracts were combined and washed with brine (30 mL) and distilled water, and then dried over anhydrous $MgSO_4$. The solvent was removed to obtain a brown solid, which was purified by flash chromatography (silica gel), using hexanes as eluant. Yield: 0.52 g (88%). ^{1}H NMR (400 MHz, $CDCl_3$): δ 7.21 (dd, J = 5.1, 1.0 Hz, 1H), 7.16 (dd, J = 3.6, 1.0 Hz, 1H), 7.12 (d, J = 3.8 Hz, 1H), 7.05 (s, 2H), 7.00 (dd, J = 5.1, 3.6 Hz, 1H), 6.97 (d, J = 3.8 Hz, 1H), 0.30 (s, 9H). ^{13}C{^{1}H} NMR (75.429 MHz, $CDCl_3$): δ 138.48, 136.85, 136.78, 135.22, 133.48, 127.86, 124.78, 124.66, 124.29, 123.84, 123.08, 121.72, 100.18, 97.39, –0.17. Anal. Calcd for $C_{17}H_{16}S_3Si$: C 59.25, H 4.68. Found: C 59.18, H 4.70.

(5-(2,2':5',2"-Terthienyl))acetylene (65c). To a solution of **64c** (0.44 g, 1.3 mmol) in a mixture of $CHCl_3$ and MeOH (60 mL, 1:3 v/v), was added anhydrous K_2CO_3 (0.36 g, 2.6 mmol). The suspension was stirred at room temperature for 2 h, after which time the solvent was removed, and the solid was extracted with $CHCl_3$ (20 mL). The $CHCl_3$ solution was then washed with distilled water (2 × 30 mL), and dried over anhydrous $MgSO_4$. The product was obtained as a yellow solid by removing the solvent and then purified by flash chromatography

(silica gel) using hexanes as eluant. Yield: 0.27 g (78%). ^{1}H NMR (400 MHz, $CDCl_3$): δ 7.22 (dd, J = 5.1, 1.1 Hz, 1H), 7.15 – 7.17 (m, 2H), 7.05-7.07 (m, 2H), 6.99 – 7.02 (m, 2H), 3.40 (s, 1H). $^{13}C\{^1H\}$ NMR (75.429 MHz, $CDCl_3$): δ 138.85, 137.06, 136.79, 135.09, 133.98, 127.93, 124.99, 124.79, 124.35, 123.96, 123.09, 120.56, 82.56, 82.38. Anal. Calcd for $C_{14}H_8S_3$: C 61.73, H 2.96. Found: C 62.04, H 2.96.

Diisopropylaminotributylstannane. This compound was prepared by modification of a literature procedure.[147] *n*-BuLi (1.6 M in hexanes; 31.7 mL, 50.7 mmol) was diluted with dry diethyl ether (30 mL), and cooled to –78 °C. Diisopropylamine (5.19 g, 51.3 mmol) was cooled to –78 °C, and was added dropwise via cannula while the *n*-BuLi solution was being stirred. Upon completion of the addition, the mixture was allowed to warm to room temperature. A solution of tributyltin chloride (10.3 mL, 38.0 mmol) in dry diethyl ether (15 mL) was added to the stirred reaction mixture, causing an immediate color change to milky white. After being heated at reflux for 4 h, the solution was stirred at room temperature for 12 h, after which time the mixture became a pale yellow cloudy suspension. The lithium chloride was removed by suction filtration through Celite under N_2. Removal of the solvent from the filtrate afforded an orange oil, which was distilled *in vacuo* to obtain a moisture-sensitive colorless oil (bp = 152 °C at 0.15 mmHg). Yield: 9.01 g (61%). ^{1}H NMR (200.132 MHz, $CDCl_3$): δ 2.83 (septet, J = 6.3 Hz, 2H), 1.51 – 1.64 (m, 6H), 1.16 – 1.39 (m, 12H), 0.97 (d, J = 6.3 Hz, 12 H), 0.86 (t, J = 7.3 Hz, 9H). Anal. Calcd for $C_{18}H_{41}NSn$: C 55.40, H 10.59, N 3.59. Found: C 55.38, H 10.68, N 3.90.

1-(Tributylstannyl)-2-(5-(2,2':5',2''-terthienyl))acetylene (67c). This compound was prepared by modification of a published procedure.[148] Diisopropylaminotributylstannane (0.72 g, 1.8 mmol) was added to a flask charged with **65c** (0.50g, 1.8 mmol). Dry THF (20

mL) was added to the mixture, and the solution was stirred overnight in the absence of light at room temperature. The THF was removed, and the residual oil was held *in vacuo* at room temperature overnight to obtain a brown oil. Yield: 1.02 g (99%). ^{1}H NMR (400 MHz, $CDCl_3$): δ 7.20 (dd, J = 5.1, 1.0 Hz, 1H), 7.15 (dd, J = 3.6, 1.0 Hz, 1H), 7.06 (d, J = 3.8 Hz, 1H), 7.04 (s, 2H), 7.00 (dd, J = 5.1, 3.6 Hz, 1H), 6.97 (d, J = 3.8 Hz, 1H), 1.57 – 1.64 (m, 6H), 1.32 – 1.41 (m, 6H), 1.07 (t, J = 8.1 Hz, 6H), 0.93 (t, J = 7.3 Hz, 9H). Anal. Calcd for $C_{26}H_{34}S_3Sn$: C 55.62, H 6.10. Found: C 55.84, H 6.29.

***trans*-{Ru=C=CHR(dppm)$_2$(Cl)}[PF$_6$] (R = 2-thienyl) (66a).** To a solution of **59** (0.60 g, 0.64 mmol) and $NaPF_6$ (0.21 g, 1.3 mmol) in CH_2Cl_2 (75 mL) was added **65a** (0.15 g, 1.4 mmol). After being stirred at room temperature for 18 h, the red-brown solution was filtered through a filter-paper-tipped cannula. The solvent was removed *in vacuo*, and the residue was rinsed with diethyl ether to obtain a rust-colored solid. The solid was dried *in vacuo* at 90 °C for 6 days. Yield: 0.68 g (92%). ^{1}H NMR (400 MHz, $CDCl_3$): δ 7.15 – 7.45 (m, 40H), 6.87 (dd, J = 5.2, 0.9 Hz, 1H), 6.51 (dd, J = 5.2, 3.6 Hz, 1H), 5.30–5.40 (m, 2H), 5.01 – 5.10 (m, 3H), 3.22 – 3.25 (m, 1H). ^{31}P{^{1}H} NMR (81.015 MHz, $CDCl_3$): δ –18.1 (s). Anal. Calcd for $C_{56}H_{48}ClF_6P_5RuS$: C 58.06, H 4.18. Found: C 57.70, H 4.06.

***trans*-Ru(dppm)$_2$(Cl)(C≡CR) (R = 2-thienyl) (62a).** To a solution of **66a** (0.62 g, 0.54 mmol) in CH_2Cl_2 (40 mL) was added 1,8-diazabicyclo[5.4.0]undec-7-ene (DBU) (80 μL, 0.54 mmol) via syringe. The red-brown solution changed color quickly to yellow. After being stirred at room temperature for 2 h, the reaction mixture was filtered through a filter-paper-tipped cannula, and the solvent was removed *in vacuo*. The resulting dark yellow solid was taken up in a minimum of THF and transferred via cannula to a Schlenk filter charged with neutral alumina (Brockman, Activity I). The product was eluted with diethyl ether.

Removal of the solvent at reduced pressure, followed by rinsing with hexanes, yielded a yellow solid, which was recrystallized from layered chloroform/hexanes. The crystals were crushed and dried *in vacuo* at 90 °C for 6 days. Yield: 0.36 g (66%). ^{1}H NMR (400 MHz, $CDCl_3$): δ 7.38 – 7.50 (m, 16H), 7.20–7.30 (m, 8H), 7.15 (t, J = 7.6 Hz, 8H), 7.09 (t, J = 7.6 Hz, 8H), 6.57 – 6.60 (m, 2H), 5.68 (dd, J = 2.6, 1.9 Hz, 1H), 4.88 (quintet, J = 4.2 Hz, 4H). ^{31}P{^{1}H} NMR (81.015 MHz, $CDCl_3$): δ –8.7 (s). Anal. Calcd. for $C_{56}H_{47}ClP_4RuS$: C 66.43, H 4.68. Found: C 66.33, H 4.61.

***trans*-Ru(dppm)$_2$(Cl)(C≡CR) (R = 5-(2,2'-bithienyl)) (62b).** To a solution of **59** (0.31 g, 0.33 mmol) and $NaPF_6$ (0.16 g, 0.95 mmol) in CH_2Cl_2 (30 mL) was added **65b** (0.17 g, 0.89 mmol). The solution was stirred at room temperature for 7 h, turning dark-brown. The solution was then filtered through a filter-paper-tipped cannula, and a brown solid was obtained by removing the solvent. The solid was dissolved in CH_2Cl_2, and filtered through a short Al_2O_3 column (Basic, Brockman Activity I) to give an orange solution. The volume of the solution was reduced to approximately 1 mL, and hexanes (40 mL) were added to the solution to induce the precipitation of an orange-yellow solid. The solid was dried overnight *in vacuo* at room temperature. Yield: 0.16 g (44%). ^{1}H NMR (400 MHz, CD_2Cl_2): δ 7.50 – 7.56 (m, 8H), 7.41 – 7.47 (m, 8H), 7.34 (t, J = 7.4 Hz, 4H), 7.30 (t, J = 7.4 Hz, 4H), 7.22 (t, J = 7.6 Hz, 8H), 7.16 (t, J = 7.6 Hz, 8H), 7.10 – 7.12 (m, 1H), 6.96 – 6.98 (m, 2H), 6.70 (d, J = 3.4 Hz, 1H), 5.54 (d, J = 3.4 Hz, 1H), 4.86 – 4.99 (m, 4H). ^{31}P{^{1}H} NMR (81.015 MHz, $CDCl_3$): δ –8.9 (s). Anal. Calcd for $C_{60}H_{49}ClP_4RuS_2$: C 65.84, H 4.51. Found: C 65.92, H 4.52.

***trans*-Ru(dppm)$_2$(Cl)(C≡CR) (R = 5-(2,2':5',2''-terthienyl)) (62c).** This complex was prepared as described for **62b**. Yield: 53%. ^{1}H NMR (400 MHz, CD_2Cl_2): δ 7.50 – 7.56 (m, 8H), 7.41 – 7.48 (m, 8H), 7.12 – 7.38 (m, 26H), 7.03 – 7.06 (m, 2H), 6.87 (broad, 1H),

6.72 (d, J = 3.7 Hz, 1H), 5.54 (broad, 1H), 4.86 – 4.98 (m, 4H). $^{31}P\{^{1}H\}$ NMR (81.015 MHz, $CDCl_3$): δ –8.9 (s). Anal. Calcd. for $C_{64}H_{51}ClP_4RuS_3$: C 65.33, H 4.37. Found: C 65.49, H 4.42.

***trans*-Ru(dppm)$_2$(C≡CR)$_2$ (R = 2-thienyl) (63a).** To a deaerated solution of **59** (0.43 g, 0.46 mmol) and CuI (7 mg, 0.04 mmol) in chlorobenzene (25 mL) was added **67a** (0.73 g, 1.8 mmol). The solution was heated at reflux overnight, and then cooled to room temperature. Chlorobenzene was removed, and the residual solid was dissolved in CH_2Cl_2. The CH_2Cl_2 solution was filtered through Celite to remove CuI. The filtrate was concentrated to approximately 10 mL, and hexanes were added. The solution was then cooled to –4 °C overnight, resulting in the precipitation of **63a**. Yield: 0.30 g (60%). ^{1}H NMR (400 MHz, CD_2Cl_2): δ 7.47 – 7.55 (m, 16H), 7.28 (t, J = 7.4 Hz, 8H), 7.15 (t, J = 7.6 Hz, 16H), 6.63 – 6.66 (m, 4H), 5.87 (t, J = 2.3 Hz, 2H), 4.85 (quintet, J = 4.2 Hz, 4H). $^{31}P\{^{1}H\}$ NMR (81.015 MHz, CD_2Cl_2): δ –4.4 (s). Anal. Calcd for $C_{62}H_{50}P_3RuS_2$: C 68.69, H 4.65. Found: C 68.43, H 4.53.

***trans*-Ru(dppm)$_2$(C≡CR)$_2$ (R = 5-(2,2'-bithienyl)) (63b).** This complex was prepared as described for **63a**. Yield: 80%. ^{1}H NMR (400 MHz, $CDCl_3$): δ 7.42 – 7.48 (m, 16H), 7.26 (t, J = 7.4 Hz, 8H), 7.15 (t, J = 7.6 Hz, 16H), 7.07 (dd, J = 5.0, 1.2 Hz, 2H), 6.93 – 6.99 (m, 4H), 6.74 (d, J = 3.7 Hz, 2H), 5.69 (d, J = 3.7 Hz, 2H), 4.81 (quintet, J = 4.1 Hz, 4H). $^{31}P\{^{1}H\}$ NMR (81.015 MHz, $CDCl_3$): δ –6.3 (s). Anal. Calcd for $C_{70}H_{54}P_4RuS_4$: C 67.35, H 4.36. Found: C 67.01, H 4.47.

***trans*-Ru(dppm)$_2$(C≡CR)$_2$ (R = 5-(2,2':5'2"-terthienyl)) (63c).** The complex was prepared as described for **63a**. Yield: 84%. ^{1}H NMR (400 MHz, $CDCl_3$): δ 7.41 – 7.47 (m, 16H), 7.27 (t, J = 7.4 Hz, 8H), 7.11 – 7.19 (m, 20H), 7.02 (d, J = 3.6 Hz, 2H), 7.00 (dd, J =

5.1, 3.6, 2H), 6.87 (d, J = 3.7 Hz, 2H), 6.75 (d, J = 3.7 Hz, 2H), 5.69 (d, J = 3.7 Hz, 2H), 4.82 (quintet, J = 4.0 Hz, 4H). $^{31}P\{^{1}H\}$ NMR (81.015 MHz, $CDCl_3$): δ –6.3 (s). Anal. Calcd for $C_{78}H_{58}P_4RuS_6$: C 66.32, H 4.14. Found: C 65.98, H 4.04.

Crystallographic Study. Data collection and structure determination were performed by the late Dr. Steven Rettig in this department. An orange irregular crystal of dimensions 0.40 × 0.35 × 0.20 mm was used. Data were obtained on a Rigaku/ADSC CCD area detector with graphite monochromated Mo-Kα radiation (λ = 0.71069 Å). The data were collected at a temperature of –93° C. A total of 15312 independent reflections were measured ($2\theta \leq 61°$), of which 8814 had $I > 3\sigma(I)$ and were considered to be observed. The data were corrected for Lorentz and polarization factors. Crystal data for **63c**: $C_{78}H_{58}P_4RuS_6$, M_r = 1412.64, triclinic, space group $P\bar{1}$ *(#2)*, a = 13.1663(9) Å, b = 15.5443(8) Å, c = 17.757(2) Å, α = 70.834(3)°, β = 83.6388(10)°, γ = 75.9874(6)°, V = 3328.7(4) Å^3, Z = 2, D *(calc)* = 1.409 g cm^{-3}, μ (Mo Kα) = 5.65 cm^{-1}, $F(000)$ = 1452.

The structure was solved by direct methods and expanded using Fourier techniques. Both terminal thiophene moieties are disordered with respect to a 180° rotation about the bond to the adjacent ring. For the ring containing S(3) and the minor component S(3a) the disorder was modeled by split-atom refinement with bond length constraints. A similar treatment of the more nearly ordered ring containing S(6) was not successful. As a result of the disorder, both resolved and unresolved, the geometry of the terminal thiophene rings is subject to errors larger than expected from the least-squares standard deviations. All other non-hydrogen atoms were refined anisotropically. Hydrogen atoms were fixed in idealized positions with C–H = 0.98 Å and thermal parameters 1.2 times those of the parent atoms. The final cycle of full-matrix least-squares refinement was based on the observed data and 809 variable

parameters and converged with $R_1 = 0.037$ and $wR_2 = 0.079$. The maximum and minimum peaks on the final difference Fourier map were corresponded to 1.92 and –1.28 e $Å^{-3}$ respectively. All calculations were performed using the teXsan crystallographic software package of Molecular Structure Corporation.

3.3 Results and Interpretation

3.3.1 Syntheses and Structure

Complexes **62a** – **c** are synthesized by coupling *cis*-Ru(dppm)$_2$Cl$_2$ (**59**) with oligothienylacetylenes **65a** – **c** in the presence of excess $NaPF_6$, yielding ruthenium vinylidene complexes **66a** – **c** (Scheme 15). Complexes **66a** – **c** are converted to **62a** – **c** either by passing through a basic Al_2O_3 column or by reaction with 1,8-diazabicyclo[5.4.0.]undec-7-ene (DBU).

Scheme 15

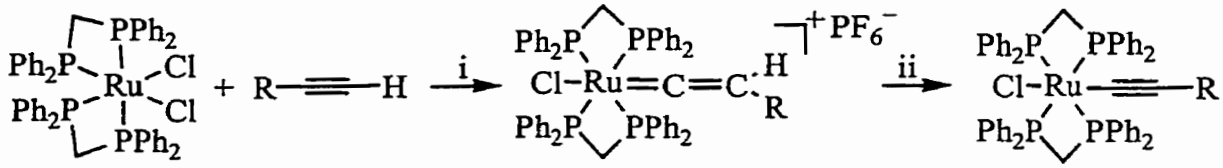

59 **65a – c** **66a – c** **62a – c**

i: $NaPF_6$, CH_2Cl_2; ii: DBU/neutral Al_2O_3 or basic Al_2O_3

Scheme 16

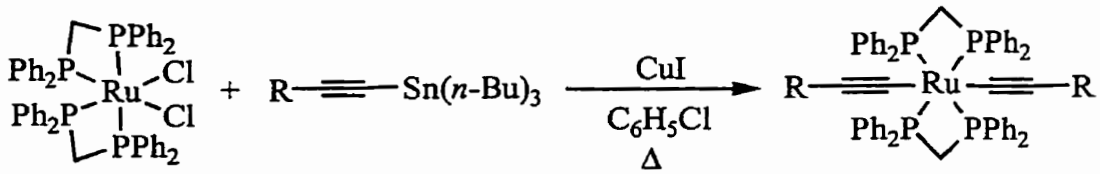

59 **67a – c** **63a – c**

Bisacetylide complexes **63a** – **c** are prepared via the coupling of **59** with the corresponding 1-(tributylstannyl)-2-(oligothienyl)acetylenes **67a** – **c** in the presence of catalytic CuI (Scheme 16). The reactions are carried out in the absence of light in chlorobenzene heated at reflux. Complexes **62a** – **c** and **63a** – **c** are fully characterized using ^{1}H and ^{31}P NMR, IR and UV–vis spectroscopies, and the elemental analyses are all in the expected range. In solution, all the complexes decompose slowly when exposed to ambient light.

The ^{1}H NMR spectrum of **62c** shows broadened peaks assigned to the protons close to the ruthenium, and a single broadened peak is observed in the ^{31}P NMR spectrum. The broadened peaks sharpen when diisopropylamine is added to the NMR solution, and no new resonances are observed in the ^{31}P NMR spectrum, consistent with the broadening being a result of partial oxidation to the paramagnetic Ru^{III} species, and *in situ* reduction with diisopropylamine. It is possible that **62c** is oxidized slowly in solution when the solution is exposed to air, or that a trace amount of the Ru^{III} species is formed on the basic alumina in the last step of the synthesis. This is the only compound in the series for which peak broadening is consistently observed in the NMR spectra.

Complex **63c** is crystallized from layered CH_2Cl_2/hexanes at 4°C to obtain orange irregular crystals whose structure is determined by single-crystal X-ray diffraction (Figure 18). Selected bond lengths and angles are listed in Table 10. The ruthenium center is in a distorted octahedral environment with the two terthienylacetylide ligands in a trans orientation around the Ru. The dihedral angles between the six thiophene rings in the structure are of interest since the extent of conjugation depends on the coplanarity of the rings. The thiophene rings are labeled 1 – 6 in Figure 18. The dihedral angle between the two innermost thiophene rings

(1 and 4) is 47.2°. The dihedral angles between rings 1 – 2 and 4 – 5 are small, 9.3° and 2.6° respectively, indicating that these rings are held nearly coplanar in the solid-state molecular structure. Both terminal thiophene rings (3 and 6) are disordered with respect to 180° rotation about the bond to the adjacent ring and have dihedral angles with the adjacent rings of 17.8° (2 – 3) and 27.6° (5 – 6).

Table 10. Selected Bond Lengths (Å) and Angles (deg) for **63c**

Ru(1) – P(1)	2.3306(8)	Ru(1) – C(1)	2.059(3)
Ru(1) – P(2)	2.3298(7)	Ru(1) – C(15)	2.067(3)
Ru(1) – P(3)	2.3243(8)	C(1) – C(2)	1.195(4)
Ru(1) – P(4)	2.3340(7)	C(15) – C(16)	1.200(4)
P(1) – Ru(1) – P(2)	72.65(3)	P(3) – Ru(1) – C(1)	92.09(8)
P(1) – Ru(1) – P(3)	178.63(3)	P(3) – Ru(1) – C(15)	90.92(9)
P(1) – Ru(1) – P(4)	108.70(3)	P(4) – Ru(1) – C(1)	92.20(7)
P(2) – Ru(1) – P(3)	106.12(3)	P(4) – Ru(1) – C(15)	88.38(7)
P(2) – Ru(1) – P(4)	178.42(3)	C(1) – Ru(1) – C(15)	176.97(12)
P(3) – Ru(1) – P(4)	72.52(3)	Ru(1) – C(1) – C(2)	176.4(3)
P(1) – Ru(1) – C(1)	87.26(8)	Ru(1) – C(15) – C(16)	175.5(3)
P(1) – Ru(1) – C(15)	89.74(9)	C(1) – C(2) – C(3)	177.2(3)
P(2) – Ru(1) – C(1)	87.03(7)	C(15) – C(16) – C(17)	174.8(4)
P(2) – Ru(1) – C(15)	92.46(7)		

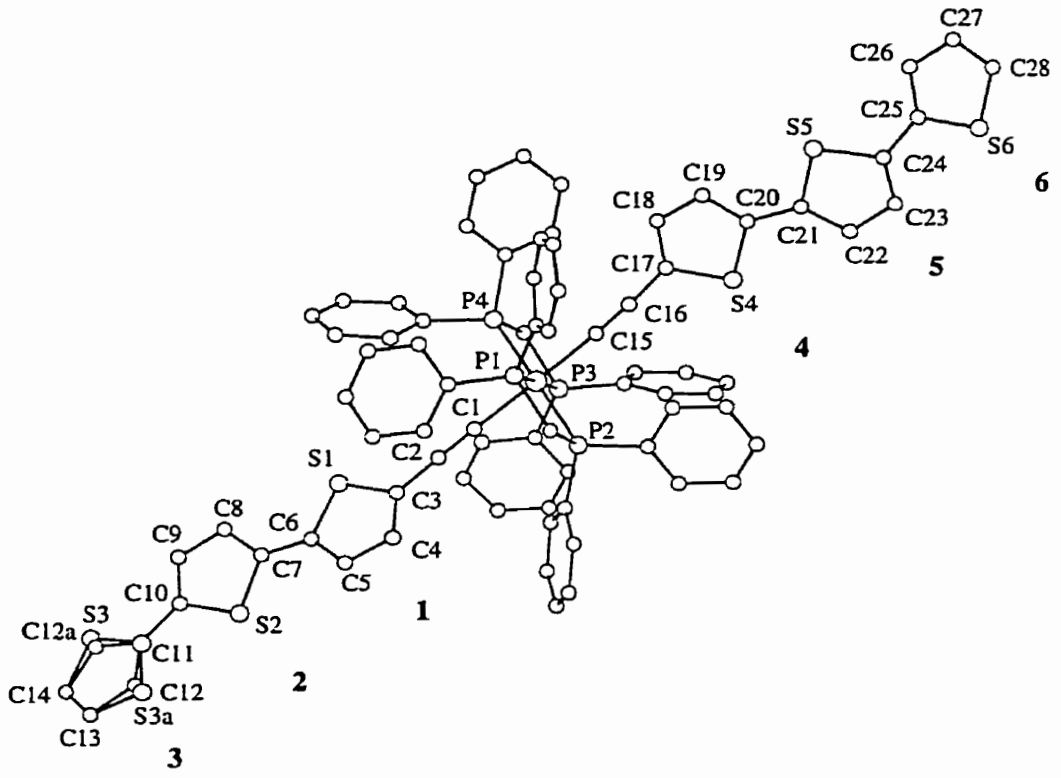

Figure 18. Solid-state molecular structure of **63c**.

3.3.2 Electrochemistry

Complexes **62a** – **c** all have two oxidation waves in their cyclic voltammograms (Figure 19) in the range 0.0 to 1.6 V vs SCE. Wave A is assigned to a $Ru^{II/III}$ redox process since it appears at similar potentials in all three complexes (Table 11). Related complexes *trans*-$Ru(dppm)_2(Cl)(C{\equiv}CR')$ (R' = Ph and 4-nitrophenyl) have oxidation waves due to the $Ru^{II/III}$ process with $E_{p,a}$ = 0.41 V vs SCE for R' = Ph and 0.59 V vs SCE for R' = 4-nitrophenyl.[149] Inspection of the first oxidation waves (A) for **62a** – **c** reveals features diagnostic of chemical irreversibility. For all these complexes plots of $i_{p,a}$ to $\nu^{1/2}$ (ν = scan rate)

deviate from linearity, and the ratio $i_{p,c}/i_{p,a}$ is less than 1 (Table 11), consistent with some of the oxidized species undergoing following chemical reactions.[150] These results suggest that isolation of the Ru^{III} complexes may be difficult, due to the instability of the oxidized species in solution. The $i_{p,c}/i_{p,a}$ ratio for **62c** is closest to 1.0, so the oxidized form of this complex is most likely to be sufficiently stable to isolate. Attempts to isolate the Ru^{III} complex by oxidation of **62c** using $FcPF_6$ obtain a deeply colored gray-green solid; however, this complex is found to be impure. The IR spectrum of this solid contains an unassigned band at 1920 cm^{-1} in addition to the expected peak at 1976 cm^{-1}.[136] In addition, electrochemical reduction of the oxidized **62c** yields other products in addition to **62c**, as indicated by new resonances in the ^{31}P NMR spectrum. Although all attempts to isolate the Ru^{III} complexes as pure solids are unsuccessful, these species can be spectroscopically characterized *in situ* (*vide infra*).

The second oxidation wave (B) in the CV of **62a** is clearly chemically irreversible. For complex **62b**, wave B becomes more reversible only at high scan rates ($\geq$ 100 mV/s), but is irreversible at slower scan rates. Wave B appears most chemically reversible for **62c**. The oxidation potential of wave B decreases significantly as the length of the oligothienyl ligand increases (Table 11). Based on this behavior, the second oxidation wave (B) is assigned to a thiophene-based oxidation. Electrochemical studies on oligothiophenes have shown that longer oligomers have lower oxidation potentials.[21,22] The potential of wave B in **62c** is lower and more reversible than the first oxidation wave in the CV of the organic oligomer **64c** ($E_{p,a}$ = 1.07 V vs SCE). At the potential of wave B the ruthenium in **62c** is already oxidized; yet, is still able to stabilize the ligand-based oxidation relative to the trimethylsilyl derivative **64c**. The CVs of complexes **63a – c** all contain multiple waves. Complexes **63a** and **63b** both show four distinct waves in the range 0 – 1.4 V vs SCE (Figure 20a and b). The lowest

potential waves (C for **63a**; G for **63b**) are assigned to a $Ru^{II/III}$ redox couple. Wave G is more reversible than wave C as shown by $i_{p,c}/i_{p,a}$ measurements, and wave C becomes more reversible at higher scan rates. The three irreversible waves (D, E and F for **63a**; H, I and J for **63b**) observed at higher potentials are assigned to ligand-based oxidations, as well as oxidation of products resulting from decomposition during the electrochemical experiment. It is very clear that the first ones of these multiple waves (D and H) are ligand-based and are likely due to the same process which gives rise to wave B in the CVs of **62a – c**.

For complex **63b** repeated scans over the range 0 – 1.4 V result in an increase in the current upon each subsequent scan (Figure 21a). This observation is consistent with deposition of conducting material on the electrode. Inspection of the electrode surface after multiple scans reveals the presence of an insoluble red film. During growth of the film, wave G decreases in intensity and eventually disappears, presumably due to the film blocking further monomer from reaching the electrode surface. This indicates that the film is insulating at 0.3 V vs SCE since a conducting film would allow oxidation of monomer in solution at this potential even if the monomer cannot penetrate to the electrode surface.

Bisacetylide **63c** shows four waves in its CV, all of which appear relatively reversible (Figure 20c). The $Ru^{II/III}$ wave (K) appears very close to where it is observed for **63a** and **63b**. The three waves (L, M and N) at higher potentials are due to ligand-based oxidation processes, by analogy with the results observed for **63a** and **63b**. When the concentration of the sample is increased, the shapes of the waves in the CV change as a result of deposition of conductive material on the electrode during the scan (Figure 21c, first scan). Multiple scans show clear evidence for this growth (Figure 21c), analogous to the observations for **63b**. Extended scanning of solutions containing lower concentrations of **63c** (3.5×10^{-4} M, as in

Figure 20c) also results in deposition of conducting material, albeit more slowly. Since the stability of the oxidized species formed under these conditions is in doubt, the exact nature of the conducting material formed in these experiments is unclear. It is possible that the material contains coordinated metal centers in addition to dimerized or polymerized oligothienyl ligands, or alternatively that decomposition of the complexes via ligand loss results in polythiophene-like conducting polymer films. No films form when **62a** – **c** and **63a** are scanned repeatedly under the same conditions.

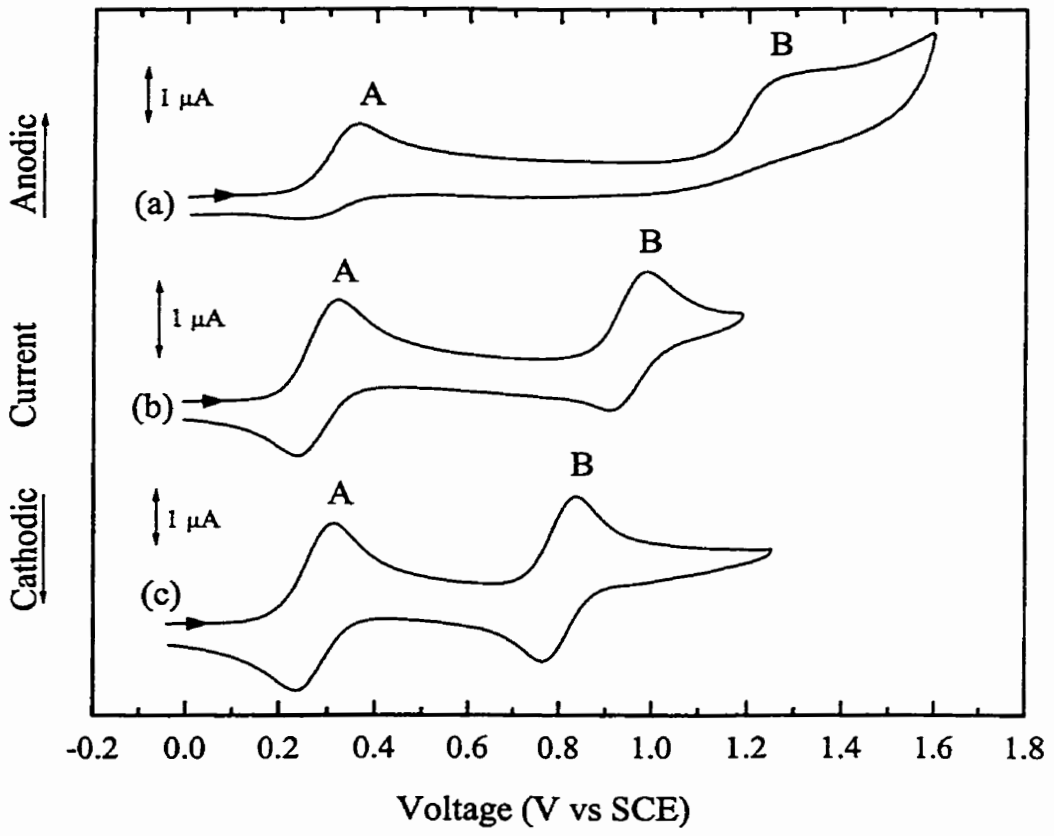

Figure 19. Cyclic voltammograms of (a) **62a** (2.2×10^{-3} M), (b) **62b** (1.6×10^{-3} M) and (c) **62c** (1.8×10^{-3} M) in CH_2Cl_2 containing 0.1 M $[(n\text{-}Bu)_4N]PF_6$. Scan rate = 100 mV/s.

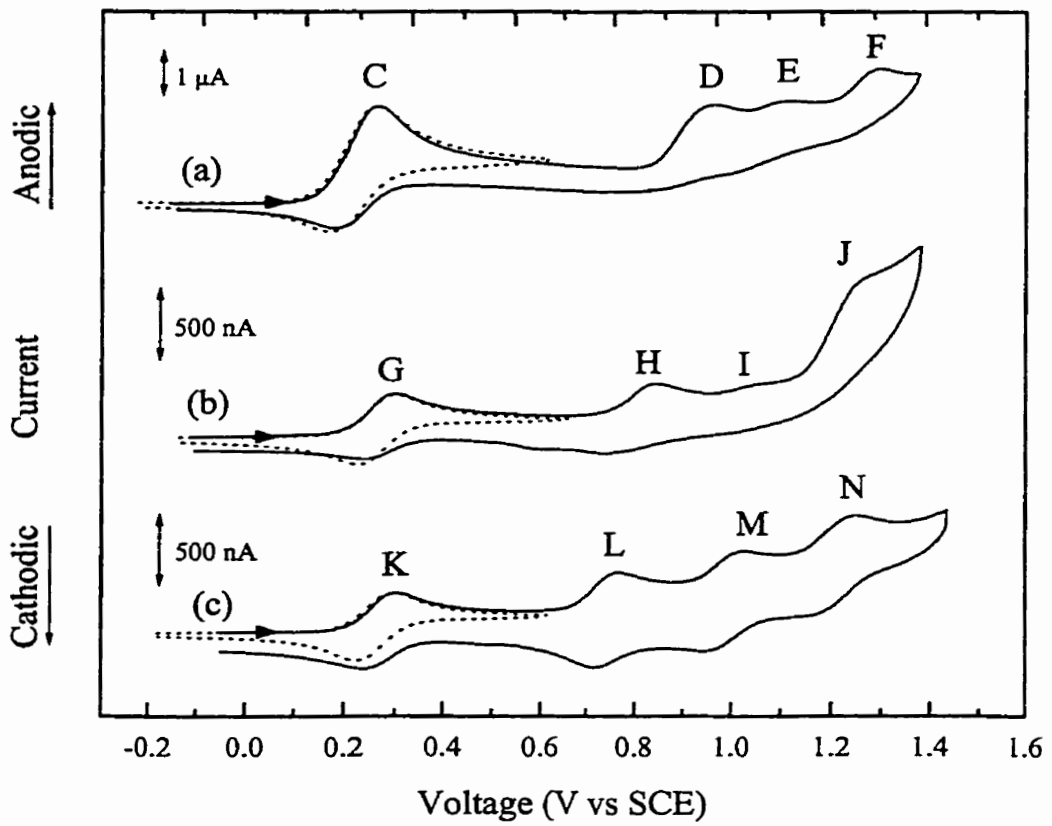

Figure 20. Cyclic voltammograms of (a) **63a**, (b) **63b** (4.0×10^{-4} M) and (c) **63c** (3.5×10^{-4} M) in CH_2Cl_2 containing 0.1 M $[(n\text{-}Bu)_4N]PF_6$. The scan rate = 100 mV/s. The dotted lines show the cyclic voltammograms in the range of –0.2 – 0.6 V vs SCE.

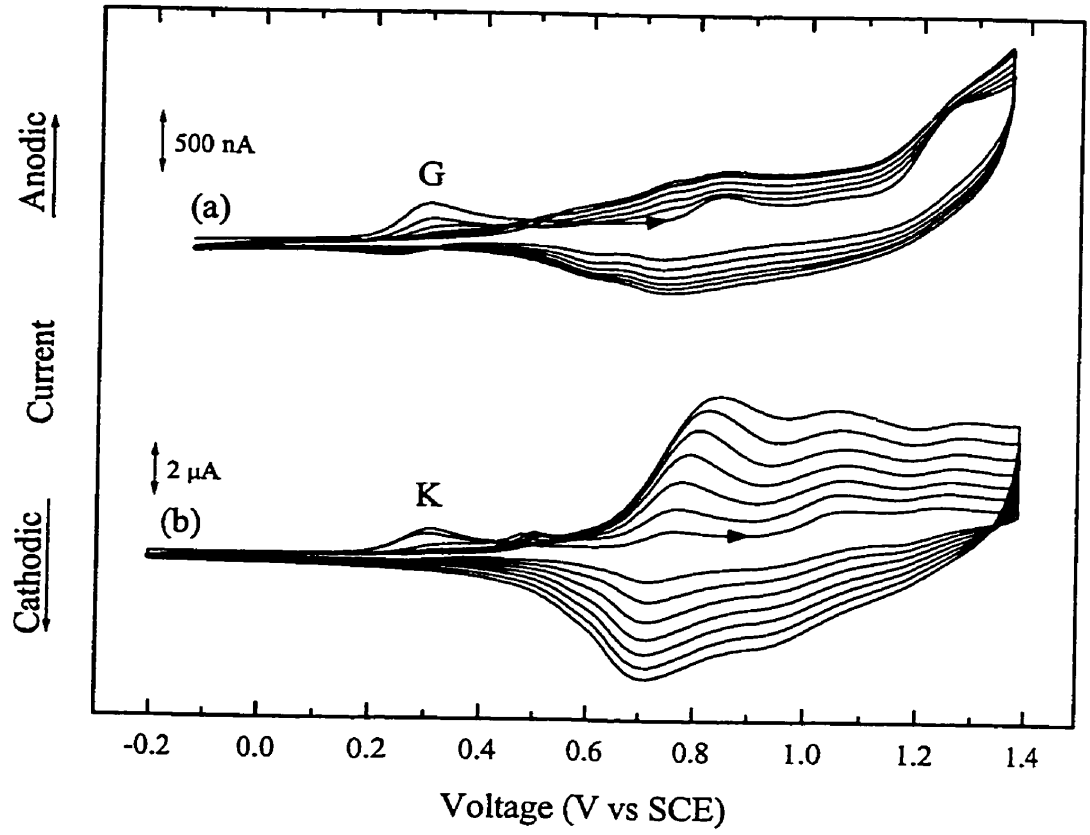

Figure 21. Multiple scan cyclic voltammograms of (a) **63b** (4.0×10^{-4} M) and (b) **63c** (1.8×10^{-3} M) in CH_2Cl_2 containing 0.1 M $[(n\text{-Bu})_4N]PF_6$ Scan rate = 100 mV/s.

Table 11. Spectroscopic and Electrochemical Data for **62a – c**

Complex	UV–vis–near-IR λ (nm) (ε ($M^{-1}cm^{-1}$))[a]	IR (KBr) $\nu_{C\equiv C}$ (cm^{-1})	$E_{p,a}$ ($Ru^{II/III}$)[a,b]	$i_{p,c}/i_{p,a}$[c]	$E_{p,a}(2)$[a,b]
62a	328 (14000)	2063	0.36	0.50	1.25
62b	406 (22000)	2056	0.32	0.89	0.99
62c	334 (sh) (11000), 450 (33000)	2053	0.30	0.94	0.84
62c$^+$	375 (13000), 580 (29000), 665 (sh) (17000), 1090 (29000)				
63a	338 (25000)	2050	0.33	0.59	0.98
63b	420 (53000)	2050	0.30	0.95	0.85
63c	340 (sh) (24000), 460 (75000)	2047	0.30	0.95	0.76
63c$^+$	400 (45000), 595 (28000), 1330 (23000), 1610 (sh) (16000)				
64c	384 (34000)	2139			1.07[d]

[a] CH_2Cl_2, 20 °C except for **62c**$^+$ and **63c**$^+$ which were obtained at –17 °C. [b] V vs SCE, Pt working electrode, 20 °C. [c] $Ru^{II/III}$ wave; scan rate = 100 mV/s. [d] first oxidation wave.

3.3.3 Spectroscopic Characterization

The frequencies of the infrared absorption bands for the C≡C groups in the complexes are collected in Table 11. The absorptions appear at similar energies for the whole series, and are significantly lower in energy than the corresponding absorption for 1-(trimethylsilyl)-2-(5-(2,2':5',2"-terthienyl))acetylene (**64c**) demonstrating the extent of backbonding of the Ru^{II} center with the acetylide.

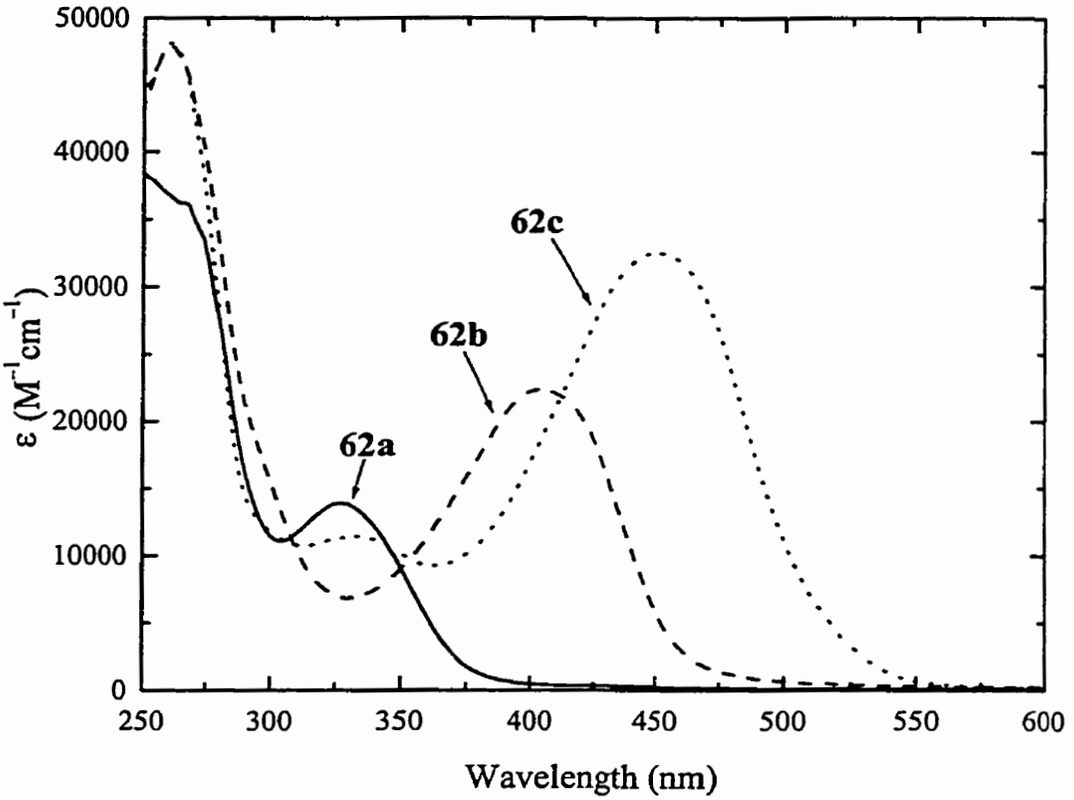

Figure 22. UV–vis spectra of **62a** (—), **62b** (– –) and **62c** (···) in CH_2Cl_2

The electronic spectra of **62a – c** and **63a – c** are shown in Figures 22 and 23 respectively. All the complexes exhibit strong ligand-based (dppm) absorption bands above 270 nm. Intense absorption bands with λ_{max} in the range 328 – 460 nm are assigned to thiophene-based $\pi - \pi^*$ transitions. These bands are absent in the spectra of analogous complexes which do not contain oligothienyl ligands, such as *trans*-$Ru(dppm)_2(Cl)(C{\equiv}CH)$,[151] and the extinction coefficients are in the range expected for such transitions.[152] These absorption bands are approximately twice as intense in the spectra of the diacetylides **63a – c** as the corresponding bands for the monoacetylides **62a – c**, and the

energy of the transition shifts to lower energy as the length of the oligothienyl ligand is increased. The energy of the $\pi - \pi^*$ absorption is 450 nm for **62c** and 460 nm for **63c**, while the absorption maximum for compound **64c** appears at 384 nm and 355 nm for 2,2':5',2"-terthiophene,[14] indicating that the electron-donating Ru^{II} reduces the $\pi - \pi^*$ energy. The differences in λ_{max} are small between the monoacetylide and diacetylide containing the same ligand, from which it is concluded that the $\pi - \pi^*$ transitions in the diacetylides are largely localized on each ligand rather than delocalized over the whole complex.

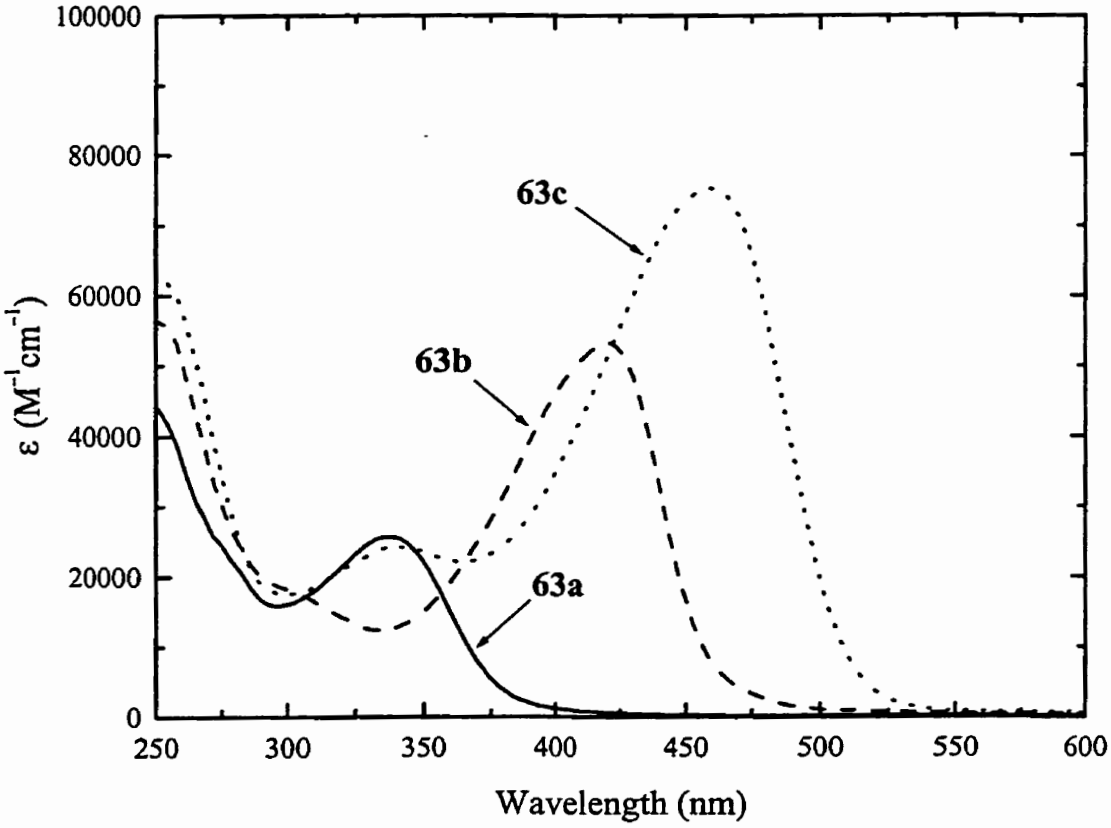

Figure 23. UV–vis spectra of **63a** (—), **63b** (– –) and **63c** (···) in CH_2Cl_2.

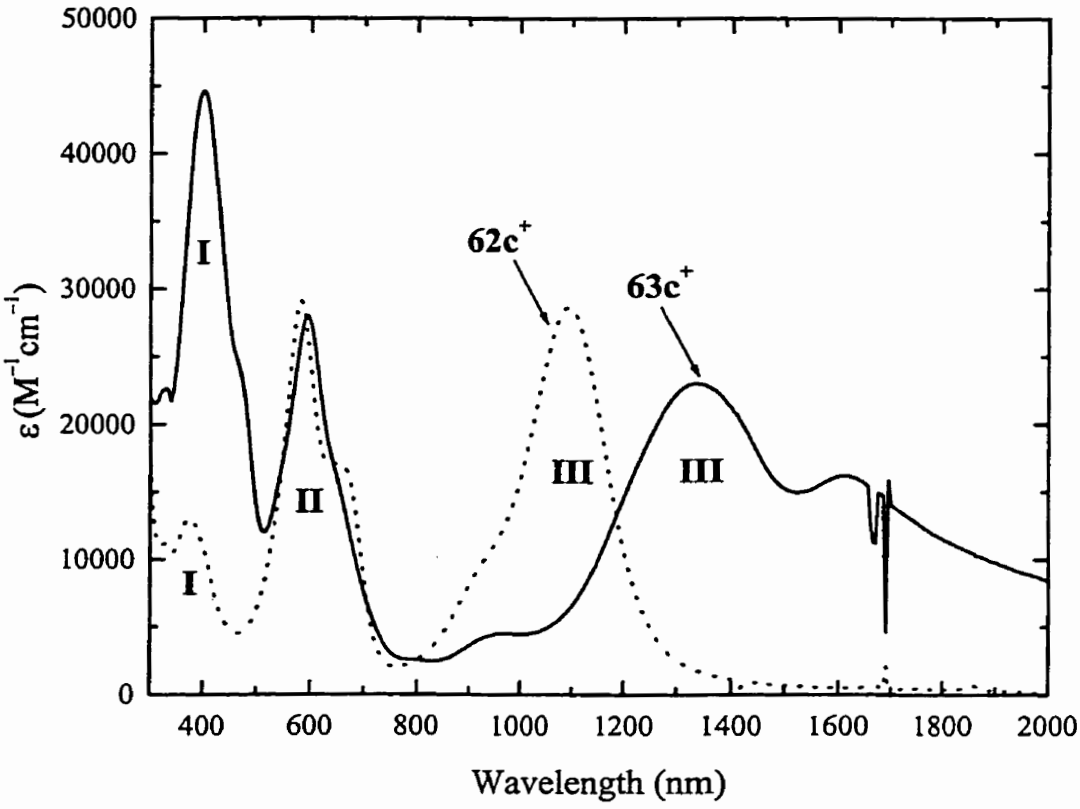

Figure 24. Vis–near-IR spectra of **62c**$^+$ (···) and **63c**$^+$ (—) in CH_2Cl_2 at –17 °C.

Due to the instability of the Ru^{III} complexes (*vide supra*) electronic spectra of these species cannot be obtained at room temperature; however, the solutions of the oxidized complexes can be prepared by the addition of one equivalent of a freshly prepared solution of $FcPF_6$ to a solution of the neutral complex in dry CH_2Cl_2 at –20 °C. The solutions are transferred to a spectrophotometric cell held at –17 °C, and the electronic spectra are obtained. The oxidation reactions are assumed to be complete when no further increase in the new

absorption bands is observed (within 30 min). After this time, the oxidized species **62c**$^+$ and **63c**$^+$ are stable in solution for at least 30 min with only slight changes in their absorption spectra. Complexes **62a**$^+$ – **b**$^+$, **63a**$^+$ – **b**$^+$ still decompose at this temperature as evidenced by changes in the color of the solutions, and the spectra of these complexes are not reproducible. For these complexes oxidation and decomposition of the Ru^{III} species occur at a comparable rate, resulting in mixtures of complexes in solution.

The electronic spectra of **62c**$^+$ and **63c**$^+$ at –17 °C are shown in Figure 24, and the data summarized in Table 11. In these spectra, three sets of bands (I – III) are observed in the visible and near-IR regions. The ferrocenium used in the preparation is reduced to ferrocene, which has a d – d transition in this region; however, it is very weak (441 nm, ε = 91 $M^{-1}cm^{-1}$)[153] and does not interfere with the observed spectra. Band I is assigned to the $\pi - \pi^*$ absorption of the terthienyl group. This absorption shifts to higher energy in the Ru^{III} species, since the metal center is less electron-donating than in the corresponding Ru^{II} complexes. Bands II and III consist of multiple, intense absorptions in the visible and near-IR region and are entirely absent in the spectra of the Ru^{II} analogs. Ru^{III} complexes frequently exhibit ligand-to-metal charge-transfer (LMCT) absorptions,[36,137] particularly with reducing-type ligands. Based on the intensities and energies of bands II and III these bands are assigned as LMCT bands from the terthienyl ligand to the Ru^{III}. Splitting of both ligand-donor orbitals and metal-acceptor orbitals would give rise to the multiple bands which are observed; however, it is not possible to assign these low-energy bands to specific transitions at this time.

3.4 Discussion

In complexes **62a – c** and **63a – c** the length of the oligothienyl group has a dramatic effect on the oxidation potential of this group; however, it does not significantly affect the $Ru^{II/III}$ oxidation potential. This is similar to the effects observed in bimetallic Fe^{II} ferrocenylacetylide complexes **8a** and **8b**.[56] The oxidation potential of the (Cp)(PP)Fe- moiety is –0.47 V vs Fc^+/Fc in **8a** (PP = dppm), and –0.84 V (PP = dmpe) in **8b**, while the oxidation potential of the ferrocenyl group is relatively constant at +0.12 V vs Fc^+/Fc in **8a** and +0.08 V in **8b**. Although the length of the oligothienyl ligand has little effect on the potential of the $Ru^{II/III}$ oxidation, the complexes containing the longer ligands are found to have more reversible $Ru^{II/III}$ oxidation waves. This is due to resonance delocalization of the positive charge in the Ru^{III} species onto the oligothienyl group. This resonance stabilization is greater for more conjugated ligands, and minimizes further chemical reactions of the oxidized complexes. This is consistent with the complete irreversibility of the $Ru^{II/III}$ wave in *trans*-$Ru(dppm)_2(Cl)(C{\equiv}CH)$,[151] in which no resonance stabilization is possible.

Charge delocalization in the monocations $\mathbf{62c}^+$ and $\mathbf{63c}^+$ may be evaluated by analysis of their electrochemical and spectroscopic data using Hush theory, which has been previously applied to LMCT processes.[34-36] The terthienyl-to-Ru^{III} LMCT in these oxidized species can be represented by the potential energy diagram in Figure 7b, and the energy of the LMCT correlates to the oxidation potential difference between the metal and oligothienyl groups (eqs 8 and 12). The difference in the oxidation potentials (ΔE) of the terthienyl ligand and the Ru center is 0.54 V in **62c** and 0.46 V in **63c**, and the complex with the smaller ΔE (**63c**) also has the lower energy LMCT band. The lowest energy absorptions are observed at 1090 nm in $\mathbf{62c}^+$, and 1330 nm with a shoulder at 1610 nm in $\mathbf{63c}^+$. Similarly, the difference in the

oxidation potentials for the two $Fe^{II/III}$ couples of **8a** (0.62 V) and **8b** (0.80 V) correlates with the energy of the IVCT band.[56] The monocation $\mathbf{8a}^+$ has an intense, broad IVCT band at 1595 nm, while $\mathbf{8b}^+$ has a band at 1295 nm.

3.5 Conclusions

The results in this Chapter support the conclusion that the π system of the conjugated oligothienyl ligands interacts electronically with the Ru center. The electron-donating Ru^{II} group decreases the energy of the $\pi - \pi^*$ transition in the oligothienyl ligands, and the energy of this transition increases when the Ru^{II} is oxidized. The reversibility of the $Ru^{II/III}$ oxidation wave improves as the length of the oligothienyl ligand is increased, indicating stabilization of the Ru^{III} species occurs via delocalization of positive charge from the metal to the oligothienyl ligand. The presence of low-energy charge-transfer transitions in the spectra of $\mathbf{62c}^+$ and $\mathbf{63c}^+$ is consistent with this delocalization.

These results suggest that polymers containing Ru centers bridged by oligothienyl linkers could be conductive; however, it is clear that polymers having these groups will require complete stability of the Ru center in both oxidation states, otherwise decomposition may result in the formation of material of ill-defined composition.

Chapter 4 Charge Delocalization in (Ferrocenylethynyl)oligothiophene Complexes

4.1 Introduction

The extent of charge delocalization in metal complexes will depend on the magnitude of the energy barrier to charge transfer between donor and acceptor (E_{th} as shown in Figure 7). As described in Chapter 2, the higher degree of charge delocalization in the ruthenium(II) bis(ferrocenylacetylide) complexes is observed when the difference in oxidation potentials between the terminal groups and the Ru center is smallest. The same trend is also observed for **62c**$^+$ and **63c**$^+$, which show oligothienyl-to-Ru^{III} LMCT bands in the near-IR region. These LMCT absorption bands have very similar features to the IVCT bands described in Chapter 2.

The electronic and optical properties of hybrid polymers which consist of metal and organic conjugated groups in the polymer backbone depend on charge delocalization along the polymer backbone. Insight into the extent of delocalization along the polymer backbone may be obtained by examining the LMCT processes in model complexes such as $Fc^+/Fc{-}{\equiv}{-}R$ and $Fc^+/Fc{-}{\equiv}{-}R{-}{\equiv}{-}Fc/Fc^+$ (R = conjugated organic groups). This Chapter describes the spectroscopic and electrochemical characterization of a series of compounds in which a metal center (ferrocene) is conjugated to oligothiophenes of varying oxidation potentials (**68a** – **e** and **69a** – **e**). Analysis of this data allows important conclusions to be made regarding charge delocalization in these complexes.

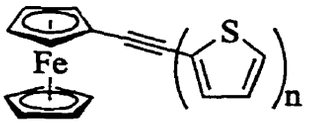

68a (n =1)
68b (n =2)
68c (n =3)

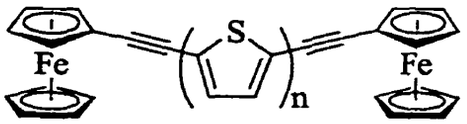

69a (n =1)
69b (n =2)
69c (n =3)

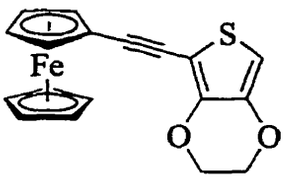

68d

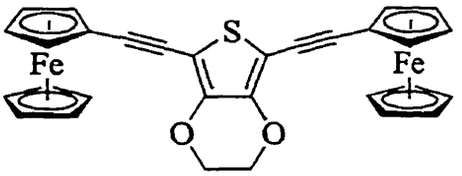

69d

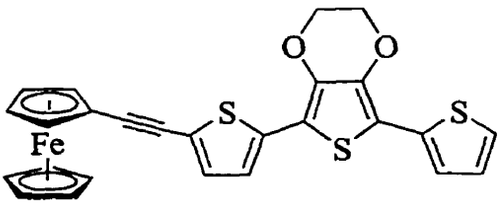

68e

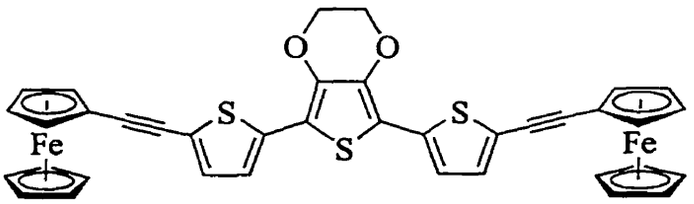

69e

4.2 Experimental

General. Procedures were the same as described in previous Chapters except as noted here. 5,5'-Dibromo-2,2'-bithiophene[146] and 5,5"-dibromo-2,2':5',2"-terthiophene[146] were prepared using literature procedures. 3,4-Ethylenedioxythiophene was a gift from Bayer Ltd. UV–vis–near-IR spectra of solutions of $\mathbf{68a}^{+} - \mathbf{e}^{+}$ and $\mathbf{69a}^{2+} - \mathbf{e}^{2+}$ in CH_2Cl_2 containing 0.10 M $[(n\text{-}Bu)_4N]PF_6$ were obtained on a Varian Cary 5 spectrometer.

Electrochemistry. Cyclic voltammograms were obtained under nitrogen at room temperature in a CH_2Cl_2 solution containing $4 - 6 \times 10^{-3}$ M complex and 0.5 M $[(n\text{-}Bu_4)N]PF_6$. Before addition of dry solvent the cells containing the electrodes and electrolyte were dried *in vacuo* at 90 °C overnight. Electrolyses of **68a** – **e** and **69a** – **e** were conducted in a CH_2Cl_2 solution containing 0.10 M $[(n\text{-}Bu)_4N]PF_6$ using Pt mesh electrodes and a $Ag/AgNO_3$ (CH_3CN) reference electrode (0.39 V vs SCE).

2,5-Dibromo-3,4-ethylenedioxythiophene. This complex was prepared by a modification of the literature method.[154] 3,4-Ethylenedioxythiophene (1.42 g, 10.0 mmol) was dissolved in THF/CH_3COOH (40 mL, 1:1 v/v), and *N*-bromosuccinimide (3.74 g, 21.0 mmol) was added. After the solution was stirred at room temperature for 2 h, distilled water (100 mL) was added resulting in the precipitation of a silver-white crystalline solid. The solid was isolated by filtration, and dried over P_2O_5. Yield: 2.6 g (87%).

3',4'-Ethylenedioxy-2,2':5',2"-terthiophene. Mg foil (0.60 g, 25 mmol) and one grain of I_2 were added to a dry flask charged with dry diethyl ether (80 mL). The suspension was stirred for 10 min, and a solution of 2-bromothiophene (3.60 g, 22.0 mmol) in diethyl ether (20 mL) was then added dropwise over 30 min via a pressure-equalized addition funnel. After addition, the solution was heated at reflux for 2 h, and then cooled to room temperature. This solution was added to a solution of 2,5-dibromo-3,4-ethylenedioxythiophene (3.0 g, 10 mmol) and Ni(dppp)Cl_2 (0.27 g, 0.50 mmol) in diethyl ether (50 mL) via a filter paper-tipped cannula. The mixture was then heated at reflux overnight. After the solution was cooled to room temperature, the reaction was quenched by addition of 1 M aq HCl (50 mL). The organic layer was collected, washed with distilled water (2 × 50 mL) and dried over anhydrous $MgSO_4$. After filtration, removal of the solvent resulted in an orange oil, which was purified by flash chromatography on silica gel using hexanes/diethyl ether (9:1 v/v) as eluant. The product was used without further purification in the next step. Yield: 3.02 g. ^{1}H NMR (400 MHz, d_6-benzene): δ 7.27 (dd, J = 3.6, 1.1 Hz, 2H), 6.81 (dd, J = 5.1, 1.1 Hz, 2H), 6.75 (dd, J = 5.1, 3.6 Hz, 2H), 3.35 (s, 4H).

5-Bromo-3',4'-ethylenedioxy-2,2':5',2"-terthiophene. 3',4'-Ethylenedioxy-2,2':5',2"-terthiophene (1.00 g, 3.03 mmol) was dissolved in THF/CH_3COOH (40 mL, 1:1

v/v). *N*-Bromosuccinimide (0.55 g, 3.1 mmol) was added to the solution while the solution was stirred rapidly. After addition, the solution was stirred for another 1 h, then distilled water (50 mL) was added to induce the precipitation of a yellow solid which was collected by filtration. The crude yellow solid was dried over P_2O_5, and the product was purified by chromatography on silica gel using CH_2Cl_2/hexanes (1:4 v/v) as eluant. Yield: 0.45 g (39%). ^{1}H NMR (400 MHz, d_6-benzene): δ 7.26 (d, J = 2.9 Hz, 1H), 6.81 (d, J = 4.9 Hz, 1H), 6.73 – 6.76 (m, 2H), 6.64 (d, J = 3.9 Hz, 1 H), 3.21 – 3.35 (m, 4H). Anal. Calcd $C_{14}H_9BrO_2S_3$: C 43.64, H 2.35. Found: C 43.03, H 2.27.

5,5"-Dibromo-3',4'-ethylenedioxy-2,2':5',2"-terthiophene. 3',4'-Ethylenedioxy-2,2':5',2"-terthiophene (1.00 g, 3.03 mmol) was dissolved in THF/CH_3COOH (40 mL, 1:1 v/v). *N*-Bromosuccinimide (1.13 g, 6.36 mmol) was added portionwise while the solution was stirred rapidly. After addition the solution was stirred for 2 h, during which time a yellow solid formed. Distilled water (50 mL) was added to induce the precipitation of more yellow solid, which was collected by filtration. The yellow solid was dissolved in CH_2Cl_2 (50 mL), and the solution was washed with distilled water (50 mL) and dried over anhydrous $MgSO_4$. After filtration, removal of the solvent yielded a yellow solid, which was purified by recrystallization from toluene. Yield: 1.04 g (71%). ^{1}H NMR (400 MHz, d_6-benzene): δ 6.72 (d, J = 3.9 Hz, 2H), 6.65 (d, J = 3.9 Hz, 2H), 3.22 (s, 4H). Anal. Calcd $C_{14}H_8Br_2O_2S_3$: C 36.22, H 1.74. Found: C 35.93, H 1.65.

2-Ferrocenylethynylthiophene (68a). Ethynylferrocene (0.38 g, 1.8 mmol) was added to a solution of 2-bromothiophene (0.25 g, 1.5 mmol), trans-$Pd(PPh_3)_2Cl_2$ (53 mg, 0.076 mmol), CuI (15 mg, 0.077 mmol) and diisopropylamine (0.30 g, 3.0 mmol) in dry THF (50 mL). The solution was stirred and heated at reflux overnight. After the solution was

cooled to room temperature, distilled water (50 mL) was added to quench the reaction. The solution was extracted with CH_2Cl_2 (2 × 40 mL). The organic layers were combined, washed with brine (50 mL) and distilled water (50 mL), and dried over anhydrous $MgSO_4$. Removal of the solvent resulted in a brown solid, which was purified by flash chromatography on silica gel using hexanes as eluant. Yield: 0.30 g (68%). ^{1}H NMR (400 MHz, CD_2Cl_2): δ 7.27 (dd, J = 1.1, 5.2 Hz, 1H), 7.21 (dd, J = 1.1, 3.6, 1H), 7.00 (dd, J = 3.6, 5.2, 1H), 4.50 (t, J = 1.8 Hz, 2H), 4.27 (t, J = 1.8 Hz, 2H), 4.25 (s, 5H). Anal. Calcd $C_{16}H_{12}FeS$: C 65.77, H 4.14. Found: C 66.14, H 4.27.

5-Ferrocenylethynyl-2,2'-bithiophene (68b). This complex was prepared as described for **68a** using 5-bromo-2,2'-bithiophene. The product was purified by flash chromatography on silica gel using CH_2Cl_2/hexanes (1:20 v/v) as eluant. Yield: 74%. ^{1}H NMR (400 MHz, CD_2Cl_2): δ 7.27 (dd, J = 1.0, 5.1 Hz, 1H), 7.21 (dd, J = 1.1, 3.6, 1H), 7.11 (d, J = 3.8 Hz, 1H), 7.06 (d, J = 3.8 Hz, 1H), 7.04 (dd, J = 3.6, 5.1, 1H), 4.51 (t, J = 1.7, 2H), 4.29 (t, J = 1.7, 2H), 4.26 (s, 5H). Anal. Calcd $C_{20}H_{14}S_2Fe$: C 64.18, H 3.77. Found: C 64.24, H 3.78.

5-Ferrocenylethynyl-2,2':5',2"-terthiophene (68c). This complex was prepared as described for **68a** using 5-iodo-2,2':5',2"-terthiophene. The product was purified by flash chromatography on silica gel using CH_2Cl_2/hexanes (1:3 v/v) as eluant. Yield: 25%. ^{1}H NMR (400 MHz, $CDCl_3$): δ 7.21 (dd, J = 1.1, 5.1 Hz, 1H), 7.17 (dd, J = 1.1, 3.6, 1H), 7.08 (d, J = 3.8 Hz, 1H), 7.06 (s, 2H), 7.00 – 7.02 (m, 2H), 4.49 (t, J = 1.8, 2H), 4.24 – 4.25 (m, 7H) Anal. Calcd $C_{24}H_{16}S_3Fe$: C 63.16, H 3.53. Found: C 62.85, H 3.43.

5-Ferrocenylethynyl-3,4-ethylenedioxythiophene (68d). A solution of *n*-BuLi (4.0 mL, 1.6 M in hexanes, 6.4 mmol) was cooled to –78 °C and added dropwise to a solution of

2,5-dibromo-3,4-ethylenedioxythiophene (1.8 g, 6.0 mmol) in dry THF (40 mL). The solution was then warmed up to room temperature, and the reaction was quenched by adding 1 M aq HCl (30 mL). The solution was extracted with CH_2Cl_2 (2 × 30 mL), and the organic layers were combined and dried over anhydrous $MgSO_4$. Removal of the solvent yielded 1.0 g of pale yellow 2-bromo-3,4-ethylenedioxythiophene, which was used without purification to prepare **68d**, following the same procedure described for **68a**. Pure **68d** was obtained by flash chromatography on silica gel using CH_2Cl_2/hexanes (1:2.5 v/v) as eluant. Yield: 18%. ^{1}H NMR (400 MHz, CD_2Cl_2): δ 6.27 (s, 1H), 4.48 (t, J = 1.8 Hz, 2H), 4.28 – 4.30 (m, 2H), 4.26 (t, J = 1.8 Hz, 2H), 4.24 (s, 5H), 4.19 – 4.21 (m, 2H). Anal. Calcd $C_{18}H_{14}O_2SFe$: C 61.73, H 4.03. Found: C 61.43, H 3.98.

5-Ferrocenylethynyl-3',4'-ethylenedioxy-2,2':5',2''-terthiophene (68e). This complex was prepared as described for **68a** using 5-bromo-3',4'-ethylenedioxy-2,2':5',2''-terthiophene. The product was purified by flash chromatography on silica gel using CH_2Cl_2/hexanes (1:3 v/v) as eluant. Yield: 62%. ^{1}H NMR (400 MHz, CD_2Cl_2): δ 7.25 – 7.27 (m, 2H), 7.12 (d, J = 3.9 Hz, 1H), 7.09 (d, J = 3.9 Hz, 1H), 7.04 (dd, J = 3.8, 5.0 Hz, 1H), 4.50 (t, J = 1.8 Hz, 2H), 4.40 (s, 4H), 4.28 (t, J = 1.8 Hz, 2H), 4.26 (s, 5H). Anal. Calcd $C_{26}H_{18}O_2S_3Fe$: C 60.70, H 3.53. Found: C 60.57, H 3.56.

2,5-Bis(ferrocenylethynyl)thiophene (69a). Ethynylferrocene (0.52 g, 2.5 mmol) was added to a solution of 2,5-dibromothiophene (0.24 g, 1.0 mmol), $Pd(PPh_3)_2Cl_2$ (70 mg, 0.10 mmol), CuI (20 mg, 0.10 mmol) and diisopropylamine (0.30 g, 3.0 mmol) in dry THF (50 mL). The solution was stirred and heated at reflux overnight. After the solution was cooled to room temperature, distilled water (30 mL) was added to quench the reaction. The solution was extracted with CH_2Cl_2 (2 × 40 mL). The organic layers were collected and

combined, washed with brine (50 mL) and distilled water (50 mL), and then dried over anhydrous $MgSO_4$. Removal of the solvent yielded a brown solid, which was purified by flash chromatography on silica gel using CH_2Cl_2/hexanes (1:4 v/v) as eluant. Yield: 0.41 g (82%). ^{1}H NMR (400 MHz, $CDCl_3$): δ 7.04 (s, 2H), 4.49 (t, J = 1.8 Hz, 4H), 4.25 (t, J = 1.8 Hz, 4H), 4.24 (s, 10H). Anal. Calcd $C_{28}H_{20}S_2Fe_2$: C 67.23, H 4.03. Found: C 67.29, H 3.91.

5,5'-Bis(ferrocenylethynyl)-2,2'-bithiophene (69b). This complex was prepared as described for **69a** using 5,5'-dibromo-2,2'-bithiophene. The product was purified by flash chromatography on silica gel using CH_2Cl_2/hexanes (1:3 v/v) as eluant. Yield: 80%. ^{1}H NMR (400 MHz, $CDCl_3$): δ 7.09 (d, J = 3.8 Hz, 2H), 7.02 (d, J = 3.8 Hz, 2H), 4.49 (t, J = 1.8 Hz, 4H), 4.25 (t, J = 1.8 Hz, 4H), 4.24 (s, 10H). Anal. Calcd $C_{32}H_{22}S_2Fe_2$: C 66.00, H 3.81. Found: C 66.11, H 3.70.

5,5"-Bis(ferrocenylethynyl)-2,2':5',2"-terthiophene (69c). This complex was prepared as described for **69a** using 5,5"-dibromo-2,2':5',2"-terthiophene. The product was purified by flash chromatography on silica gel using CH_2Cl_2/hexanes (3:7 v/v) as eluant. Yield: 65%. ^{1}H NMR (400 MHz, $CDCl_3$): δ 7.09 (d, J = 3.8 Hz, 2H), 7.06 (s, 2H), 7.02 (d, J = 3.8, 2H), 4.49 (t, J = 1.8, 4H), 4.25 (t, J = 1.8 Hz, 4H), 4.24 (s, 10H). Anal. Calcd $C_{36}H_{24}S_3Fe_2$: C 65.07, H 3.64. Found: C 65.38, H 3.68.

2,5-Bis(ferrocenylethynyl)-3,4-ethylenedioxythiophene (69d). This complex was prepared as described for **69a** using 2,5-dibromo-3,4-ethylenedioxythiophene. The product was purified by recrystallization from layered hexanes/CH_2Cl_2 solution, following by flash chromatography on silica gel using diethyl ether/hexanes (1:2 v/v) as eluant. Yield: 34%. ^{1}H NMR (400 MHz, CD_2Cl_2): δ 4.50 (t, J = 1.8 Hz, 4H), 4.31 (s, 4H), 4.28 (t, J = 1.8 Hz, 4H), 4.25 (s, 10H). Anal. Calcd $C_{30}H_{22}O_2SFe_2$: C 64.55, H 3.97. Found: C 63.94, H 3.98.

5,5"-Bis(ferrocenylethynyl)-3',4'-ethylenedioxy-2,2':5',2"-terthiophene (69e). This complex was prepared as described for **69a** using 5,5"-dibromo-3',4'-ethylenedioxy-2,2':5',2"-terthiophene. The product was purified by recrystallization from a layered CH_2Cl_2/hexanes solution, following by flash chromatography on silica gel using diethyl ether/hexanes (1:2 v/v) as eluant. Yield: 36%. ^{1}H NMR (400 MHz, CD_2Cl_2): δ 7.09 – 7.14 (m, 4H), 4.50 (t, J = 1.8 Hz, 4H), 4.42 (s, 4H), 4.29 (t, J = 1.8 Hz, 4H), 4.26 (s, 10H). Anal. Calcd $C_{38}H_{26}O_2S_3Fe_2$: C 63.17, H 3.63. Found: C 62.46, H 3.62.

4.3 Results and Interpretation

4.3.1 Syntheses

Compounds **68a** and **69a** are prepared by coupling ethynylferrocene with mono- and dibromothiophene, respectively, using trans-$Pd(PPh_3)_2Cl_2$ and CuI catalysts (Scheme 17), and **68b** –**e** and **69b** – **e** are obtained using the same procedures. The compounds are purified either by chromatography on silica gel or by recrystallization from CH_2Cl_2/hexanes or toluene, and characterized using ^{1}H NMR and UV–vis spectroscopies and C, H elemental analyses.

Scheme 17

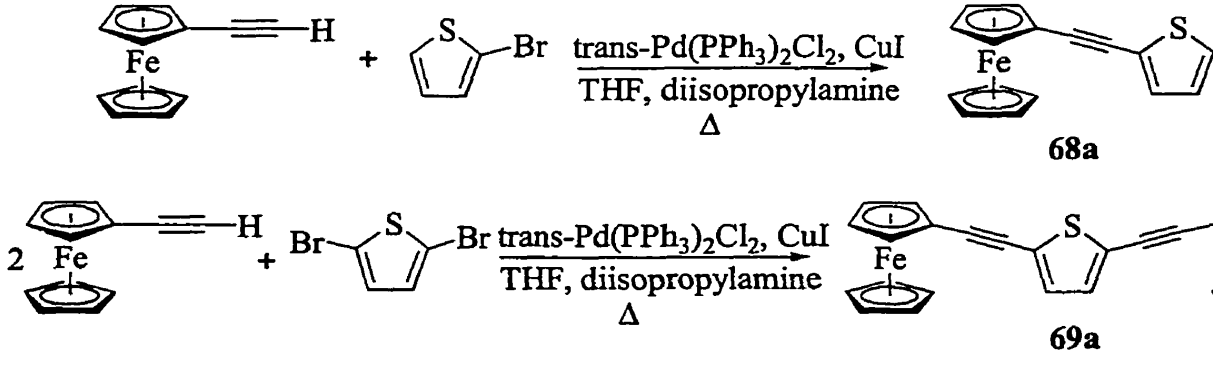

4.3.2 Electrochemistry

Complexes **68a – e** and **69a – e** all contain ferrocenyl and oligothiophene groups which are both expected to show redox activity. The reversibility and relative oxidation potentials of the redox processes in these compounds are determined by CV in CH_2Cl_2 solution containing 0.5 M $[(n\text{-Bu})_4N]PF_6$. All the compounds have two oxidation waves in the range 0 – 1.8 V vs SCE (Figures 25 and 26), and the potentials for these waves are collected in Table 12.

Table 12. Electrochemical and UV–vis Spectroscopic Data for **68a – e** and **69a – e**

Complex	$E_{1/2}(1)$ ± 0.01 (V)[a]	$E_{p,a}(2)$ ± 0.01 (V)[a]	ΔE ± 0.02 (V)[a,b]	λ_{max} (nm) (ε ($M^{-1}cm^{-1}$))[c]
68a	0.55	1.67	1.12	305 (14000), 445 (610)
68b	0.55	1.40	0.85	350 (25000), 445 (1600) (sh)
68c	0.55	1.13	0.58	392 (35000)
68d	0.53	1.47	0.94	310 (13000), 445 (610)
68e	0.53	0.91	0.38	406 (39000)
69a	0.56	1.68	1.12	342 (26000), 446 (3300) (sh)
69b	0.55	1.42	0.87	390 (38000)
69c	0.55	1.23	0.68	416 (44000)
69d	0.56	1.50	0.94	352 (27000), 448 (3700) (sh)
69e	0.54	1.04	0.50	433 (52000)

[a] Volts vs SCE, Pt working electrode, CH_2Cl_2 containing 0.5 M $[(n\text{-Bu})_4N]PF_6$, 20 °C. [b] $\Delta E = [E_{p,a}(2) - E_{1/2}(1)]$. [c] CH_2Cl_2 solution.

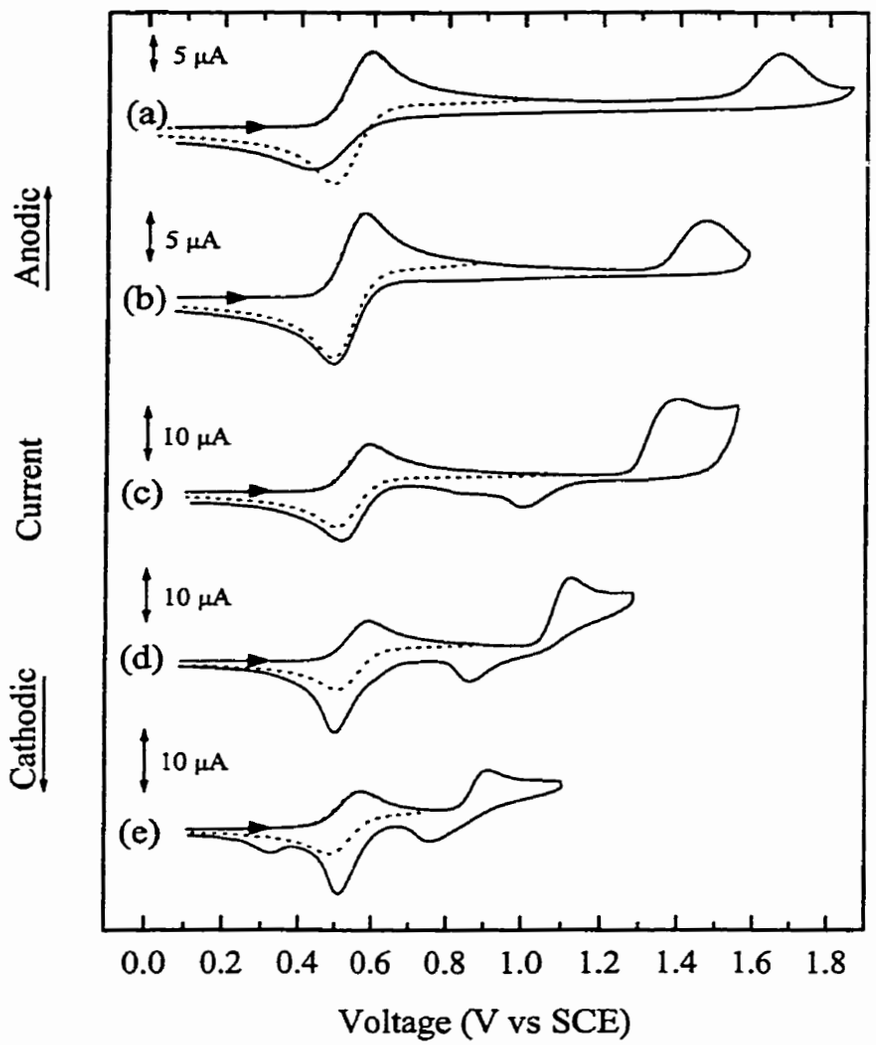

Figure 25. Cyclic voltammograms of (a) **68a**, (b) **68d**, (c) **68b**, (d) **68c** and (e) **68e** in CH_2Cl_2 containing 0.5 M $[(n\text{-}Bu_4)N]PF_6$. Scan rate = 100 mV/s.

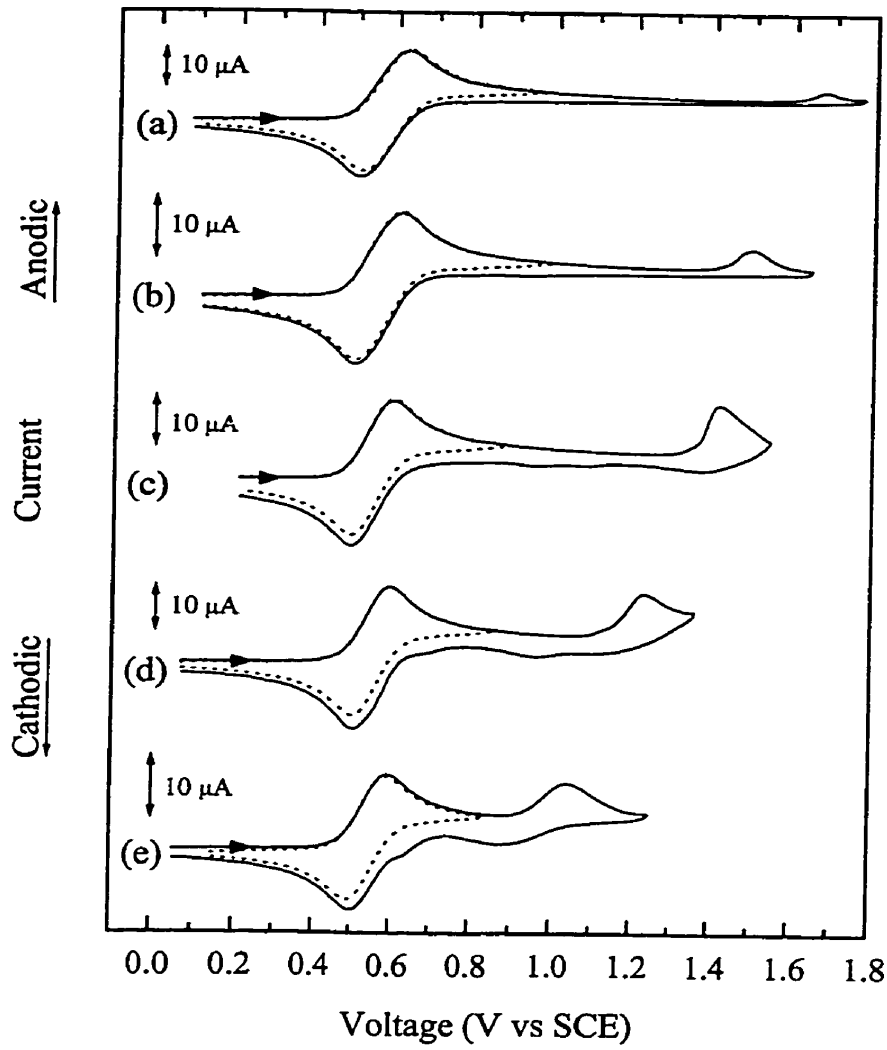

Figure 26. Cyclic voltammograms of (a) **69a**, (b) **69d**, (c) **69b**, (d) **69c** and (e) **69e** in CH_2Cl_2 containing 0.5 M $[(n\text{-}Bu)_4N]PF_6$. Scan rate = 100 mV/s.

The first oxidation wave is reversible and occurs at a potential very close to that of the $Fe^{II/III}$ couple in ethynylferrocene ($E_{1/2}$ = 0.57 V vs SCE); therefore, this wave is assigned to the $Fe^{II/III}$ redox couple. The compounds containing two ferrocenyl groups (**69a – e**) show

only a single-oxidation wave for these centers, indicating that there is little ground-state interaction between the metal centers over the conjugated oligothiophene bridge. In the series of all-*trans* compounds Fc–$(CH{=}CH)_n$–Fc (n = 1 – 6), peak separations are observed only for $n \leq 3$,[45] while for Fc–$CH{=}CHC_6H_4CH{=}CH$–Fc no peak separation is observed.[44] Thus, it is not surprising that no separation is observed in **2a – e**, in which the Fe – Fe distance is considerably longer.

The second oxidation wave in the cyclic voltammograms of all the compounds is irreversible (Figures 25 and 26), and the oxidation potential depends strongly on the nature of the oligothiophene group. Both longer conjugation length and the presence of electron-donating ethylenedioxy substituents (in **68d, 68e, 69d** and **69e**) result in a decrease in the potential of this wave. On the basis of these observations the second wave is assigned to an oligothiophene-based oxidation, the potential of which varies from 0.91 to 1.68 V vs SCE. The peak current of the second wave varies due to the differences in the stabilities of the resulting dications.

Complexes **68a – e** all contain a terminal thiophene ring with an unsubstituted α position, and these compounds are consequently good candidates to undergo α–α coupling when oxidized. The second oxidation waves of **68a** and **68d** are completely irreversible, and no new reduction waves which would be evidence of dimerization are observed (Figure 25a and 25b). On the other hand, the cyclic voltammograms of **68b**, **68c** and **68e** all contain a number of features which indicate dimerization is occurring (Figure 25c – e). For all three compounds a new reduction wave appears after the first scan past the thiophene-oxidation wave. In subsequent scans, these reduction waves have corresponding oxidation features, and when solutions of these compounds are cycled repeatedly past the thiophene-oxidation wave

(0.7 – 1.5 V vs SCE for **68b**, 0 – 1.3 V for **68c** and 0 – 1.1 V for **68e**), an electrochromic film deposits on the electrode surface. The films are orange-red in the neutral state, and black when fully oxidized.

Characterization of these films by CV in monomer-free solution reveals a reversible wave at ~ 0.5 V vs SCE due to the $Fe^{II/III}$ couple as well as other waves assigned to oxidation of the oligothiophene groups (Figure 27). The electrodeposited films are proposed to consist of dimers **70**, **71** and **72**.

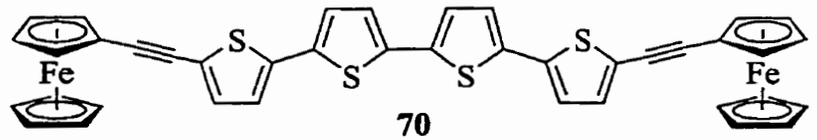

70

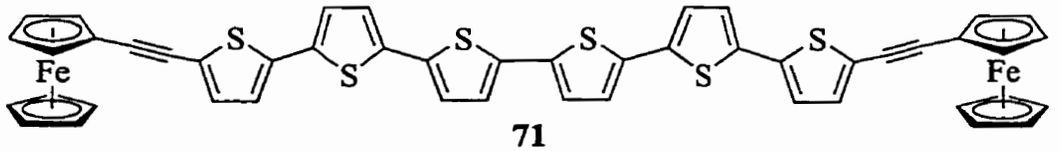

71

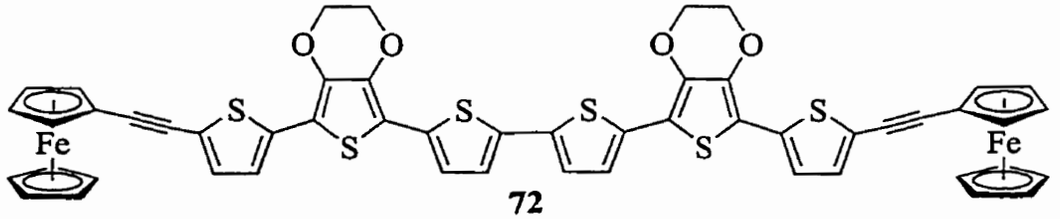

72

The oxidation wave at 1.01 V in **70** (Figure 27a) is quasireversible and occurs at a lower potential than the oxidation of the terthiophene group in **69c**. This is consistent with the presence of a longer tetrathiophene bridge in this dimer. The new reduction wave at 0.63 V vs SCE may be due to a similar process to that observed in the CVs of **69c** and **69e** (*vide infra*).

The CV of **71** (Figure 27b) contains two oxidation waves with $E_{1/2}$ at 0.51 and 0.91 V vs SCE. The wave at 0.51 V has a shoulder on the high potential side, which may be due to overlap between the $Fe^{II/III}$ oxidation and an oligothiophene oxidation wave. In **71**, the bridge consists of a sexithiophene group. These have been shown to support two reversible one-

electron oxidations, for instance, in didodecylsexithiophene the first oxidation occurs at 0.34 V, and the second occurs at 0.54 V vs Fc^{+}/Fc.[23]

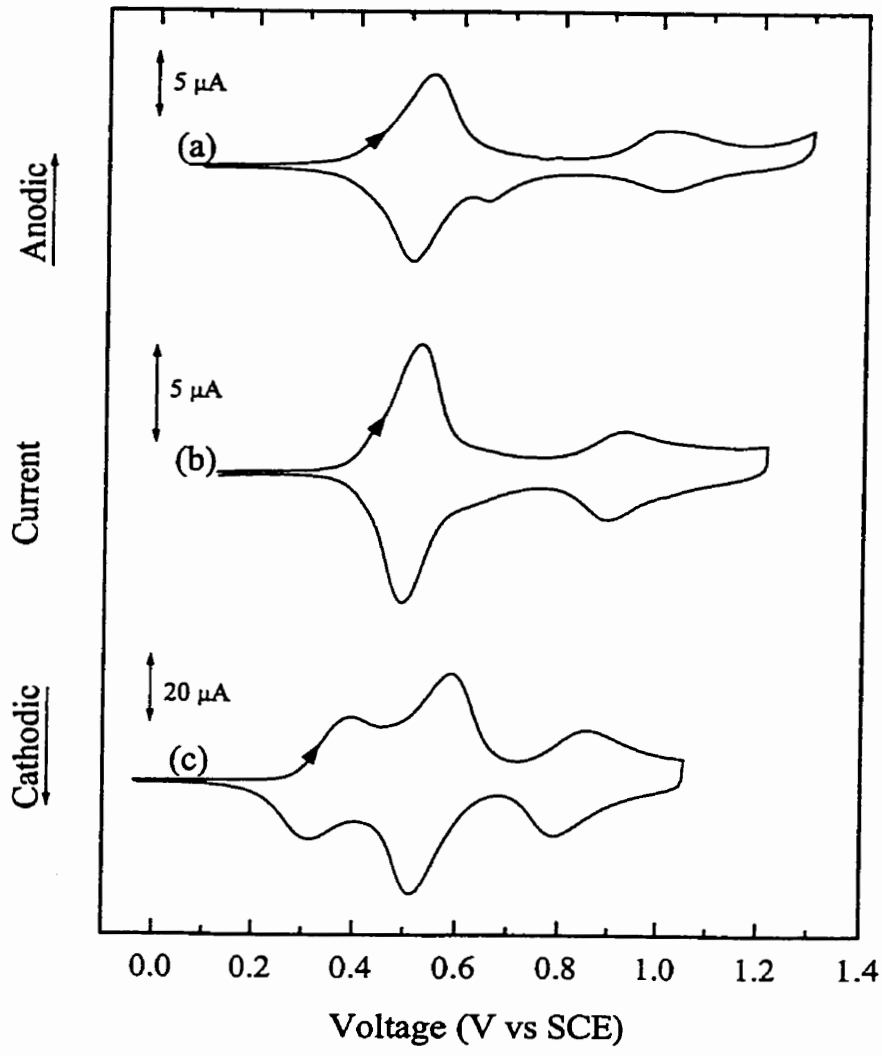

Figure 27. Cyclic voltammograms of (a) **70**, (b) **71** and (c) **72** in CH_2Cl_2 containing 0.5 M $[(n\text{-}Bu)_4N]PF_6$. Scan rate = 100 mV/s.

The CV of the dimer **72** shows similar features, with the waves having $E_{1/2}$ at 0.35 and 0.82 V vs SCE assigned as sequential, reversible oxidations of the substituted sexithiophene bridge. The electron-donating ethylenedioxy groups in **72** result in lower potential waves for the bridge compared to **71**. In **72** the bridge is oxidized at a lower potential than the ferrocenyl groups, and it is possible that an increase in the conductivity of the molecular wire linking the two terminal groups could lead to splitting in the potentials of the ferrocenyl waves; however, no splitting in this case is observed, possibly due to poor orbital overlap between the oligothiophene and the ethynyl linkage.

For complexes **69a**, **69b** and **69d** the oligothiophene-oxidation waves are irreversible, and no new reduction waves are observed; however, for **69c** and **69e** the second oxidation waves become more reversible at higher scan rates, and new reduction features appear (Figure 26). For example, at a scan rate of 100 mV/s a small reduction wave is observed at 0.96 V for **69c** and at 0.64 V vs SCE for **69e**. This wave is likely due to the reduction of the product resulting from coupling of **69c** or **69e** upon oxidation past the oligothiophene-oxidation potential, analogous to the behavior of **68c**, **68d** and **68e**. Although the disubstituted complexes do not have unsubstituted α positions available, it is possible that $\beta - \beta$ coupling occurs in these compounds.

4.3.3 Spectroscopic Characterization

The UV–vis spectra of **68a – e** and **69a – e** all contain very strong absorption bands with λ_{max} between 305 and 433 nm, and these bands are assigned to an oligothiophene $\pi - \pi^*$ transition (Table 12). As expected, the absorption red-shifts and becomes more intense with an increase in the length of the oligothiophene group. The presence of the electron-donating

ethylenedioxy groups results in a slight decrease in the absorption maximum relative to the unsubstituted compound with an equally long oligothiophene group. Several of the compounds also have a weaker absorption band at ~ 446 nm, assigned to a Fe^{II} d – d transition.[135] This band is not observed in the spectrum of the complex containing a longer oligothiophene group because of overlap from the strong, broad $\pi - \pi^*$ transition of the oligothiophene group.

Stable solutions of the oxidized species $\mathbf{68a}^+ - \mathbf{e}^+$ and $\mathbf{69a}^{2+} - \mathbf{e}^{2+}$ in CH_2Cl_2 containing 0.10 M $[(n\text{-Bu})_4N]PF_6$ are prepared by constant-potential electrolysis at a potential 0.25 V above $E_{1/2}$ of the ferrocenyl wave, except for **68e** which is electrolyzed 0.15 V above the iron-oxidation potential to preclude oxidation of the oligothiophene group. The UV–vis–near-IR spectra of these solutions are measured, and the data are collected in Table 13. All the complexes have a strong absorption band with λ_{max} between 285 and 425 nm, with a low-energy shoulder between 370 – 520 nm. The high-energy absorption band appears at a similar wavelength, and is of comparable intensity, to that observed in the corresponding neutral complex, and this band is therefore assigned as $\pi - \pi^*$ transitions in the oligothiophene groups. The shoulder observed between 370 and 520 nm is due to a Cp $\rightarrow$ Fe^{III} ligand-to-metal charge-transfer (LMCT) transition, and has been observed previously at similar energies in the oxidized species of **52** – **57** discussed in Chapter 2.

The spectra of $\mathbf{68a}^+ - \mathbf{e}^+$ and $\mathbf{69a}^{2+} - \mathbf{e}^{2+}$ all contain broad, low-energy absorption bands with λ_{max} between 875 and 1290 nm (Figures 28 and 29). These absorption bands are assigned to oligothiophene $\rightarrow$ Fe^{III} LMCT transitions. The energy maxima of these LMCT transitions correlate to the length of the oligothiophene groups, with the absorption maxima shifting to lower energy with increased conjugation. The ethylenedioxy substituent in

compounds with an identical conjugation length (for example **68c** vs **68e**) results in a shift to lower energy and an increase in the intensity of the absorption band.

Table 13. UV–vis–Near-IR Spectroscopic Data for $\mathbf{68a}^{+} - \mathbf{e}^{+}$ and $\mathbf{69a}^{2+} - \mathbf{e}^{2+}$

Complex	λ_{max} (nm) (± 5 nm) (ε ($M^{-1}cm^{-1}$))[a]	$\Delta\nu_{1/2}$ (cm^{-1})[b] ± 100	$f(\times 10^{-3})$[b] (cm^{-1})
$68a^{+}$	280 (18000), 370 (5000) (sh), 875 (630 ± 20)	3460	10 ± 2
$68b^{+}$	340 (22000), 445 (8800) (sh), 1015 (1390 ± 50)	3680	24 ± 2
$68c^{+}$	385 (26000), 485(11000) (sh), 1090 (1550 ± 70)	3800	27 ± 2
$68d^{+}$	285 (23000), 410 (56000) (sh), 995 (1190 ± 50)	3240	18 ± 2
$68e^{+}$	400 (28000), 505 (12000) (sh), 1290 (2090 ± 90)	3750	36 ± 2
$69a^{2+}$	285 (29000), 425 (12000) (sh), 885 (1550 ± 60)	3805	27 ± 2
$69b^{2+}$	375 (28000), 475 (19000), 1010 (2600 ± 100)	3890	46 ± 2
$69c^{2+}$	410 (33000) 475 (29000) (sh), 1080 (3600 ± 160)	3760	62 ± 3
$69d^{2+}$	290 (28000), 320 (24000) (sh), 450 (14000) (sh), 985 (2400 ± 90)	4120	46 ± 2
$69e^{2+}$	425 (30000), 520 (25000) (sh), 1255(4000 ± 150)	4300	79 ± 3

[a] CH_2Cl_2 containing 0.10 M $[(n\text{-}Bu)_4N]PF_6$, 20 °C. [b] lowest energy bands

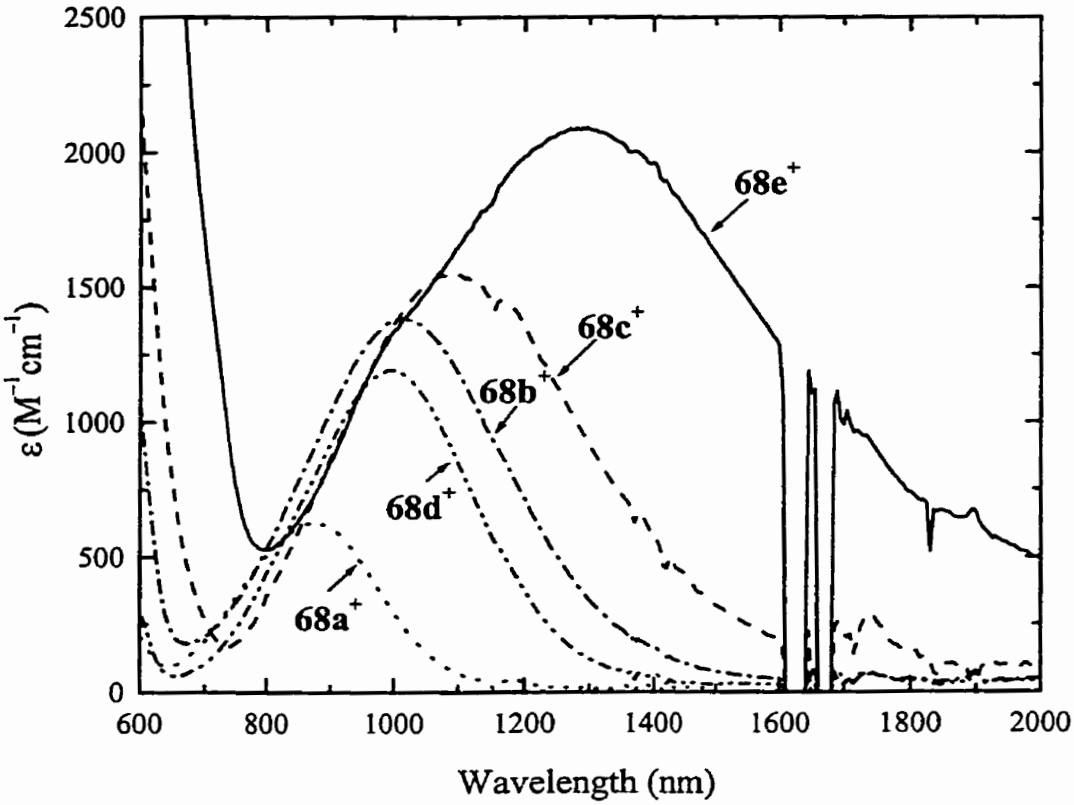

Figure 28. Vis–near-IR spectra of $\mathbf{68a}^{+} - \mathbf{e}^{+}$ in CH_2Cl_2 containing 0.1 M $[(n\text{-Bu})_4N]PF_6$.

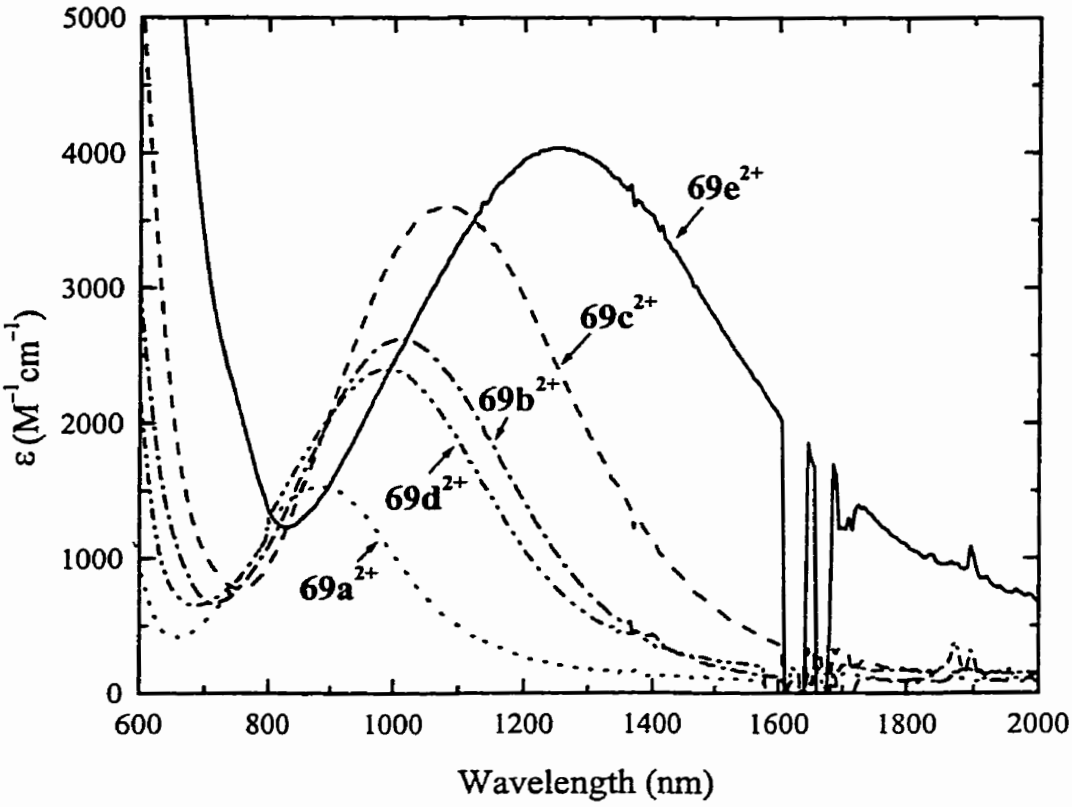

Figure 29. Vis–near-IR spectra of $\mathbf{69a}^{2+} - \mathbf{e}^{2+}$ in CH_2Cl_2 containing 0.1 M $[(n\text{-Bu})_4N]PF_6$.

4.4 Discussion

The electrochemical and spectroscopic results are interpreted using the classical electron-transfer model of Hush. The absorption maximum (ν_{max}) of an IVCT band has been related to the difference in electrochemical potentials (ΔE) between two metal centers (eqs 8 and 12). A similar relationship exists for the LMCT transition band in Ru^{III} complexes (eq 14).[36,155] Here D corrects for the difference between the $Ru^{II/III}$ potential with an oxidized

ligand attached and the measured $Ru^{II/III}$ oxidation potential, and χ is the sum of the inner and outer reorganizational parameters.

$$\nu_{max} = \chi_i + \chi_o + D + (e/h\,c)\Delta E \qquad (14)$$

A plot of ν_{max} vs ΔE will be linear if D and χ are constant for a series of complexes in which only the oxidation potential of the ligand varies. These data are shown for $\mathbf{68a}^{+} - \mathbf{68e}^{+}$ and $\mathbf{69a}^{2+} - \mathbf{69e}^{2+}$ in Figures 30 and 31, and in both plots the data are linearly correlated with R = 0.975 and 0.990 respectively. These correlations indicate that in both series a smaller oxidation-potential difference between the donor and the acceptor results in a lower optical-transition energy.

The extinction coefficient of the LMCT transition in the oxidized complexes clearly increases with smaller ΔE. Assuming a Gaussian-peak shape, the oscillator strength, f, of the band can be calculated from eq 6. A plot of f as a function of ΔE (Figure 32) shows a linear correlation within the series of monoferrocenyl cations, as well as within the diferrocenyl cations. The oscillator strengths of the dications are approximately twice those of the monocations due to the presence of twice the number of chromophores per molecule in the dications. From this plot it is clear that a smaller difference in oxidation potentials between donor and acceptor gives a greater charge-transfer transition oscillator strength.

The significance of the correlations observed in Figures 30 – 32 lies in the relationship between the intensity and shape of a charge-transfer band and the extent of charge delocalization. For a one-electron system, the f and ν_{max} of an absorption band are related to the charge-transfer dipole moment M by eq 15, which can be derived from eq 4.

$$M^2 = (9.22\times 10^{-12})\, e^2 f / \nu_{max}\, G \qquad (15)$$

From eq 15 and the correlations in Figures 30 – 32 it is clear that in the series of compounds studied here M^2 also correlates with ΔE. A smaller oxidation-potential difference between the donor and the acceptor results in a larger charge-transfer dipole moment. The dipole moment is related to α^2 and the transition dipole length d by eq 5.

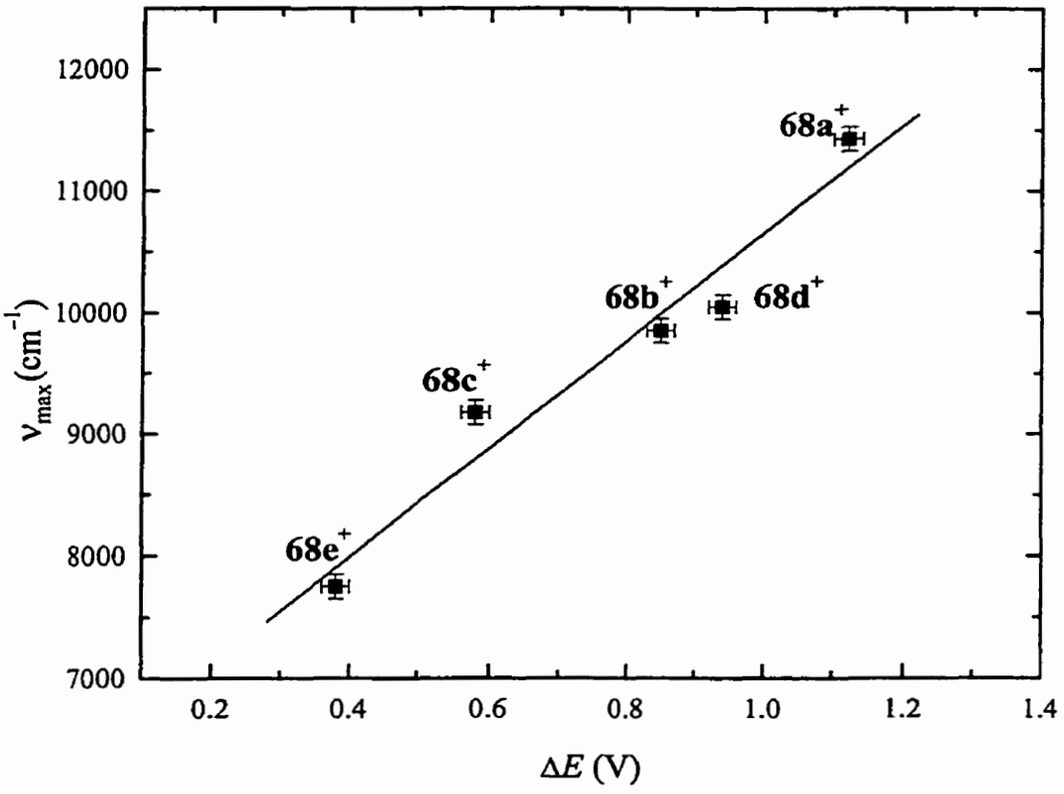

Figure 30. Absorption maxima ν_{max} (near-IR) vs the oxidation-potential difference $\Delta E = E_{p,a}(2) - E_{1/2}(1)$ for **68a**$^+$ – **e**$^+$.

From eq 5 it is clear that for complexes in which d is approximately the same, a larger dipole moment correlates to a larger α^2. Although the value of d is not known here, it is

reasonable that d does not vary significantly within the four pairs of complexes in the series with the same length oligothiophene group but with the different substitutents (for example **68a**$^{+}$ and **68d**$^{+}$, or **69c**$^{2+}$ and **69e**$^{2+}$). In these pairs, a direct correlation between α^2 and M^2, and therefore ΔE, can be made. In each pair, the complex with the smaller value of ΔE has the larger f and lower ν_{max} for the LMCT transition. Therefore, in each pair, a decrease in the oxidation-potential gap between donor and acceptor results in greater charge delocalization.

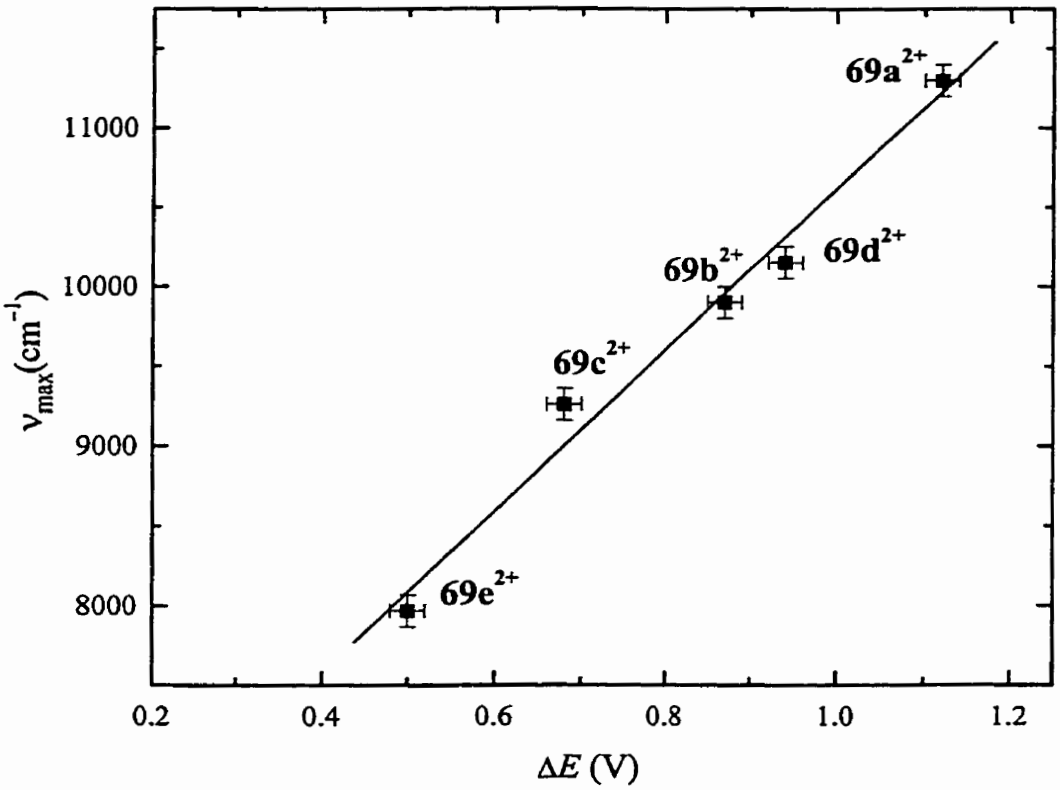

Figure 31. Absorption maxima ν_{max} (near-IR) vs the oxidation-potential difference $\Delta E = E_{p,a}(2) - E_{1/2}(1)$ for **69a**$^{2+}$ – **e**$^{2+}$.

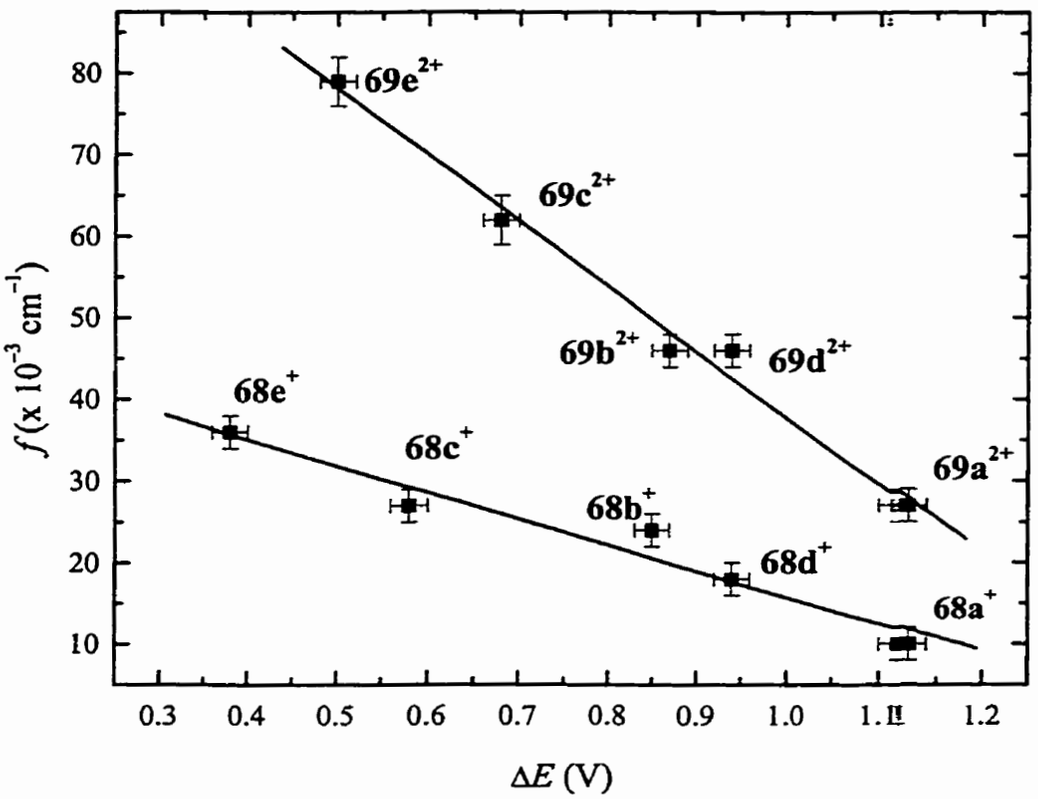

Figure 32. Oscillator strength f (near-IR) vs the oxidation-potential difference $\Delta E = E_{p,a}(2) - E_{1/2}(1)$ for $\mathbf{68a}^{+} - \mathbf{e}^{+}$ and $\mathbf{69a}^{2+} - \mathbf{e}^{2+}$.

As the conjugation length is increased (e.g. $\mathbf{68a}^{+} - \mathbf{c}^{+}$) the f increases, and the ν_{max} decreases, together giving a larger M^2 (eq 15). Here, it is reasonable that d is not the same for all the complexes, so only the *product* (M^2) of α^2 and d^2 increases with an increase in the length of the oligothiophene ligand. Thus, either more charge is delocalized (if d does not change significantly) or a similar amount of charge is delocalized further along the rigid oligothiophene ligand (if α^2 does not change significantly). Either situation is desirable for a

polymer in which charge is more delocalized. Choosing a longer oligothiophene bridge which has an oxidation potential closer to that of the metal group will either result in a greater extent of delocalization of charge, or in charge being delocalized over a greater length along the conjugated backbone.

4.5 Conclusions

Oxidation of the Fe^{II} centers in (ferrocenylethynyl)oligothiophene complexes results in the appearance of an LMCT transition from the oligothienyl group to the Fe^{III} center in the near-IR region. The band maxima and oscillator strengths of these low-energy transitions both correlate linearly with the difference ΔE in the oxidation potentials between the metal and oligothienyl groups. The complexes with similar charge-transfer transition dipole lengths show an increase in the extent of charge delocalization with a smaller ΔE. Comparisons between complexes with different length oligothienyl groups show that a reduction in ΔE results either in greater delocalization of charge or in charge being delocalized further along the rigid oligothienyl group.

The results described in this Chapter have important implications for the design of conjugated polymers which consist of redox-active metal and organic conjugated groups in the polymer backbone. It is clearly desirable to match the oxidation potentials of the metal and organic groups as closely as possible in order to achieve the highest degree of charge delocalization.

Chapter 5 Charge Delocalization in Oligothienylferrocene Monomers and Polymers

5.1 Introduction

The CV of 2,5-bis(ferrocenylethynyl)thiophene (**69a**) described in Chapter 4 shows no ground-state interaction between the two ferrocenyl termini; however, a similar study of 2,5-bisferrocenylthiophene shows two separated $Fe^{II/III}$ waves with a potential difference of 0.14 V, indicating significant ground-state interaction.[156] The presence of the C≡C group in **69a** appears to decrease the degree of charge delocalization relative to the complex without this group.

The results described in Chapter 4 show that charge delocalization in complexes containing metal centers linked via oligothienyl groups may be enhanced by matching the oxidation potentials of the metal and oligothienyl groups. Therefore, one approach to obtaining metal-oligothiophene polymers with extensive delocalization is to construct monomers containing two or more linked thienyl groups. Coupling between such monomers should yield oligomers or polymers containing bridges between adjacent metal centers of at least four thiophene units.

In this Chapter the preparation and electropolymerization of 1,1'-bis(5-(2,2'-bithienyl))ferrocene (**50**) and 1,1'-bis(5-(2,2':5',2"-terthienyl))ferrocene (**73**), and the spectroscopic and electrochemical characterization of these compounds and electropolymerized films are described. Higgins and coworkers have also published a similar study while this thesis is in preparation.[117]

5.2 Experimental

General. Procedures were as described in previous Chapters except as noted here. TMEDA was purified by distillation from KOH and was stored over molecular sieves (4 Å). 1,1'-Bis(2-thienyl)ferrocene (**40**) was prepared using the literature procedure.[69,157]

1,1'-Bis(5-(2,2'-bithienyl))ferrocene (50). *n*-BuLi (3.5 mL, 1.6 M in hexanes, 5.6 mmol) was added via syringe at 0 °C to a solution of **40** (0.78 g, 2.3 mmol) and TMEDA (1.2 mL, 8.0 mmol) in a mixture of dry THF (20 mL) and hexanes (10 mL). The solution was heated at reflux for 2 h, then cooled to room temperature. A solution of anhydrous $ZnCl_2$ (0.76 g, 0.56 mmol) in dry THF (20 mL) was then added via cannula, and the mixture was stirred for another 2 h. The mixture was added to a solution of 2-bromothiophene (0.86 g, 5.3 mmol) and $Pd(PPh_3)_4$ (60 mg, 0.052 mmol) in dry THF (20 mL) via cannula, and the mixture was heated at 50 °C for 2 days while the solution was stirred. After the reaction mixture was cooled down to room temperature, a solution of 1 M aq HCl (30 mL) was added to the reaction solution. The organic layer was collected, and the aqueous layer was extracted using methylene chloride (2 × 20 mL). The organic portions were combined and washed with distilled water (2 × 30 mL). The organic solution was dried over anhydrous $MgSO_4$, and collected by filtration. Removal of the solvent yielded a brownish red solid, which was purified by flash chromatography on silica gel using hexanes/CH_2Cl_2 (3:2 v/v) as eluant. Pure **50** was also obtained by crystallization from the hexanes/CH_2Cl_2 solution at –4 °C overnight. Yield: 0.39 g (34%). ^{1}H NMR (400 MHz, $CDCl_3$): δ 7.15 (dd, J = 5.0, 1.0 Hz, 2H), 7.05 (dd, J = 3.5, 1.0 Hz, 2H), 6.96 (dd, J = 5.0, 3.5 Hz, 2H), 6.87 (d, J = 3.7 Hz, 2H), 6.73 (d, J = 3.7 Hz, 2H), 4.47 (t, J = 1.8 Hz, 4H), 4.24 (t, J = 1.8 Hz, 4H). Anal. Calcd $C_{26}H_{18}S_4Fe$: C 60.69, H 3.53. Found: C 60.74, H 3.42.

1,1'-Bis(5-(2,2':5',2"-terthienyl))ferrocene (73). This complex was prepared as described for **50** using 5-bromo-(2,2'-bithiophene). The product was obtained in > 95% purity by crystallization either from hot toluene or chlorobenzene solution. Yield: 53%. ^{1}H NMR (400 MHz, $CDCl_3$): δ 6.98 (s, broad, 2H), 6.95 (dd, J = 3.6, 1.1 Hz, 2H), 6.80 – 6.83(m, 2H), 6.78 (d, J = 3.7, 2H), 6.71 (dd, J = 5.1, 1.1 Hz, 2H), 6.63 (dd, J = 5.1, 3.6 Hz, 2H), 6.53 (d, J = 3.7 Hz, 2H), 4.37 (t, J = 1.8 Hz, 4H), 4.01 (t, J = 1.8 Hz, 4H). Anal. Calcd $C_{34}H_{22}S_6Fe$: C 60.16, H 3.27. Found: C 60.20, H 3.15.

Electrochemistry. The working electrode was a Pt disc electrode with a diameter of 1.0 mm. All electrochemical polymerizations were carried out under nitrogen, and the cells containing the electrodes and $[(n\text{-Bu})_4]NPF_6$ were dried *in vacuo* at 90 °C overnight before addition of dry solvent. The polymer film was grown on the electrode surface by scanning over a suitable potential range (0 – 1.5 V vs SCE for **50**, and 0 – 1.2 V vs SCE for **73**). The electrochemical polymerization of **50** was carried out at 20 °C in a CH_2Cl_2 solution with an electrolyte concentration of 0.6 M, and the complex concentration was in a range of 5×10^{-3} – 1×10^{-2} M. The same experiments for **73** were carried out with a saturated solution of **73** in 1,2-dichloroethane with 0.6 M electrolyte at 70 °C.

Spectroelectrochemistry. A homemade spectroelectrochemical cell using a Pyrex cuvette into which an ITO working electrode could be inserted under inert atmosphere was used. The polymer films were deposited on the ITO electrodes from the same deposition solutions as used with the Pt electrodes, by scanning at 25 mV/s over a similar potential range (0 – 1.7 V vs SCE for **50**, and –0.2 – 1.3 V vs SCE for **73**). The poly-**50** film was prepared at 20 °C, and the poly-**73** film at 55 °C. After the film was reduced at 0 V, the films were removed from the solution, rinsed with CH_2Cl_2 and dried *in vacuo* for 1 h. The film-coated

electrodes were then loaded into the previously dried cell containing $[(n\text{-Bu})_4]NPF_6$, along with a Pt counter electrode and Ag wire reference electrode. The cell was dried *in vacuo* overnight at room temperature, and dry CH_2Cl_2 was added until the electrolyte concentration was 1.3 M. The vis–near-IR spectrum was obtained at 20 °C after the film was held at a specific potential until no further change in current was observed (~ 1 min), to allow the entire film to reach the potential.

5.3 Results and Discussion

5.3.1 Syntheses

Complexes **50** and **73** are synthesized by the coupling of **40** with 2-bromothiophene and 5-bromo-2,2'-bithiophene respectively (Scheme 18). Complex **40** has been previously synthesized,[69] while **50** and **73** are new compounds. Complex **50** is obtained as an orange solid which is soluble in CH_2Cl_2 and is purified by chromatography on silica gel. The solubility of **73** at room temperature in most organic solvents is poor; however, its solubility increases at slightly elevated temperatures so it can be purified by recrystallization from hot toluene or chlorobenzene.

Scheme 18

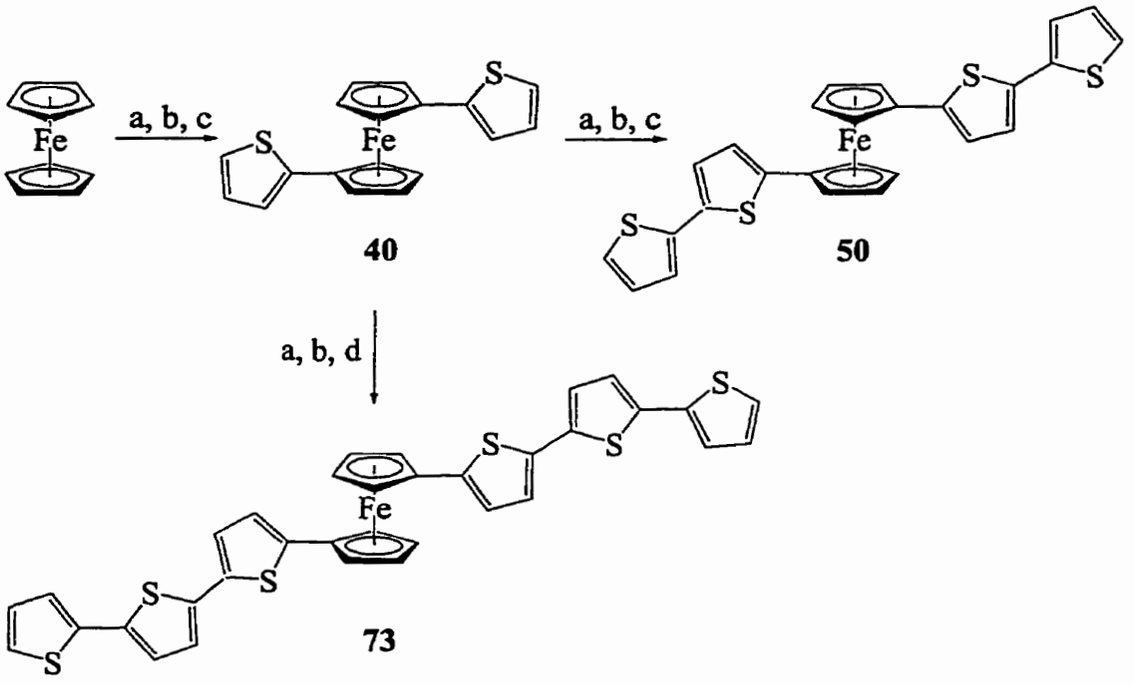

Reagents: (a) BuLi, TMEDA, THF/hexanes. (b) $ZnCl_2$, THF. (c) 2-bromothiophene, $Pd(PPh_3)_4$, THF. (d) 5-bromo-2,2'-bithiophene, $Pd(PPh_3)_4$, THF.

5.3.2 Electrochemistry

Complexes **40**, **50** and **73** are expected to show electroactivity both due to the $Fe^{II/III}$ couple and the thiophene groups, and the CV results are collected in Table 14. The CV of **40** at 20 °C in CH_2Cl_2 containing 0.1 M $[(n\text{-}Bu)_4N]PF_6$ shows only one reversible oxidation wave with $E_{1/2}$ = 0.46 V vs SCE, due to the $Fe^{II/III}$ redox couple. Previous attempts by others to electropolymerize this monomer are also unsuccessful.[117,157] The CV of **50** at 20 °C in CH_2Cl_2 containing 0.6 M $[(n\text{-}Bu)_4N]PF_6$ contains two oxidation waves in the range 0 – 1.5 V vs SCE. The lower potential wave with $E_{1/2}$ = 0.45 V vs SCE is reversible and assigned to the $Fe^{II/III}$ redox couple (Figure 33a). The higher potential wave at 1.33 V vs SCE is

electrochemically irreversible and is coupled to a reduction feature at 1.05 V (Figure 33b); this wave is assigned to a thiophene-based oxidation. Similar electrochemical behavior has been observed in a series of [CpRu(η^5-oligothiophene)]PF_6 complexes.[158] In the absence of water, scanning several times over the potential range 0 to 1.5 V results in the appearance of an electrochromic film on the electrode surface. The film is golden-red and stable in the neutral state, but becomes black when oxidized. Scanning from 0 to 0.7 V, where only the ferrocenyl groups are oxidized, does not result in any deposition.

The CV of the electropolymerization process (Figure 33b) is consistent with the growth of a conducting film on the electrode since the current of both the ferrocenyl-oxidation wave and a new reduction wave at 0.8 V increases with scan number. Oxidative coupling of **50** results in a polymer (poly-**50**) which contains ferrocenyl groups linked by tetrathienyl bridges, and deposits on the electrode due to poor solubility. The new reduction wave is associated with the tetrathienyl groups, and is expected to occur at a lower potential than reduction of the bithienyl group due to more extended conjugation.[21]

The CV of the poly-**50** film in monomer-free solution shows a broad oxidation wave at 0.6 V which is assigned as the $Fe^{II/III}$ oxidation (Figure 34). The associated reduction at 0.35 V is sharper, but is approximately equal in area to the oxidation wave. The CV also shows a broad feature at higher potentials which is due to oxidation of coupled oligothiophene moieties in the film. The film is stable to repeated cycling over the potential range 0 to 0.8 V, with only slight changes in the voltammogram during this process.

Table 14. UV–vis–near-IR Spectroscopic and Electrochemical Data for **40**, **50** and **73**

Complex	UV–vis–near-IR	$E_{1/2}$ (1)[b]	$E_{p,a}$ (2)[b]
	λ (nm) (ε ($M^{-1}cm^{-1}$))[a]	V vs SCE	V vs SCE
40	460 (830), 306 (17000)	0.46	-
50	466 (2800, sh), 344 (35000)	0.45	1.33
73	384 (55000)	0.37	0.93
2,2′-bithiophene[c]	302 (12470)	-	1.31
2,2':5',2"-terthiophene[c]	355 (25050)	-	1.05
40$^+$	275 (18000), 365 (9000), 480 (3800), 815 (900, sh), 945 (1200)		
50$^+$	345 (21000), 450 (9600), 560 (3700, sh), 1175 (2300)		
73$^+$	385 (51000), 505 (13000, sh), 585 (7800, sh), 1305 (3500)		

[a] CH_2Cl_2, 20 °C. [b] Conditions: Pt working electrode; 20 °C; CH_2Cl_2; scan rate = 50 mV/s, except for **73**: 70 °C; $ClCH_2CH_2Cl$. [c] UV–vis: ref. [14]; electrochemical: ref. [21]

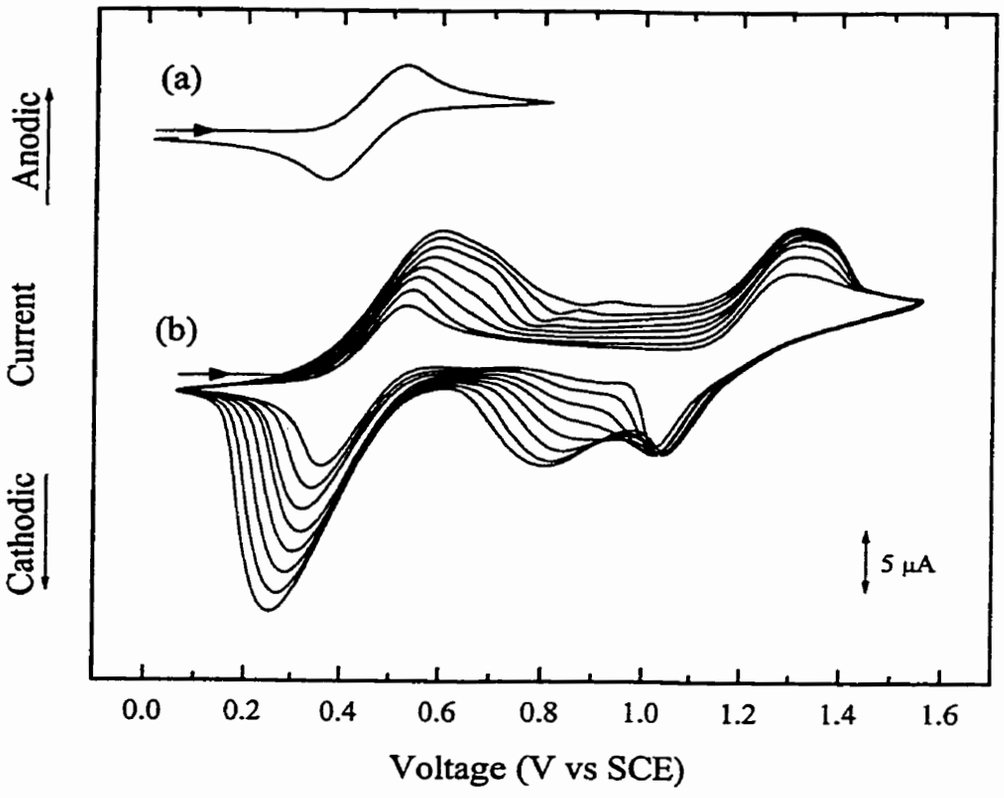

Figure 33. Cyclic voltammogram of **50** at 20 °C in CH_2Cl_2 containing 0.6 M $[(n\text{-}Bu)_4N]PF_6$ on a Pt working electrode (a) between 0 – 0.8 V and (b) multiple scans between 0 – 1.6 V. Scan rate = 50 mV/s.

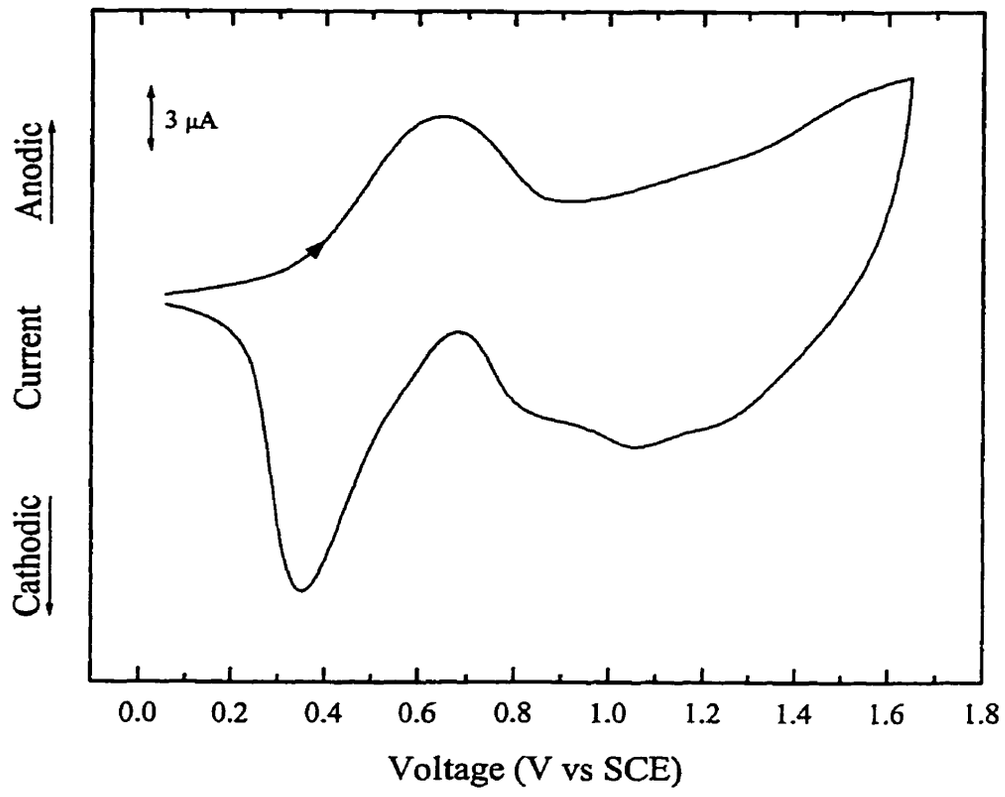

Figure 34. Cyclic voltammogram of poly-**50** on a Pt working electrode at 20 °C in CH_2Cl_2 containing 0.6 M $[(n\text{-Bu})_4N]PF_6$. Scan rate = 50 mV/s.

Due to the poor solubility of **73** in CH_2Cl_2 at room temperature the cyclic voltammogram of this compound is obtained in $ClCH_2CH_2Cl$ containing 0.6 M $[(n\text{-Bu})_4N]PF_6$ at 70 °C. The cyclic voltammogram contains multiple waves in the range 0 – 1.2 V vs SCE, including a reversible $Fe^{II/III}$ wave with $E_{1/2}$ = 0.37 V (Figure 35a), and two irreversible waves at 0.93 and 1.03 V due to thiophene-based oxidations. The $Fe^{II/III}$ waves of **40**, **50** and **73** all appear at very similar potentials, indicating that those redox couples are not substantially

affected by the length of the oligothiophene group. Similar behavior is also observed in **62a – c** and **63a – c**. Increasing the length of the oligothienyl group from **50** to **73** results in a decrease in the second-oxidation potential by 0.40 V.

In the absence of water, scanning over the potential range 0 to 1.2 V results in the growth of a golden-red film (poly-**73**) on the electrode surface (Figure 35b). The CV of the film in monomer-free solution shows similar features to those observed for poly-**50** (Figure 34). This cyclic voltammogram (Figure 36) is recorded after the film is scanned ten times over the complete potential range. During these scans the intensity of the waves increase until it stabilizes as shown in Figure 36. After this treatment, the film is stable to repeated cycling over the potential range 0 to 1.5 V. The reasons for this unusual increase in intensity are not known.

The thicknesses of the poly-**50** and poly-**73** films are estimated from integration of the cyclic voltammograms. The number of monomer units in the films is determined from the area under the ferrocenyl-redox waves. Assuming a density of 1.1 g/cm^3,[10] the same as that of electropolymerized polythiophene, the poly-**50** film in Figure 34 and the poly-**73** film in Figure 36 both have a thickness of 0.4 μm.

It is very important that electropolymerization of **50** and **73** be carried out under rigorous exclusion of water. The presence of even small amounts of water results in the formation of brittle black deposits which stop growing after 2 – 3 scans. The $Fe^{II/III}$ wave disappears after the first scan, which suggests that water reacts to form an insulating film which prevents the $Fe^{II/III}$ redox couple in dissolved monomer from being observed. In a related study, Higgins and coworkers have also attempted to electropolymerize **50** and **51**, and have obtained films in which the ferrocenyl groups are electrochemically inaccessible.[117]

This different result is likely related to the amount of water present in the electropolymerization media.

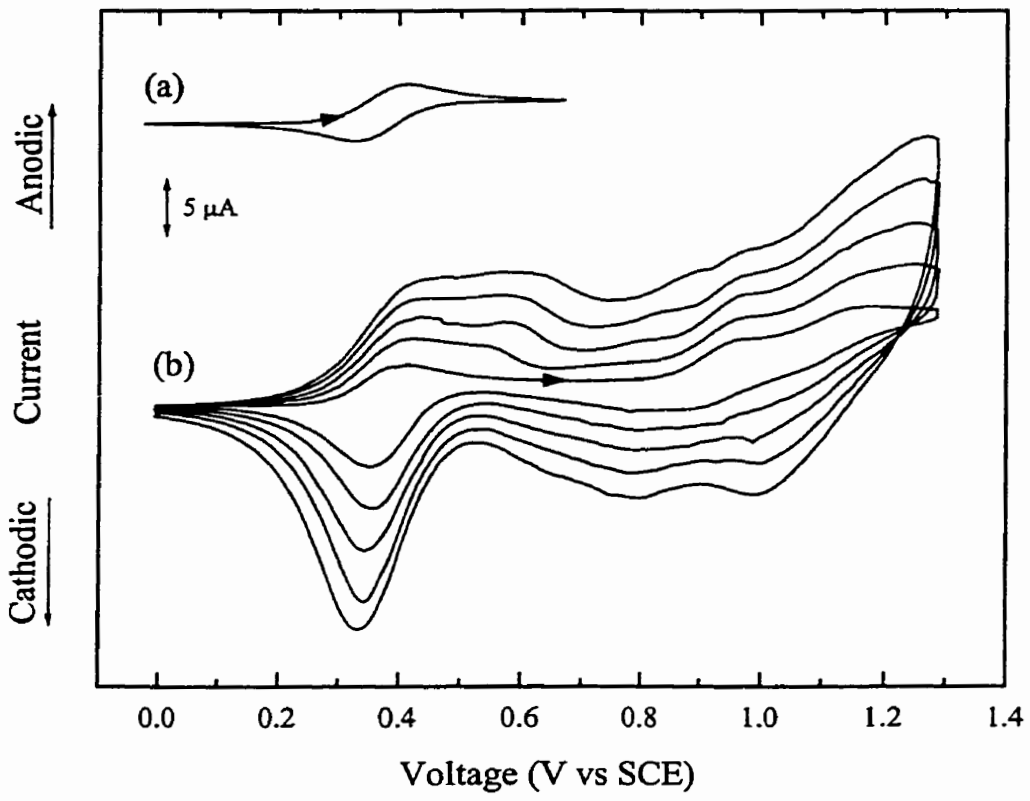

Figure 35. Cyclic voltammogram of **73** at 70 °C in $ClCH_2CH_2Cl$ containing 0.6 M [(*n*-Bu)$_4$N]PF_6 at a Pt working electrode (a) between 0 – 0.7 V and (b) multiple scans between 0 – 1.3 V. Scan rate = 50 mV/s.

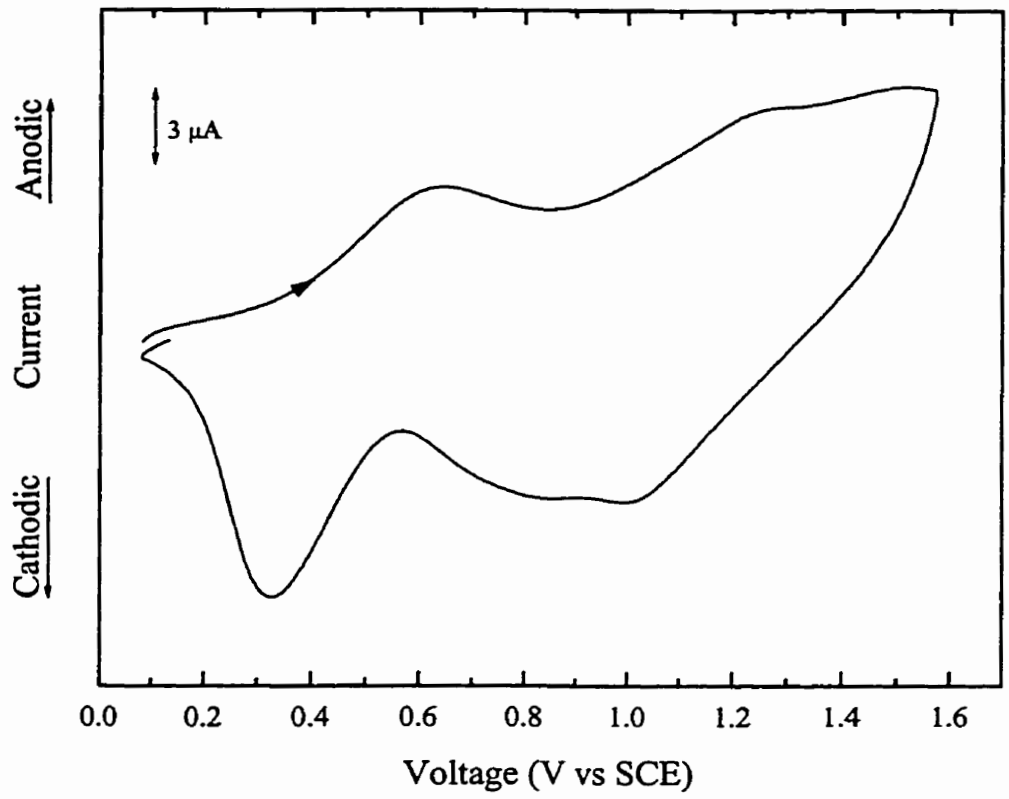

Figure 36. Cyclic voltammogram of poly-**73** on a Pt working electrode at 20 °C in CH_2Cl_2 containing 0.6 M $[(n\text{-Bu})_4N]PF_6$. Scan rate = 50 mV/s.

5.3.3 Spectroscopic Characterization

The spectroscopic data of both the neutral complexes and the monocations are collected in Table 14. The UV–vis spectra of **40, 50** and **73** in the neutral state contain a strong absorption band assigned to a $\pi - \pi^*$ transition in the oligothienyl group. This band shifts to lower energy and becomes more intense as the conjugation length is increased. The weaker bands at 460 nm in the spectrum of **40** and the shoulder at 466 nm for **50** are assigned

as Fe^{II} d – d transitions, and appear very close to the ligand-field transition for ferrocene at 441 nm.[135] Solutions of the monocations **40**$^+$, **50**$^+$, and **73**$^+$ are prepared by electrochemical oxidation in CH_2Cl_2 containing 0.13 M $[(n\text{-Bu})_4N]PF_6$, and the vis–near-IR spectra are obtained (Figure 37). The spectra all contain several intense transitions between 300 – 800 nm, and the strongest ones are assigned to $\pi - \pi^*$ transitions in the oligothienyl groups. These transitions appear at similar energy and have similar intensity to those of the corresponding neutral complexes. The other bands between 300 – 800 nm are likely due to Cp → Fe^{III} LMCT transitions and are of similar intensity and energy as those in ferrocenium.[153]

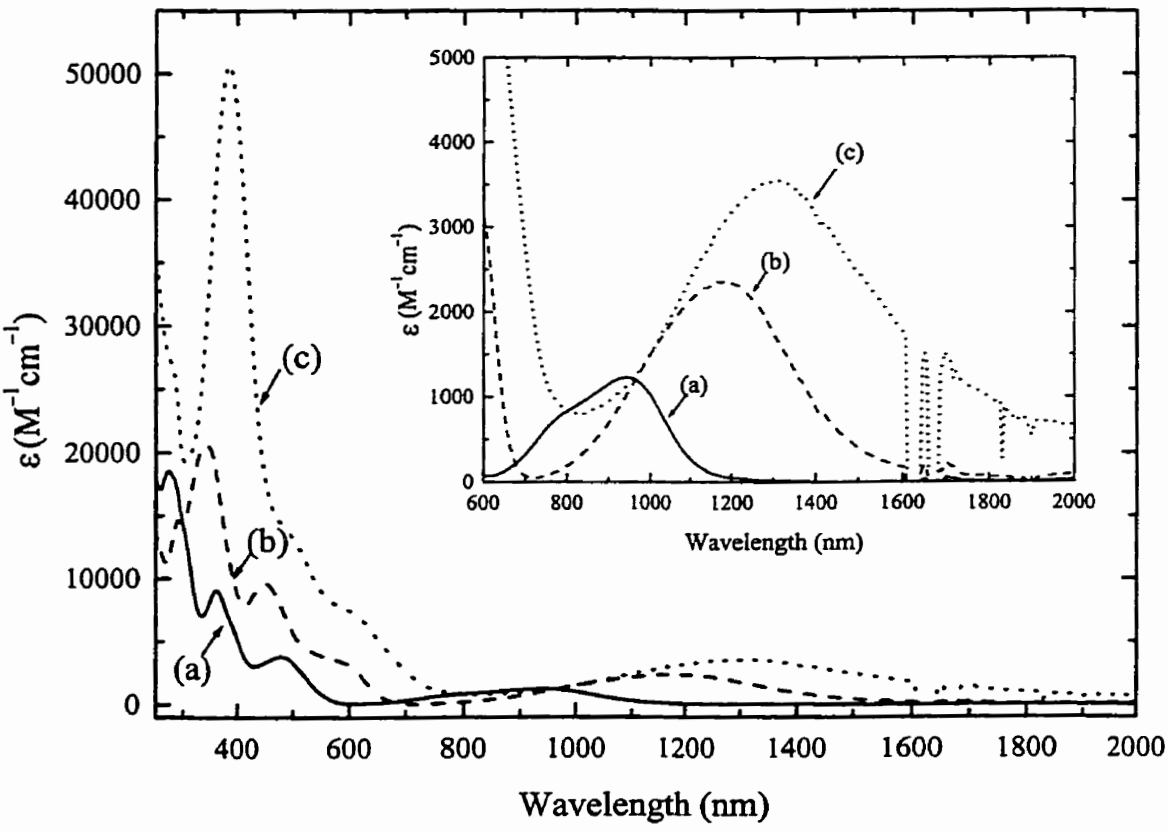

Figure 37. Vis–near-IR spectra of (a) **40**$^+$, (b) **50**$^+$ and (c) **73**$^+$ in CH_2Cl_2 containing 0.13 M $[(n\text{-Bu})_4N]PF_6$.

The spectra of **40**$^+$, **50**$^+$ and **73**$^+$ contain a broad low-energy band with λ_{max} between 945 and 1305 nm having features very similar to those observed in the complexes described in Chapter 4. The absorption maximum and intensity of this band are dependent on the length of the conjugation in the ligand. The band appears at the highest energy (945 nm) and is the least intense (ε = 1200 $M^{-1}cm^{-1}$) for **40**$^+$, and appears at the lowest energy (1345 nm) and is the most intense (ε = 3500 $M^{-1}cm^{-1}$) for **73**$^+$. On the basis of this behavior, this low-energy band is assigned to an oligothiophene $\rightarrow$ Fe^{III} LMCT transition. The difference in oxidation potential between the oligothienyl group and the metal center correlates to the energy of this LMCT transition, as well as to the oscillator strength (f = 2.1 $\times$ 10^{-2} cm^{-1} for **40**$^+$, 3.3 $\times$ 10^{-2} cm^{-1} for **50**$^+$ and 5.5 $\times$ 10^{-2} cm^{-1} for **73**$^+$). Increased conjugation in the oligothienyl group narrows the oxidation potential difference between the metal and the oligothienyl group, and thus enhances donor-accepting coupling between them. The energy and intensity of the LMCT transition in **40**$^+$, **50**$^+$ and **73**$^+$ are consistent with significant delocalization of charge in these complexes, and this delocalization is the greatest for the complex with the most conjugated oligothienyl group (**73**$^+$).

5.3.4 Spectroelectrochemistry of Electropolymerized Films

In order to examine the effect of oxidation on the spectral characteristics of the electropolymerized films, *in situ* spectroelectrochemistry on poly-**50** and poly-**73** films on transparent indium tin oxide (ITO) electrodes is carried out. The cyclic voltammograms of these films are similar to those obtained on Pt electrodes, although the positions of all the peaks slightly shift due to the resistance of the ITO layer. In order to minimize IR drop in the

solution due to the relatively large separations between the electrodes in the spectroelectrochemical cell, high electrolyte concentrations are used (1.3 M).

Optical spectra of the films are collected at three potentials: reduced (~ –0.1 – 0 V), with the ferrocene oxidized (~ 0.7 – 0.8 V) and fully oxidized (~ 1.5 – 1.7 V). These spectra over the range 300 – 1600 nm are shown for poly-**50** and poly-**73**, respectively, in Figures 38 and 39. The spectra all show sharp absorptions at > 1100 nm due to vibrational overtones from the electrolyte and solvent. The reduced films (~ –0.1 – 0 V vs SCE) have a single broad band at 445 nm (poly-**50**) and 420 (poly-**73**) which are assigned to a $\pi - \pi^*$ transition of the oligothienyl group in the backbone. The absorption maxima for both films are close to those observed for polythiophene (between 418 – 480 nm depending on the method of preparation). The absorption maximum for poly-**73** is expected at lower energy than for poly-**50** due to the relative conjugation lengths in the two materials; however, the opposite is observed. This may be due to differences in the conditions (temperature and solvent) under which the two films are prepared. The conductivity of electropolymerized polythiophene films has been shown to be dependent on the conditions under which the films are prepared;[159] similar effects may influence the absorption maxima for the neutral poly-**50** and poly-**73** films.

Upon oxidation of the films to a potential at which the ferrocenyl groups are oxidized several changes are observed in the spectra. In the case of poly-**50** two bands are observed, at 495 and 1395 nm. The broad, higher energy band is predominantly due to the $\pi - \pi^*$ transition with contributions from Cp $\rightarrow$ Fe^{III} LMCT also possible, and the band with λ_{max} at 1395 nm is assigned as a charge-transfer band from the oligothiophene group to the Fe^{III}. It is interesting to compare this spectrum to that of **50**$^+$ in solution (Figure 37b). The lowest energy band shifts from 1175 nm in **50**$^+$ to 1395 nm in poly-**50** oxidized at 0.8 V, consistent with the

charge transfer originating from a more conjugated moiety in the polymer. Coupling of **50** should result in a tetrathienyl bridge between ferrocenyl groups, which is expected to result in a charge-transfer band slightly lower in energy than that observed for $\mathbf{73}^{+}$ which contains a terthienyl group.

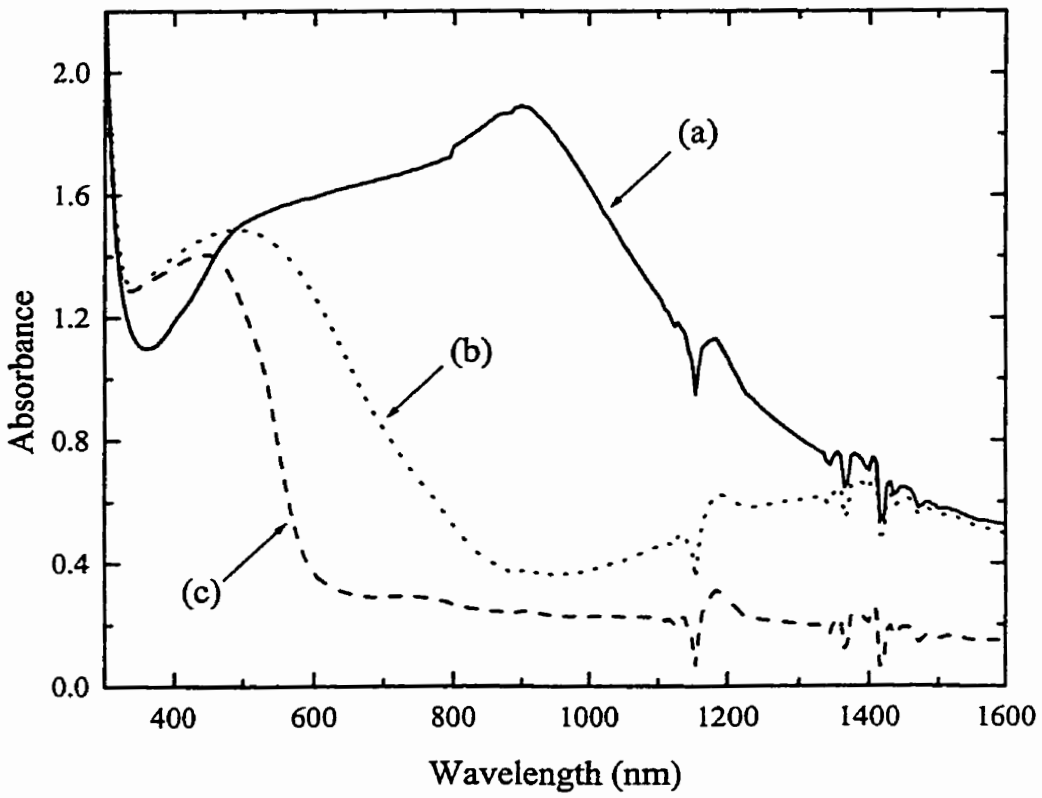

Figure 38. Spectroelectrochemistry of poly-**50** on an ITO electrode at the oxidation potentials (a) –0.1 V, (b) 0.8 V and (c) 1.7 V vs SCE in CH_2Cl_2 containing 1.3 M $[(n\text{-}Bu)_4N]PF_6$.

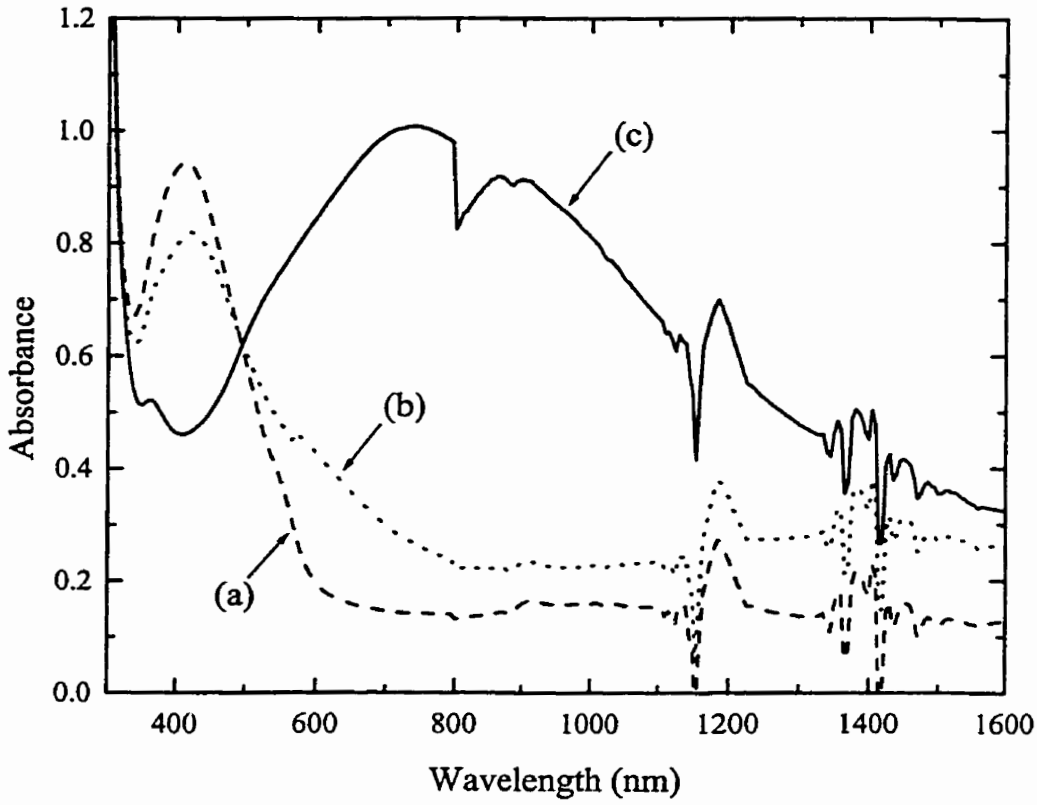

Figure 39. Spectroelectrochemistry of poly-**73** on an ITO electrode at the oxidation potentials (a) 0 V, (b) 0.7 V and (c) 1.5 V vs SCE in CH_2Cl_2 containing 1.3 M $[(n\text{-}Bu)_4N]PF_6$.

In the spectrum of poly-**73** oxidized at 0.7 V, the $\pi - \pi^*$ transition does not shift substantially from neutral poly-**73**, although a broad low-energy shoulder does appear, and a very weak, broad band in the near-IR is present. Based on the spectra of $\mathbf{50}^+$ and $\mathbf{73}^+$, as well as the spectrum of poly-**50** at 0.8 V, this absorption of poly-**73** at 0.7 V is expected to be more intense than observed. It is possible that the ferrocenyl centers are not completely oxidized at 0.7 V resulting in a weaker absorption. Cycling the films twice between 0 and 0.7 – 0.8 V

demonstrates that the spectral changes are completely reversible, consistent with the stability of the films over this potential range as shown in the cyclic voltammograms of the films on the Pt electrodes.

Oxidation of both poly-**50** and poly-**73** films to 1.5 – 1.7 V vs SCE results in dramatic changes in the spectra. For both poly-**50** and poly-**73** a very broad absorption between 400 and 1600 nm appears. In contrast to the reversibility of the spectral changes upon oxidation to 0.7 – 0.8 V, these broad absorptions do not completely disappear when the oxidized film is reduced back to –0.1 – 0 V indicating oxidation to 1.5 – 1.7 V results in some irreversible changes to the polymers. The appearance and positions of these broad bands suggest that they arise due to transitions to intergap states in the oxidized polymers. Oxidation or doping of polythiophene causes the interband absorption at 480 nm to decrease with the concomitant appearance of lower energy bands due to transitions between the valence band and localized levels in the band gap.[160]

5.4 Conclusions

The stability of ferrocene in both Fe^{II} and Fe^{III} oxidation states allows for the electropolymerization of oligothienylferrocene complexes without significant decomposition. The growth of electroactive films on the electrode surface is consistent with the formation of a conductive material during the electropolymerization process. The reversible electrochromic behavior of these films is similar to that observed for other conducting polymers such as polythiophene.

Oxidation of the ferrocenyl groups in both the monomers and in the electropolymerized films results in the appearance of a low-energy transition. This band is

due to an oligothienyl group to Fe^{III} LMCT transition and is indicative of significant charge delocalization, which is enhanced with increased conjugation in the oligothienyl group.

Chapter 6 Copper(I) Halide Catalyzed Trans – Cis Isomerization of $RuCl_2(dppm)_2$

6.1 Introduction

Coupling reactions of ruthenium halide complexes with organostannane derivatives in the presence of a copper(I) halide are an important synthetic route to ruthenium-containing conjugated polymers.[64,71,80,82] This route has been successfully used for the preparations of new complexes described in Chapters 2 and 3. In one of these syntheses the amount of copper(I) halide used results in different products. *trans*-$Ru(dppm)_2(C{\equiv}CFc)_2$ (**53**) is obtained from the coupling reaction of $Ru(dppm)_2Cl_2$ with $FcC{\equiv}CSn(n\text{-}Bu)_3$ when catalytic CuI is used, while [*cis*-$Ru(dppm)_2(C{\equiv}CFc)_2$]CuI (**52**) is isolated when excess CuI is used.

The function of CuI in these coupling reactions is not very well understood, although it is likely that transmetalation of the acetylide group from $RC{\equiv}CSnR'_3$ (R' = Bu, Me) to CuI is involved in the catalysis. This is related to the use of copper(I) compounds as cocatalysts in Stille reactions, in which organic electrophiles are coupled with organostannanes using Pd(0) catalysts.[161,162] Besides the transmetalation, the copper(I) halide likely also plays another role in the coupling reactions which influences the structure of the product as described above for **52** and **53**. In order to investigate this question, the reactivity of CuCl or CuI with *trans*-$RuCl_2(dppm)_2$ (**19**) or *cis*-$RuCl_2(dppm)_2$ (**59**) is examined. Meyer has previously reported that the isomerization of **59** to **19** occurs by photochemical means or by oxidation and subsequent reduction, and that the reverse process (**19** → **59**) occurs thermally in 1,2-dichloroethane at reflux (83 °C) in 10 h.[120] In this Chapter the catalytic behavior of CuCl and CuI for the isomerization of **19** to **59** is described, as well as the isolation and structural characterization of

a halide-bridged heterotrimetallic complex **74** that forms when **19** or **59** reacts with excess CuCl.

6.2 Experimental

Copper(I) halide catalyzed conversion of 19 to 59. CuCl (0.7 mg, 0.007 mmol, 8 mol %) was added to a solution of **19** (87 mg, 0.093 mmol) dissolved in CH_2Cl_2 (20 mL). The solution was stirred for 24 h at room temperature in the dark, during which time the solution turned bright greenish yellow. The solution was then washed with with 2 M aq HCl and distilled water to remove residual copper salts. The CH_2Cl_2 layer was collected and dried over $MgSO_4$. The solution was reduced in volume to approximately 2 mL and was then poured into hexanes (50 mL) to offord 74 mg of a yellow powder, which was 95% **59** and 5% **19**. Pure **59** was obtained when the reaction was allowed to proceed for 6 days. When CuI was used as the catalyst under identical conditions, the same results were obtained.

[{*cis*-RuCl$_2$(dppm)$_2$}$_2$Cu][CuCl$_2$] (74). CuCl (17 mg, 0.17 mmol) was added to a solution of **19** (296 mg, 0.10 mmol) in CH_2Cl_2 (20 mL). The suspension was stirred at room temperature for 2 h, during which time it turned from orange-yellow to green-yellow. The solution was filtered through Celite 545, and the filtrate was reduced in volume to approximately 2 mL. The concentrated solution was poured into hexanes (100 mL), yielding a yellow powder. The solid was recrystallized from layered CH_2Cl_2/hexanes to obtain yellow needles, which were dried at 90 °C *in vacuo* for 2 days. Yield: 94 mg (89%). Anal. Calcd for $C_{100}H_{88}Cl_6P_8Cu_2Ru_2$: C 57.70; H 4.26. Found: C 57.79; H 4.13.

Crystallographic Study. Data collection and structure determination were carried out by Dr. Glenn Yap (Department of Chemistry and Biochemistry, University of Windsor,

Ontario). A suitable single crystal of **74**, grown by slow diffusion of hexanes into a 1,2-dichloroethane solution, was selected and mounted inside a thin-walled glass capillary which contained mother liquor. Unit-cell parameters were calculated from reflections obtained from 60 data frames collected at different sections of the Ewald sphere. The systematic absences in the diffraction data and the determined unit-cell parameters were consistent for space groups *P2/c* and *Pc*. The E statistics strongly suggested the centric option, which yielded chemically reasonable and computationally stable results. A trial application of a semiempirical absorption correction based on redundant data at varying effective azimuthal angles yielded T_{max}/T_{min} at unity and was ignored.

Table 15. Crystallographic Data for **74**·solvent

Empirical formula	$C_{107.13}H_{88}Cl_6Cu_2P_8Ru_2$	*V*, Å3	5787.0(3)
Formula weight	2165.02	T, K	298 (2)
Crystal system	Monoclinic	Radiation	MoKα (0.71073 Å)
Space group	*P2/c*	Density (calcd)	1.242 g cm^{-3}
a, Å	11.6059(4)	*Z*	2
b, Å	13.8415(5)	*R(F)*,[a] %	5.38
c, Å	36.163(1)	*Rw(F2)*,[a] %	16.47
β, deg	95.03(1)	GOF on F^2	1.066

[a] Quantity minimized = $Rw(F^2) = \Sigma[w(F_o^2 - F_c^2)^2]$; $R = \Sigma|F_o - F_c|/\Sigma(F_o)$; GOF = Goodness-of-fit.

The $[\{cis\text{-}RuCl_2(dppm)_2\}_2Cu]^+$ cation is located on a 2-fold axis. A $[CuCl_2]^-$ anion is located at an inversion center. Attempts to model several peaks of significant electron density, located away from the compound molecules, as a chemically recognizable, cocrystallized

solvent molecule were not successful. These peaks were assigned arbitrary carbon atom identities with refined partial site occupancies. All non-hydrogen atoms were refined with anisotropic displacement coefficients except those on the apparent solvent molecules, which were refined isotropically. Phenyl groups were refined as idealized, flat, rigid bodies. All hydrogen atoms were treated as idealized contributions except those on the apparent solvent molecules, which were ignored. The structure was solved by direct methods, completed by subsequent Fourier syntheses, and refined with full-matrix least-squares methods. All scattering factors and anomalous dispersion coefficients are contained in the SHELXTL 5.03 program library.[123] Table 15 contains the details of the structure determination.

6.3 Results and Interpretation

6.3.1 Catalytic Isomerization

When a solution of **19** in CH_2Cl_2 is stirred in the presence of CuCl or CuI (5 – 10 mol %) at room temperature for 24 h, **59** forms in high yield (90 – 95%) (Scheme 19). If the reaction is allowed to proceed for 6 days at room temperature in the absence of light, **19** is quantitatively converted to **59**. No **59** forms from **19** at room temperature in the absence of catalyst.

Identical results are obtained from the catalytic reaction in the presence and absence of ambient laboratory light for 24 h. Stirring a solution of **59** without added copper(I) halide under ambient laboratory light results in the conversion to 60% **19** after 24 h; however, with added CuCl or CuI under ambient light, only a small amount (< 5%) of **19** is formed. These results suggest that the presence of the copper(I) halide prevents formation of significant amounts of **19**, presumably by reconversion of photochemically formed **19** to **59**.

Scheme 19

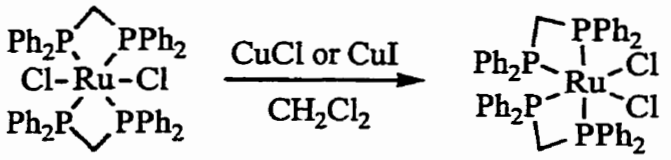

19 **59**

6.3.2 Synthesis and Structure of 74

A small amount (< 5%) of a new phosphorus-containing product is also observed by ^{31}P NMR prior to workup when CuCl is used as the catalyst in Scheme 19. This product is obtained in high yield when a CH_2Cl_2 solution of **19** or **59** is stirred with excess CuCl at room temperature for 2 h. This complex is isolated and characterized as **74**.

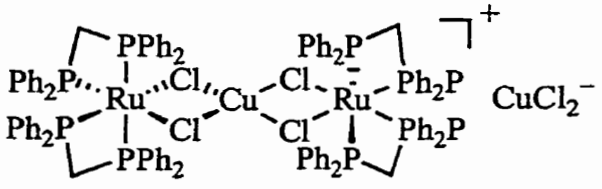

74

Diffusion of hexanes into a 1,2-dichloroethane solution of complex **74** produces yellow crystals whose structure is determined by single-crystal X-ray diffraction (Figure 40). The structure shows that the cation of **74** is a halide-bridged heterotrimetallic cationic complex in which the copper center has four chloride ligands bridging to the two ruthenium atoms. Although halide-bridging ligands are common in coordination chemistry, halide-bridged heterobimetallic complexes are uncommon, and only several have been structurally characterized.[163-166] Complex **74** is the first example of a complex containing a dihalide bridge between ruthenium and copper centers. A previous study proposed a single bridging chloride on the basis of NMR evidence for $[(\eta^3{:}\eta^3\text{-}C_{10}H_{16})Cl_2Ru(\mu\text{-}Cl)Cu(PCy_3)]$.[165] In

complex **74**, the Cu atom is in a severely distorted tetrahedral environment with four equal Cu–Cl bond lengths of 2.398(2) Å. In comparison, the Cu–Cl bonds in [{$(C_5H_{10}NO)_2Mo(\mu_2$-$S)_2Cu(\mu_2$-$Cl)\}_2$] are 2.375(1) and 2.341(2) Å in length, while the Cu centers in this complex are much closer to a tetrahedral geometry than those in **74**.[167] The ruthenium centers in complex **74** are in a slightly twisted trigonal-antiprismatic coordination, with Cl(1), P(3), and P(2) forming one face and Cl(2), P(4) and P(1) forming the opposite face. The Ru–Cl bonds in **74** (2.469(2), 2.470(2) Å) are slightly longer than the corresponding bonds in **59** (2.440(2), 2.451(13) Å), while the Cl–Ru–Cl angle is smaller in **74** (82.03(7)) than in **59** (84.1(5)).[168] The $[CuCl_2]^-$ counterion of **74** is linear with a Cu–Cl bond length of 2.101(4) Å, similar to the Cu–Cl bond length in [(*n*-Bu)$_4$N][$CuCl_2$] (2.107(1) Å).[169]

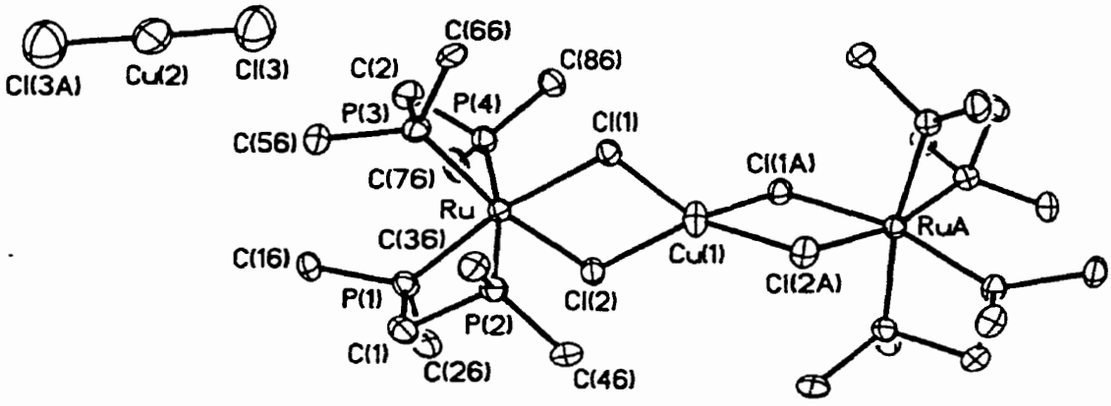

Figure 40. ORTEP diagram of the solid-state molecular structure of **74**·solvent. The solvent molecules and the phenyl groups, except the *ipso* carbon atoms, are omitted for clarity. The thermal ellipsoids are depicted at 30% probability.

Table 16. Selected Bond Lengths in **74**·solvent (Å)

Ru – P(1)	2.303(2)	Cu(1) – Cl(2)	2.398(2)	P(2) – C(36)	1.828(6)
Ru – P(2)	2.363(2)	Cu(1) – Cl(2A)	2.398(2)	P(2) – C(46)	1.820(4)
Ru – P(3)	2.312(2)	Cu(2) – Cl(3)	2.101(4)	P(3) – C(2)	1.856(8)
Ru – P(4)	2.351(2)	Cu(2) – Cl(3A)	2.101(4)	P(3) – C(56)	1.832(5)
Ru – Cl(1)	2.470(2)	P(1) – C(1)	1.856(9)	P(3) – C(66)	1.844(5)
Ru – Cl(2)	2.469(2)	P(1) – C(16)	1.842(5)	P(4) – C(2)	1.822(9)
Cu(1) – Cl(1)	2.398(2)	P(1) – C(26)	1.845(5)	P(4) – C(76)	1.80(1)
Cu(1) – Cl(1A)	2.398(2)	P(2) – C(1)	1.853(8)	P(4) – C(86)	1.820(5)

Table 17. Selected Bond Angles in **74**·solvent (deg)

P(1) – Ru – P(2)	72.01(8)	Cl(1) – Cu(1) – Cl(2A)	113.79(8)
P(1) – Ru – P(3)	95.16(8)	Cl(1A) – Cu(1) – Cl(2A)	85.04(7)
P(1) – Ru – P(4)	100.38(8)	Cl(2) – Cu(1) – Cl(2A)	134.9(1)
P(2) – Ru – P(3)	102.30(8)	Cl(3) – Cu(2) – Cl(3A)	180.0
P(2) – Ru – P(4)	170.41(8)	C(1) – P(1) – Ru	96.6(2)
P(3) – Ru – P(4)	72.09(8)	C(16) – P(1) – Ru	126.1(2)
P(1) – Ru – Cl(1)	164.71(8)	C(26) – P(1) – Ru	119.3(2)
P(1) – Ru – Cl(2)	93.61(8)	C(1) – P(2) – Ru	94.6(3)
P(2) – Ru – Cl(1)	93.45(7)	C(36) – P(2) – Ru	123.2(2)
P(2) – Ru – Cl(2)	92.34(8)	C(46) – P(2) – Ru	123.1(2)

P(3) – Ru – Cl(1)	92.51(7)	C(2) – P(3) – Ru	95.0(3)
P(3) – Ru – Cl(2)	164.69(8)	C(56) – P(3) – Ru	127.1(2)
P(4) – Ru – Cl(1)	94.56(7)	C(66) – P(3) – Ru	120.4(2)
P(4) – Ru – Cl(2)	93.99(8)	C(2) – P(4) – Ru	94.7(3)
Cl(1) – Ru – Cl(2)	82.03(7)	C(76) – P(4) – Ru	122.8(4)
Cl(1) – Cu(1) – Cl(2)	85.03(7)	C(86) – P(4) – Ru	121.8(2)
Cl(1A) – Cu(1) – Cl(2)	113.80(8)	Cu(1) – Cl(1) – Ru	96.42(7)
Cl(1) – Cu(1) – Cl(1A)	131.2(1)	Cu(1) – Cl(2) – Ru	96.44(8)

6.3.3 NMR Studies

When pure crystalline **74** is dissolved in CD_2Cl_2, the ^{31}P NMR spectrum obtained suggests that several complexes are present in solution (Figure 41). Complex **74** is poorly soluble in most other weak donor solvents; however, the ^{31}P NMR spectrum of **74** in mixtures of CD_2Cl_2 and acetone or THF is similar to that in pure CD_2Cl_2. Complex **74** reacts with stronger donor solvents such as CH_3CN or CH_3NO_2. In CD_2Cl_2, the ^{31}P NMR spectrum consists of two major triplets (δ –0.5 and –28.2) and two smaller triplets (δ –0.4 and –25.3). In addition, there are broad peaks at δ 0 and –25 which overlap the triplets. The four sharp triplets are assigned to two cis-substituted ruthenium complexes present in an approximately 4:1 ratio when **74** dissolves. Neither of these complexes is **59**, and the small chemical shift differences between the sets of peaks indicate that they are structurally similar. These two major compounds are proposed to be **74** and the intermediate **75** (Scheme 20).

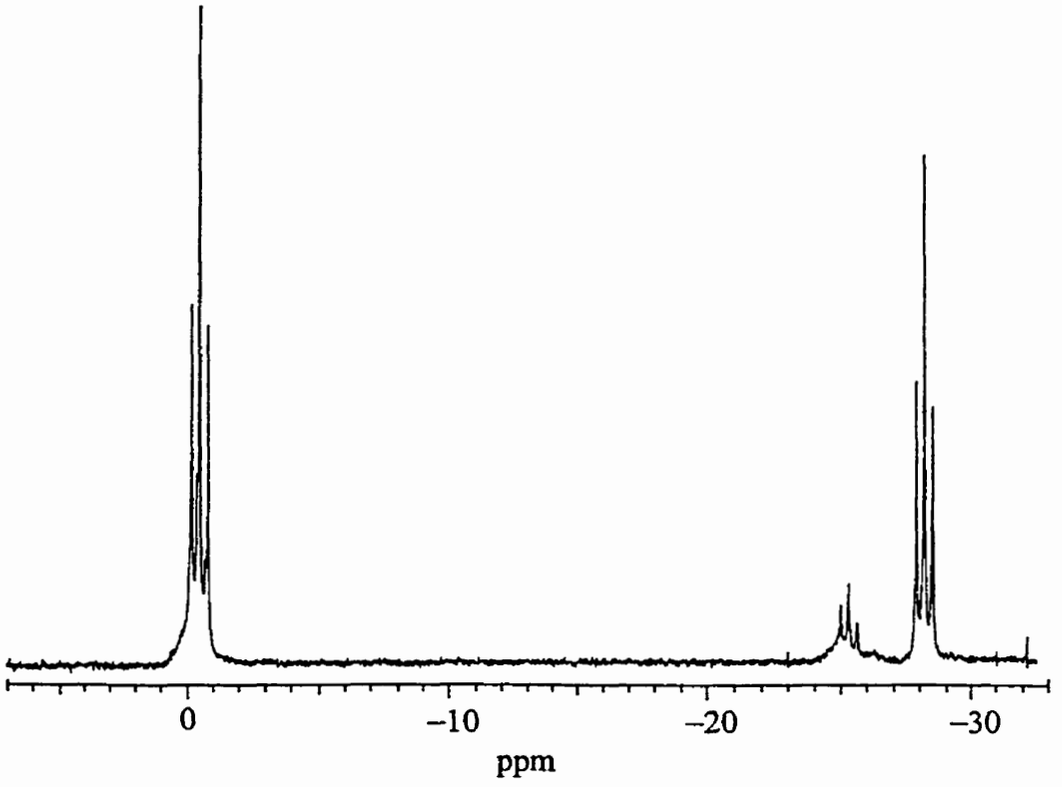

Figure 41. ^{31}P NMR spectrum of **74** in CD_2Cl_2.

The molar conductivity of an acetone solution of **74** is 207 Ω^{-1} cm^2 mol^{-1}, indicating that the major species in solution is the 1:1 electrolyte **74**. The broad peaks in the ^{31}P NMR spectrum may be due to species **76**, which would result if one of the Cu–Cl bonds in **75** breaks. The broad peaks can result from inequivalency of the phosphorus atoms in **76** or from chemical exchange with **59**. Since **74** is a strong electrolyte, the relative concentrations of the species in Scheme 20 are expected to be independent of the amount of **74** added. A 10-fold increase in the amount of **74** dissolved does not change the ratio of **74** to the sum of **75** and **76** (integrated together in the ^{31}P NMR spectrum), consistent with the equilibria in Scheme 20.

Addition of excess [(*n*-Bu)$_4$N]Cl or 2 M aq HCl to a solution of **74** in CH_2Cl_2 results in complete conversion of all species present to **59**. The added Cl^- presumably complexes the copper as $CuCl_2^-$, leaving **59** as the only ruthenium-containing species. Subsequent addition of excess CuCl to a solution of **74** which had been treated with excess [(*n*-Bu)$_4$N]Cl results in the disappearance of peaks due to **59** and the reappearance of sharp peaks due to **74** and **75** as well as the broad peaks δ 0 and –25 in the ^{31}P NMR spectrum. These experiments demonstrate that **59** and **74** – **76** may be interconverted in the presence of CuCl and Cl^-, and that the relative concentrations of these species in solution depend on the amount of CuCl and Cl^- present.

Scheme 20

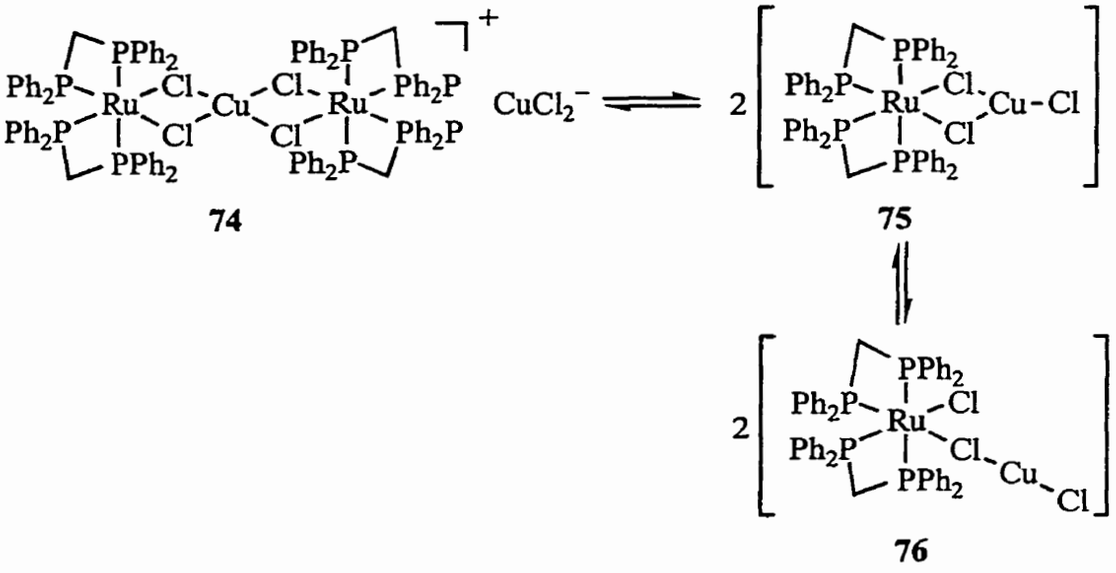

74 **75**

76

The progress of the reaction of **19** with one equivalent of CuCl in CD_2Cl_2 is followed by ^{31}P NMR. Since CuCl is poorly soluble, only a small amount dissolves initially, and the reaction conditions are identical to the catalytic experiments. Upon addition of CuCl into the tube, the singlet in the ^{31}P NMR at δ –7.7 due to **19** broadens. In the early stages of the

reaction, sharp resonances due to **59** begin to appear, and eventually the resonances due to **74** and **75** also become apparent. When an identical experiment is carried out with **59** and stoichiometric CuCl, reaction is very rapid in the NMR tube with complete disappearance of **59** and formation of the equilibrium mixture of **74** – **76** within 5 min.

Complex **19** isomerizes to **59** when a small amount of **74** is added to the solution. A solution of **19** and 4 mol % **74** in CH_2Cl_2 is stirred at room temperature for 24 h, affording a solution which contained 90% **59** and 10% **19** by ^{31}P NMR. Addition of a small amount of complex **74** to the isomerization reaction is analogous to adding catalytic CuCl. Intermediates **75** and **76** are formed directly in solution from **74**, introducing coordinated CuCl, which acts as a catalyst for the isomerization.

The UV–vis absorption spectrum obtained when **74** is dissolved in CH_2Cl_2 is similar to that of **59** (Figure 42). It is likely that the bands in the spectrum of **74** are due to the same transitions observed for **59**, with slight distortions due to the change in the ligand field around ruthenium upon coordination of the copper center. Since both **74** and **75** have very similar ligand environments at the ruthenium center, it is reasonable that both complexes exhibit similar visible transitions to **59**. Solutions of **74** are stable under ambient laboratory light, consistent with the cis chloride ligands being locked in place on the ruthenium center by the copper, preventing photochemical isomerization.

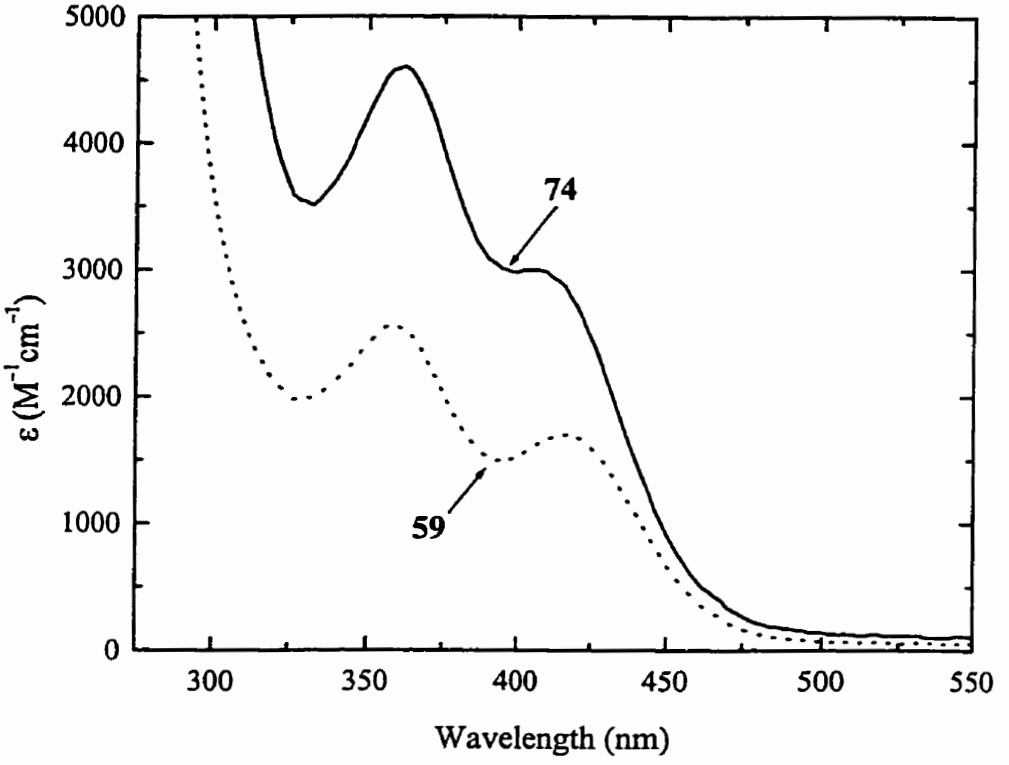

Figure 42. Absorption spectra of **59** (...) and **74** (—) in CH_2Cl_2.

6.4 Discussion

The following mechanism is proposed for the CuCl-catalyzed isomerization of **19** to **59**. As the CuCl dissolves, it coordinates to one of the chloride ligands in **19**, yielding halide-bridged intermediate **77** (Scheme 21). Complex **77** is not observed in the ^{31}P NMR spectrum, but a broadening of the singlet at δ –7.7 is observed. This broadening is specific to this peak, and is not due to nonspecific broadening as would be caused by paramagnetic Cu^{II} impurities. It is possible that the broadening is caused by exchange between **77** and **19**. The ruthenium center in intermediate **77** is still trans substituted. Coordination of the CuCl is expected to

weaken the Ru–Cl bond, facilitating isomerization to the more stable cis orientation at the ruthenium center. The Ru–Cl bond is lengthened in **74** compared to **59**, consistent with a weakening of the Ru–Cl bond upon coordination of Cu^{I}. Thermodynamically, $RuCl_2(dppm)_2$ prefers the cis orientation. Meyer argued that this is because **59** is stabilized by π-donation from the Cl through the Ru to a trans P, whereas this favorable interaction is not possible in the trans isomer.[120]

Scheme 21

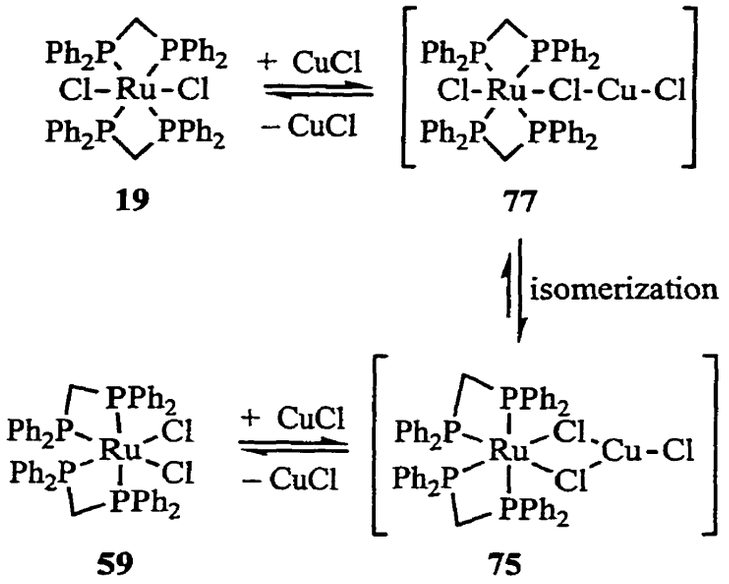

19 **77** **59** **75**

It is proposed here that **77** isomerizes to **75**, in which the ruthenium center has a cis geometry, and the CuCl is coordinated to both chloride ligands. The intermediate **75** can then lose CuCl, presumably via **76**, to yield **59**. This pathway is likely under catalytic conditions when there is a large excess of ruthenium species relative to CuCl. Under these conditions, any **75** which forms probably reacts with **19**, yielding **59** and **77**. The equilibrium between **77** and **75** is expected to favor **75** due to both the favorable geometry of the ruthenium center in this complex, and the stabilizing effect of coordination of the copper with the two bridging

chlorides. The effect of the CuCl is therefore to weaken the Ru–Cl bond in **77** and to stabilize intermediate **75**. When stoichiometric amounts of CuCl are available, sufficient copper is present to complex all the available ruthenium species. Since the reaction between **59** and CuCl is rapid, it is reasonable that **74** and **75** are the final products observed in the reaction between **19** and stoichiometric CuCl. Because CuCl is poorly soluble, **59** is observed first in this reaction followed by **74** and **75** as **19** is consumed, and **59** is formed.

The copper(I) halide catalyzed isomerization of **19** to **59** provides an alternative, low-temperature route to the cis complex. Although a previous report indicated that complexes structurally related to **19** such as *trans*-[$RuCl_2((o\text{-}C_6H_4(PMePh)_2)_2$] can be isomerized to the corresponding cis isomer using excess triethylaluminum, this procedure involves air-sensitive reagents and proceeds via hydrido intermediates which must be hydrolyzed to regenerate the product.[170] The method described here may allow for the convenient preparation of cis isomers of similar complexes which are difficult to isomerize thermally.

The results in this Chapter are important for understanding copper(I) halide catalyzed reactions involving **19** and **59**. It is likely that coupling reactions of ruthenium halide complexes with organostannane involve intermediates such as **74** – **77** in which the copper coordinates to the ruthenium halide complex. When the starting material is **19**, copper-catalyzed isomerization may generate cis-substituted intermediates in which the chloride ligands are more labile, facilitating reaction with the organostannane. In addition, since **74** is a soluble complex, it may be useful to use this directly as a reagent with organostannanes to make bisacetylide complexes and polymers.

6.5 Conclusions

Copper(I) halides are studied as catalysts for the trans – cis isomerization of $RuCl_2(dppm)_2$. When $RuCl_2(dppm)_2$ reacts with excess CuCl, a halide-bridged heterotrimetallic complex is isolated. An NMR study on the reaction of $RuCl_2(dppm)_2$ with CuCl provides some insight into the isomerization mechanism.

Chapter 7 Suggestions for Future Work

The work in this thesis opens many avenues for future exploration of metal-containing oligomers and polymers. Some of these are summarized in this Chapter.

Ruthenium oligothienylacetylide polymers may have significant conductivities when doped because oxidation of the ruthenium(II) centers in **62c** and **63c** results in very strong low-energy absorptions in the near-IR region. Measurement of the conductivities of the electropolymerized films of those materials would be interesting. Chemical coupling may also be used to produce such polymers. Preliminary results have showed that coupling of **58** with **78** gives an insoluble brown-red solid, which is presumably the polymer **79** (Scheme 22). Further characterization of this solid and preparation of analogous polymers which are soluble would be useful. The solubility of this polymer is expected to increase as alkyl groups are incorporated into either the oligothienyl groups or phosphine ligands, but care must be taken to consider the steric effects of these groups, which may reduce the efficiency of the coupling.

Scheme 22

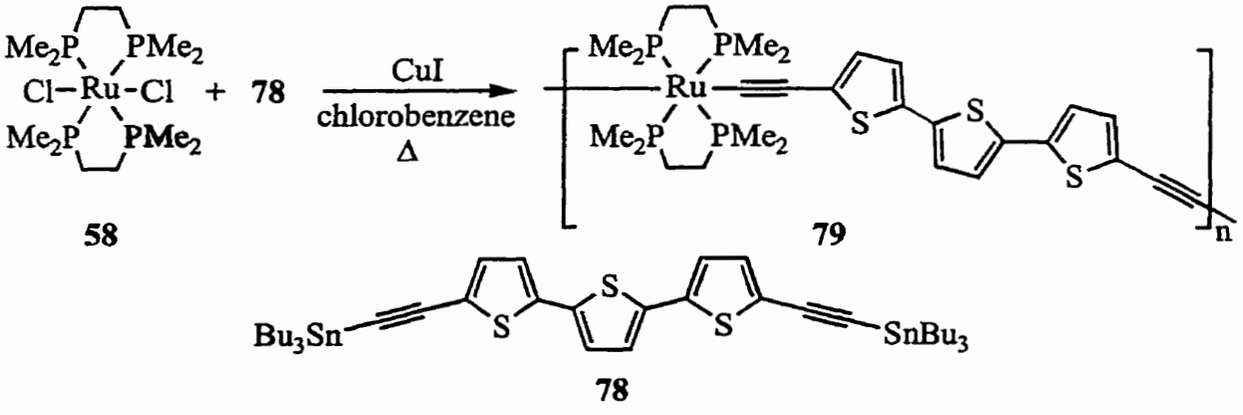

Electropolymerization of **63b** and **63c** results in the deposition of electrochromic films on the electrodes, but the nature of the films is not clear because of the poor stability of

oxidized **63b** and **63c** in solution at room temperature. The stability of these species could be enhanced through the use of more electron-rich phosphine ligands on the metal and oligothienyl groups with a lower oxidation potential. The latter could be achieved by using oligothienyl groups with a longer conjugation length or with electron-donating substituents.

Preliminary conductivity measurements on films prepared by electropolymerization of **50** and **73**, and electrodimerization of **68c** and **68e** are attempted on interdigitated microelectrodes with an interelectrode spacing of 5 μm. This method, developed by Wrighton and coworkers, allows the conductivity to be measured as a function of applied potential.[171-173] This method requires that the film must fill the interelectrode gap. In all cases, it is impossible to obtain sufficiently thick films to bridge the gap between the electrodes, and it is clear that interdigitated electrodes with a smaller gap (around 1 μm) are needed.

Murray and coworkers have measured the conductivity of polymer films using a sandwich-electrode arrangement in which a polymer film is deposited on a Pt surface, with a gold film evaporated on top of the polymer film.[174] A modified method is attempted to obtain conductivity measurements of films of the dimers **71** and **72**. In these experiments, a Pt electrode coated with a film of the dimer is dipped into a mercury pool, and the resistance between the Pt and mercury electrodes measured. Using this method the conductivity of the neutral film of the dimer **71** is obtained (3×10^{-8} S/cm), but consistent results can not be obtained for the oxidized film. It is impossible to measure the conductivity of films of **72** in this way because they crack when dry resulting in shorts between the electrodes. Further investigations are needed to obtain satisfactory and useful data from those measurements.

References

(1) Feynman, R. *Eng. Sci.* **1960**, *23*, 22.

(2) Aviram, A.; Ratner, M. *Molecular Electronics: Science and Technology*; The New York Academy of Sciences:, 1998; Vol. 852.

(3) Reed, M. A. *Proc. IEEE* **1999**, *87*, 652-658.

(4) Reinerth, W. A.; Jones, L.; Burgin, T. P.; Zhou, C. W.; Muller, C. J.; Deshpande, M. R.; Reed, M. A.; Tour, J. M. *Nanotechnology* **1998**, *9*, 246-250.

(5) Munn, R. W. *Chem. Br.* **1984**, 518-524.

(6) Mirkin, C. A.; Ratner, M. A. *Annu. Rev. Phys. Chem.* **1992**, *43*, 719-754.

(7) Kelly, T. R.; Silva, H. D.; Silva, R. A. *Nature* **1999**, *401*, 150-152.

(8) Koumura, N.; Zijlstra, R. W.; Delden, R. A. V.; Harada, N.; Feringa, B. L. *Nature* **1999**, *401*, 152-154.

(9) Shirakawa, H.; Louis, E. J.; MacDiarmid, A. G.; Chiang, C. K.; Heeger, A. J. *J. Chem. Soc., Chem. Commun.* **1977**, 578-580.

(10) Skotheim, T. A. *Handbook of Conducting Polymers*; 1st ed.; Marcel Dekker: New York and Basel, 1986; Vol. 1-2.

(11) Skotheim, T. A.; Elsenbaumer, R. L.; Reynolds, J. R. *Handbook of Conducting Polymers*; 2nd ed.; Marcel Dekker: New York, 1998.

(12) Naarmann, H.; Theophilou, N. *Synth. Met.* **1987**, *22*, 1-8.

(13) Tsukamoto, J.; Takahashi, A.; Kawasaki, K. *Jpn. J. Appl. Phys.* **1990**, *29*, 125-130.

(14) Pham, C. V.; Burkhardt, A.; Shabana, R.; Cunningham, D. D.; Mark, H. B. J.; Zimmer, H. *Phosphorus, Sulfur, and Silicon* **1989**, *46*, 153-168.

(15) Salzner, U.; Lagowski, J. B.; Pickup, P. G.; Poirier, R. A. *Synth. Met.* **1998**, *96*, 177-189.

(16) Hotta, S.; Soga, M.; Sonoda, N. *Synth. Met.* **1988**, *26*, 267-269.

(17) Kossmehl, G.; Chatzitheodorou, G. *Mol. Cryst. Liq. Cryst.* **1982**, *83*, 291-296.

(18) Berlin, A.; Pagani, G. A.; Sannicolo, F. *J. Chem. Soc., Chem. Commun.* **1986**, 1663-1664.

(19) Tourillon, G.; Garnier, J. A. *J. Electroanal. Chem.* **1984**, *161*, 51-58.

(20) Waltman, R. J.; Bargon, J.; Diaz, A. F. *J. Phys. Chem.* **1983**, 1459-1463.

(21) Diaz, A. F.; Crowley, J.; Bargon, J.; Gardini, G. P.; Torrance, J. B. *J. Electroanal. Chem.* **1981**, *121*, 355-361.

(22) Martinez, F.; Voelkel, R.; Naegele, D.; Naarmann, H. *Mol. Cryst. Liq. Cryst.* **1989**, *167*, 227-232.

(23) Bäuerle, P.; Segelbacher, U.; Gaudl, K.-U.; Huttenlocher, D.; Mehring, M. *Angew. Chem. Int. Ed. Engl.* **1993**, *32*, 76-78.

(24) Fichou, D.; Demanze, F.; Horowitz, G.; Hajlaoui, R.; Constant, M.; Ganier, F. *Synth. Met.* **1997**, *85*, 1309-1312.

(25) Zotti, G.; Schiavon, G.; Berlin, A.; Pagani, G. *Chem. Mater.* **1993**, *5*, 430-436.

(26) Kagan, J.; Arora, S. K. *Heterocycles* **1983**, *20*, 1937-1940.

(27) Horowitz, G.; Hajlaoui, R.; Kouki, F. *Eur. Phys. J. Appl. Phys.* **1998**, *1*, 361-367.

(28) Horowitz, G. *Adv. Mater.* **1998**, *10*, 365-377.

(29) Torsi, L.; Dodabalapur, A.; Rothberg, L. J.; Fung, A. W. P.; Katz, H. E. *Phys. Rev. B* **1998**, *57*, 2271-2275.

(30) Fichou, D.; Horowitz, G.; Xu, B.; Garnier, F. *Synth. Met.* **1990**, *39*, 243-260.

(31) Hush, N. S. *Prog. Inorg. Chem.* **1967**, *8*, 391-444.

(32) Nelson, S. F.; Tran, H. Q.; Nagy, M. A. *J. Am. Chem. Soc.* **1998**, *120*, 298-304.

(33) Lambert, C.; Nöll, G. *J. Am. Chem. Soc.* **1999**, *121*, 8434-8442.

(34) Desjardins, P.; Yap, G. P. A.; Crutchley, R. J. *Inorg. Chem.* **1999**, *38*, 5901-5905.

(35) Creutz, C.; Newton, M. D.; Sutin, N. *J. Photochem. Photobiol. A: Chem.* **1994**, *82*, 47-59.

(36) Evans, C. E. B.; Ducharme, D.; Naklicki, M. L.; Crutchley, R. J. *Inorg. Chem.* **1995**, *34*, 1350-154.

(37) Creutz, C. *Prog. Inorg. Chem.* **1983**, *30*, 1-73.

(38) Crutchley, R. J. *Adv. Inorg.Chem.* **1994**, *41*, 273-325.

(39) Creutz, C.; Taube, H. *J. Am. Chem. Soc.* **1973**, *95*, 1086-1094.

(40) Richardson, D. E.; Taube, H. *Coord. Chem. Rev.* **1984**, *60*, 107-128.

(41) Rosa, R. D. L.; Chang, P. J.; Salaymeh, F.; Curtis, J. C. *Inorg. Chem.* **1985**, *24*, 4229-4231.

(42) Robin, M. B.; Day, P. *Adv. Inorg. Chem. Radiochem.* **1967**, *10*, 247-422.

(43) Levanda, C.; Bechgaard, K.; Cowan, D. O. *J. Org. Chem.* **1976**, *41*, 2700-2704.

(44) Morrison, W. H.; Krogsrud, J., S.; Hendrickson, D. S. *Inorg. Chem.* **1973**, *12*, 1998-2004.

(45) Ribou, A.-C.; Launay, J.-P.; Sachtleben, M. L.; Li, H.; Spangler, C. W. *Inorg. Chem.* **1996**, *35*, 3735-3740.

(46) Coat, F.; Lapinte, C. *Organometallics* **1996**, *15*, 477-479.

(47) Belanzoni, P.; Re, N.; Sgamellotti, A.; Floriani, C. *J. Chem. Soc., Dalton Trans.* **1998**, 1825-1835.

(48) Brady, M.; Weng, W.; Zhou, Y.; Seyler, J. W.; Amoroso, A. J.; Arif, A. M.; Böhme, M.; Frenking, G.; A., Gladysz. J. A. *J. Am. Chem. Soc.* **1997**, *119*, 775-788.

(49) Guillemot, M.; Toupet, L.; Lapinte, C. *Organometallics* **1998**, *17*, 1928-1930.

(50) Bunz, U. H. *Angew. Chem. Int. Ed. Engl.* **1996**, *35*, 969-971.

(51) Bartik, T.; Bartik, B.; Brady, M.; Dembinski, R.; Gladysz, J. A. *Angew. Chem. Int. Ed. Engl.* **1996**, *35*, 414-417.

(52) Colbert, M. C. B.; Lewis, J.; Long, N. J.; Raithby, P. R.; Younus, M.; White, A. J. P.; Williams, D., J.; Payne, N. N.; Yellowlees, L.; Beljonne, D.; Chawdhury, N.; Friend, R. H. *Organometallics* **1998**, *17*, 3034-3043.

(53) Jones, N. D.; Wolf, M. O.; Giaquinta, D. M. *Organometallics* **1997**, *16*, 1352-1354.

(54) Colbert, M. C. B.; Lewis, J.; Long, N. J.; Raithby, P. R.; White, A. J. P.; Williams, D., J. *J. Chem. Soc., Dalton Trans.* **1997**, 99-104.

(55) Osella, D.; Gambino, O.; Nervi, C.; Ravera, M.; Russo, M. V.; Infante, G. *Inorg. Chim. Acta* **1994**, *225*, 35-40.

(56) Sato, M.; Hayashi, Y.; Kumakura, S.; Shimizu, N.; Katada, M.; Kawata, S. *Organometallics* **1996**, *15*, 721-728.

(57) Hanack, M.; Lang, M. *Adv. Mater.* **1994**, *6*, 819-833.

(58) Takahashi, S.; Kariya, M.; Yatake, T.; Sonogshira, K.; Hagihara, N. *Macromolecules* **1978**, *11*, 1063-1066.

(59) Sonogashira, K.; Kataoka, S.; Takahashi, S.; Hagihara, N. *J. Organomet. Chem.* **1978**, *160*, 319-327.

(60) Takahashi, S.; Ohyama, Y.; Murata, E.; Sonogashira, K.; Hagihara, N. *J. Polym. Sci., Polym. Chem. Ed.* **1980**, *18*, 349-353.

(61) Takahashi, S.; Murata, E.; Sonogashira, K.; Hagihara, N. *J. Polym. Sci., Polym. Chem. Ed.* **1980**, *18*, 661-669.

(62) Hagihara, N.; Sonogashira, K.; Takahashi, S. *Adv. Polym. Sci.* **1981**, *41*, 149-179.

(63) Takahashi, S.; Morimoto, H.; Murata, E.; Kataoka, S.; Sonogashira, K.; Hagihara, N. *J. Polym. Sci., Polym. Chem. Ed.* **1982**, *20*, 565-573.

(64) Johnson, B. F. G.; Kakkar, A. K.; Khan, M. S.; Lewis, J. *J. Organomet. Chem.* **1991**, *409*, C12-C14.

(65) Khan, M. S.; Schwartz, N. A.; Kakkar, A. K.; Lin, B.; Raithby, P. R.; Lewis, J. *Z. Anorg. Allg. Chem.* **1992**, *616*, 121-124.

(66) Khan, M. S.; Davies, S. J.; Kakkar, A. K.; Schwartz, D.; Lin, B.; Johnson, B. F. G.; Lewis, J. *J. Organomet. Chem.* **1992**, *424*, 87-97.

(67) Lewis, J.; Khan, M. S.; Kakkar, A. K.; Johnson, B. F. G. *J. Organomet. Chem.* **1992**, *425*, 165-176.

(68) Sun, Y.; Taylor, N. J.; Carty, A. J. *Organometallics* **1992**, *11*, 4293-4300.

(69) Garnier, F.; Yassar, A., U.S. Patent 5272238, 1993

(70) Frapper, G.; Kertesz, M. *Inorg. Chem.* **1993**, *32*, 732-740.

(71) Faulkner, C. W.; Ingham, S. L.; Khan, M. S.; Lewis, J.; Long, N. J.; Raithby, P. R. *J. Organomet. Chem.* **1994**, *482*, 139-145.

(72) Markwell, R., D.; Butler, I. S.; Kakkar, A. K.; Khan, M. S.; Al-Zakwani, Z. H.; Lewis, J. *Organometallics* **1996**, *15*, 2331-2337.

(73) Irwin, M. J.; Vittal, J. J.; Puddephatt, R. J. *Organometallics* **1997**, *16*, 3541-3547.

(74) Russo, M. V.; Furlani, A.; Altamura, P.; Fratoddi, I.; Polzonetti, G. *Polymer* **1997**, *38*, 3677-3690.

(75) Chawdhury, N.; Köhler, A.; Friend, R. H.; Wong, W. Y.; Lewis, J.; Younus, M.; Raithby, P. R.; Corcoran, T. C.; Al-Mandhary, M. R. A.; Khan, M. S. *J. Chem. Phys.* **1999**, *10*, 4963-4970.

(76) Kingsborough, R. P.; Swager, T. M. *Prog. Inorg. Chem.* **1999**, *48*, 123-231.

(77) Porter, P. L.; Guha, S.; Kang, K.; Frazier, C. C. *Polymer* **1991**, *32*, 1756-1760.

(78) Dray, A. E.; Wittmann, F.; Friend, R. H.; Donald, A. M.; Khan, M. S.; Lewis, J.; Johnson, B. F. G. *Synth. Met.* **1991**, *41-43*, 871-874.

(79) Messier, J.; Kajzar, F.; Prasad, P. *Organic Molecules for Nonlinear Optics and Photonics*; Kluwer Academic Publishers: Dordrecht; Boston, 1991.

(80) Atherton, Z.; Faulkner, C. W.; Ingham, S. L.; Kakkar, A. K.; Khan, M. S.; Lewis, J.; Long, N. J.; Raithby, P. R. *J. Organomet. Chem.* **1993**, *462*, 265-270.

(81) Chawdhury, N.; Köhlor, A.; Friend, R. H.; Younus, M.; Long, N. J.; Raithby, P. R.; Lewis, J. *Macromolecules* **1998**, *31*, 722-727.

(82) Davies, S. J.; Johnson, B. F. G.; Lewis, J.; Raithby, P. R. *J. Organomet. Chem.* **1991**, *414*, C51-C53.

(83) Khan, M. S.; Kakkar, A. K.; Ingham, S. L.; Raithby, Paul R.; Lewis, J. *J. Organomet. Chem.* **1994**, *472*, 247-255.

(84) Khan, M. S.; Kakkar, A. K.; Long, N. J.; Lewis, J.; Raithby, P. R.; Nguyen, P.; Marder, F.; Wittmann, F.; Friend, R. H. *J. Mater. Chem.* **1994**, *4*, 1227-1232.

(85) Lewis, J.; Long, N. J.; Raithby, P. R.; Shields, G. P.; Wong, W.-Y.; Younus, M. *J. Chem. Soc., Dalton Trans.* **1997**, 4283-4288.

(86) Lavastre, O.; Even, M.; Dixneuf, P. H.; Pacreau, A.; Vairon, J. P. *Organometallics* **1996**, *15*, 1530-1531.

(87) Bilow, N.; Landis, A.; Rosenberg, H. *J. Polym. Sci., Polym. Chem. Ed.* **1969**, *7*, 2719-2736.

(88) Cowan, D. O.; Park, J.; Pittma, C. U. J.; Sasaki, Y.; Mukherjee, T. K.; Diamond, N. A. *J. Am. Chem. Soc.* **1972**, *94*, 5110-5112.

(89) Pittman, C. U. J.; Sasaki, Y.; Mukherjee, T. K. *Chem. Lett.* **1975**, 383-386.

(90) Neuse, E. W.; Bednarik, L. *Macromolecules* **1979**, *12*, 187-195.

(91) Yamamoto, T.; Sanechika, K.-I.; Yamamoto, A.; Katada, M.; Motoyama, I.; Sano, H. *Inorg. Chim. Acta* **1983**, *73*, 75-82.

(92) Neuse, E. W.; Trifan, D. S. *J. Am. Chem. Soc.* **1963**, 1952-1958.

(93) Neuse, E. W.; Khan, F. B. D. *Macromolecules* **1986**, *19*, 269-272.

(94) Nelson, J. M.; Rengel, H.; Manners, I. *J. Am. Chem. Soc.* **1993**, *115*, 7035-7036.

(95) Barlow, S.; O'Hare, D. *Chem. Rev.* **1997**, *97*, 637-669.

(96) Buretea, M.; Tilley, T. D. *Organometallics* **1997**, *16*, 1507-1510.

(97) Arnold, R.; Matchett, S. A.; Rosenblum, M. *Organometallics* **1988**, *7*, 2261-2266.

(98) Nugent, H. M.; Rosenblum, M. *J. Am. Chem. Soc.* **1993**, *115*, 3848-3849.

(99) Funaki, H.; Aramaki, K.; Nishihara, H. *Synth. Met.* **1995**, *74*, 59-64.

(100) Yamamoto, T.; Morikita, T.; Maruyama, T.; Kubota, k.; Katada, M. *Macromolecules* **1997**, *30*, 5390-5396.

(101) Knapp, R.; Velten, U.; Rehahn, M. *Polymer* **1998**, *39*, 5827-5838.

(102) Morikita, T.; Maruyama, T.; T., Y.; Kubota, K.; Katada, M. *Inorg. Chim. Acta* **1998**, *269*, 310-312.

(103) Foucher, D. A.; Honeyman, C. H.; Nelson, C. H.; Tang, B. Z.; Manners, I. *Angew. Chem. Int. Ed. Engl.* **1993**, *32*, 1702-1711.

(104) Foucher, D. A.; Tang, B. Z.; Manners, I. *J. Am. Chem. Soc.* **1992**, *114*, 6246-6248.

(105) Brandt, P. F.; Rauchuss, T. B. *J. Am. Chem. Soc.* **1992**, *114*, 1926-1927.

(106) Manners, I. *Adv. Mater.* **1994**, *6*, 68-71.

(107) Manners, I. *Adv. Organomet. Chem.* **1995**, *37*, 131-168.

(108) Hirao, T.; Kurashina, M.; Aramaki, K.; Nishihara, H. *J. Chem. Soc., Dalton Trans.* **1996**, 2929-2933.

(109) Foucher, D. A.; Ziembinski, R.; Tang, B. Z.; Macdonald, P. M.; Massey, J.; Jaeger, R.; Vancso, G. J.; Manners, I. *Macromolecules* **1993**, *26*, 2878-2884.

(110) Hmyene, M.; Yassar, A.; Escorne, M.; Percheron-Guegan, A.; Garnier, F. *Adv. Mater.* **1994**, *6*, 564-568.

(111) Ingham, S. L.; Khan, M. S.; Lewis, J.; Long, N. J.; Raithby, P. R. *J. Organomet. Chem.* **1994**, *470*, 153-159.

(112) Wrighton, M. S. *Science* **1986**, *231*, 32-37.

(113) Segawa, H.; Wu, F.-P.; Nakayama, N.; Maruyama, H.; Sagisaka, S.; Higuchi, N.; Fujitsuka, M.; Shimidzu, T. *Synth. Met.* **1995**, *71*, 2151-2154.

(114) Zhu, S. S.; Kingsborough, R. P.; Swager, T. M. *J. Mater. Chem.* **1999**, *9*, 2123-2131.

(115) Kingsborough, R. P.; Swager, T. M. *Adv. Mater.* **1998**, *10*, 1100-1104.

(116) Kingsborough, R. P.; Swager, T. M. *J. Am. Chem. Soc.* **1999**, *121*, 8825-8834.

(117) Higgins, S. J.; Jones, C. L.; Francis, S. M. *Synth. Met.* **1999**, *98*, 211-214.

(118) Manna, J.; John, K. D.; Hopkins, M. D. *Adv. Organomet. Chem.* **1995**, *38*, 79-154.

(119) Chatt, J.; Hayter, R. G. *J. Chem. Soc.* **1961**, 896-904.

(120) Sullivan, B. P.; Meyer, T. J. *Inorg. Chem.* **1982**, *21*, 1037-1040.

(121) Smart, J. C.; Pinsky, B. L. *J. Am. Chem. Soc.* **1980**, *102*, 1009-1014.

(122) Polin, J.; Schottenberger, H. *Org. Synth.* **1996**, *73*, 262-269.

(123) Sheldrick, G. M., Siemens XRD, Madison, WI.

(124) Wam, V. W.-W.; Choi, S. W.-K.; Chan, C.-L.; Cheung, K.-K. *J. Chem. Soc., Chem. Commun.* **1996**, 2067-2068.

(125) Yamazaki, S.; Deeming, A. J. *J. Chem. Soc., Dalton Trans.* **1993**, 3051-3057.

(126) Abu Salah, O. M.; Bruce, M. I.; Churchill, M. R.; Bezman, S. A. *J. Chem. Soc., Chem. Commun.* **1972**, 858-859.

(127) Abu Salah, O. M.; Bruce, M. I.; Redhouse, A. D. *J. Chem. Soc., Chem. Commun.* **1974**, 855-856.

(128) Churchill, M. R.; Bezman, S. A. *Inorg. Chem.* **1974**, *13*, 1418-1426.

(129) Janssen, M. D.; Herres, M.; Zsolnai, L.; Grove, D. M.; Spek, A. L.; Lang, H.; van Koten, G. *Organometallics* **1995**, *14*, 1098-1100.

(130) Janssen, M. D.; Herres, M.; Zsolnai, L.; Spek, A. L.; Grove, D. M.; Lang, H.; van Koten, G. *Inorg. Chem.* **1996**, *35*, 2476-2483.

(131) Janssen, M. D.; Herres, M.; Spek, A. L.; Grove, D. M.; Lang, H.; van Koten, G. *J. Chem. Soc., Chem. Commun.* **1995**, 925-926.

(132) Janssen, M. D.; Kohler, K.; Herres, M.; Dedieu, A.; Smeets, W. J. J.; Spek, A. L.; Grove, D. M.; Lang, H.; van Koten, G. *J. Am. Chem. Soc.* **1996**, *118*, 4817-4829.

(133) Colbert, M. C. B.; Ingham, S. L.; Lewis, J.; Long, N. J.; Raithby, P. R. *J. Chem. Soc., Dalton Trans.* **1994**, 2215-2216.

(134) Evans, D. F. *J. Chem. Soc.* **1959**, 2003-2005.

(135) Geoffroy, G. L.; Wrighton, M. S. *Organometllic Photochemistry*; Academic Press: New York, 1979.

(136) Sato, M.; Shintate, H.; Kawata, Y.; Sekino, M.; Katada, M.; Kawata, S. *Organometallics* **1994**, *13*, 1956-1962.

(137) Lever, A. B. P. *Inorganic Electronic Spectroscopy*; 2nd ed.; Elsevier: New York, 1984.

(138) Creutz, C. *Inorg. Chem.* **1978**, *17*, 3723-3725.

(139) Kober, E. M.; Goldsby, K. A.; Narayana, D. N. S.; Meyer, T. J. *J. Am. Chem. Soc.* **1983**, *105*, 4303-4309.

(140) Dowling, N.; Henry, P. M.; Lewis, N. A.; Taube, H. *Inorg. Chem.* **1981**, *20*, 2345-2348.

(141) Hong, Y.; Miller, L. L. *Chem. Mater.* **1995**, *7*, 1999-2000.

(142) Itatani, H.; Bailar, J. C. J. *J. Am. Oil Chem. Soc.* **1967**, *44*, 147-151.

(143) Van Hecke, G. R.; Horrocks, W. D. J. *Inorg. Chem.* **1966**, *5*, 1968-1974.

(144) Wu, R.; Schumm, J. B.; Pearson, D. L.; Tour, J. M. *J. Org. Chem.* **1996**, *61*, 6906-6921.

(145) Bäuerle, P.; Wurthner, F.; Gotz, G.; Effenberger, F. *Synthesis* **1993**, 1099-1103.

(146) MacEachern, A.; Soucy, C.; Leitch, L.; Arnason, J. T.; Morand, P. *Tetrahedron* **1988**, *44*, 2403-2412.

(147) Jones, K.; Lappert, M. F. *J. Chem. Soc.* **1965**, 1944-1951.

(148) Viola, E.; Sterzo, C. L.; Crescenzi, R.; Frachey, G. *J. Organomet. Chem.* **1995**, *493*, C9-C13.

(149) These complexes were prepared previously but were not characterized by CV. see: Hodge, A. J.; Ingham, S. L.; Kakkar, A. K.; Klan, M. D.; Lewis, J.; Long, N. J.; Parker, D. G.; Raithby, P. R. *J. Organomet. Chem.* **1995**, *488*, 205-210.

(150) Rossiter, B. W.; Hamilton, J. F. *Physical Methods of Chemistry*; Wiley: New York, 1986; Vol. 2.

(151) This complex was prepared previously but was not characterized by CV and UV–vis spectroscopy. see: Touchard, D.; Haquette, P.; Pirio, N.; Toupet, L.; Dixneuf, P. H. *Organometallics* **1993**, *12*, 3132-3139.

(152) Miller, L. L.; Yu, Y. *J. Org. Chem.* **1995**, *60*, 6813-6819.

(153) Sohn, Y. S.; Hendrickson, D. N.; Gray, H. B. *J. Am. Chem. Soc.* **1971**, *93*, 3603-3612.

(154) Sotzing, G. A.; Reynolds, J. R.; Steel, P. J. *Chem. Mater.* **1996**, *8*, 882-889.

(155) Curtis, J. C.; Sullivan, B. P.; Meyer, T. J. *Inorg. Chem.* **1983**, *22*, 224-236.

(156) Sato, M.; Shiraogawa, M. *CACS Forum (Japanese)* **1993**, *13*, 30-32.

(157) Wolfgang, H.; Andrejewski, D., German Patent DE3703771, 1988.

(158) Graf, D. D.; Mann, K. R. *Inorg. Chem.* **1997**, *36*, 150-157.

(159) Hotta, S.; Hosaka, T.; Shimotsuma, W. *Synth. Met.* **1983**, *6*, 69-71.

(160) Patil, A. O.; Heeger, A. J.; Wudl, F. *Chem. Rev.* **1988**, *88*, 183-200.

(161) Liebeskind, L. S.; Fengl, R. W. *J. Org. Chem.* **1990**, *55*, 6359-5364.

(162) Stille, J. K. *Angew. Chem. Int. Ed. Engl.* **1986**, *25*, 508-524.

(163) Baker, R. W.; Braithwaite, M. J.; Nyholm, R. S. *J. Chem. Soc., Dalton Trans.* **1972**, 1924-1928.

(164) Briant, C. E.; Rowland, K. A.; Webber, C. T.; Mingos, D. M. P. *J. Chem. Soc., Dalton Trans.* **1981**, 1515-1519.

(165) Severin, K.; Polborn, K.; Beck, W. *Inorg. Chim. Acta* **1995**, *240*, 339-346.

(166) Sekutowski, D.; Jungst, R.; Stucky, G. D. *Inorg. Chem.* **1978**, *17*, 1848-1855.

(167) Bristow, S.; Garner, C. D.; Clegg, W. *Inorg. Chim. Acta* **1983**, *76*, L261-L262.

(168) Chakravarty, A. R.; Cotton, F. A.; Schwotzer, W. *Inorg. Chim. Acta* **1984**, *84*, 179-185.

(169) Asplund, M.; Jagner, S.; Nilsson, M. *Acta Chem. Scand. (A)* **1983**, *37*, 57-62.

(170) Grocott, S. C.; Wild, S. B. *Inorg. Chem.* **1982**, *21*, 3526-3534.

(171) Kittlesen, G. P.; White, H. S.; Wrighton, M. S. *J. Am. Chem. Soc.* **1984**, *106*, 7389-7396.

(172) Paul, E. W.; Ricco, A. J.; Wrighton, M. S. *J. Phys. Chem.* **1985**, *89*, 1441-1447.

(173) Thackeray, J. W.; White, H. S.; Wrighton, M. S. *J. Phys. Chem.* **1985**, *89*, 5133-5140.

(174) Pickup, P. G.; Kutner, W.; Leidner, C. R.; Murray, R. W. *J. Am. Chem. Soc.* **1984**, *106*, 1991-1998.